ISSN 1811-1165 (Print)
ISSN 2413-2179 (Online)

EURASIAN PHYSICAL TECHNICAL JOURNAL

VOLUME 19, NO. 4(42), 2022

phtj.buketov.edu.kz

EURASIAN PHYSICAL TECHNICAL JOURNAL

p - ISSN 1811-1165
e - ISSN 2413-2179

Volume 19, No. 4(42), 2022

1st issue – March, 2004

Journal Founder:

E.A. BUKETOV KARAGANDA UNIVERSITY

Е.А.БӨКЕТОВ АТЫНДАҒЫ ҚАРАҒАНДЫ УНИВЕРСИТЕТІ

КАРАГАНДИНСКИЙ УНИВЕРСИТЕТ имени Е.А.БУКЕТОВА

Contact information:
Editorial board of EAPhTJ (Build. 2, room 216)
E.A. Buketov Karaganda University
Universitetskaya Str. 28, Karaganda,
Kazakhstan, 100028
Subscription index: 75240

Tel: +7(7212) 77-04-03
Fax: +7(7212) 35-63-98
E-mail: ephtj@mail.ru

Signed to print on 20.12.2022
Format 60x84 1/8. Offset paper.
Volume 12.38 p.sh. Circulation 300 copies.
Agreed price. Order No. 1.

Басуға 20.12.2022 ж. қол қойылды.
Пішімі 60×84 1/8. Офсеттік қағазы.
Көлемі 12,38 ес.-б.т. Таралымы 300 дана.
Бағасы келісім бойынша. Тапсырыс № 1.

Подписано к печати 20.12.2022 г.
Формат 60 × 84 1/8. Офсетная бумага.
Объем 12,38 печ.л. Тираж 300 экз.
Цена договорная. Заказ № 1.

Printed in the Publishing House
of the E.A.Buketov Karaganda University

Е.А. Бөкетов атындағы Қарағанды университеті баспасының баспаханасында басылып шықты

Отпечатано в Издательстве Карагандинского университета им. академика Е.А.Букетова

Registration Certificate No.4382-Zh, November 7, 2003.
Re-registration Certificate No.KZ50VPY00027647, October 6, 2020 issued by Information Committee of the Ministry of Information and Public Development of the Republic of Kazakhstan

Eurasian Physical Technical Journal, 2022, Vol. 19, No. 4(42)

CONTENTS

Dear authors and readers!
Dear Colleagues!

Traditionally, we inform you about the scientometric indicators of the Eurasian Physical Technical Journal as a peer-reviewed scientific journal, indexed in the Scopus database. As of December 6, 2022, the Cite Score Tracker is 1.0. This indicator dynamics is determined directly by the number of citations in other editions of articles, that published in the Eurasian Physical Technical Journal. On site you can see the monthly update of this indicator - https://phtj.buketov.edu.kz/index.php/EPTJ/index.

At the end of the year the results are usually summed up. In last year, a lot of work was done to process and enter information into the database of our Journal's website. According to statistics for 2022, 186 materials were accepted to the site. And 56 articles were prepared and published in 4 issues (the share of rejected articles was 18%). The rest of the material has been processed and entered into the Archive to provide a search option.

In 2022, the geography of authors expanded: in addition to authors from scientific centers of Kazakhstan and Russia, articles for publication were sent by scientists from Belarus, Germany, India, Iraq, Latvia, Nigeria, Poland, Ukraine, Uzbekistan, etc. The composition of the editorial board was partially updated, the database is constantly updated reviewers.

Practice shows that "the competitiveness of scientific potential is one of the main priorities of the many developed countries state policy". On a global scale, 2022 in science has definitely become the year of the cosmos, since most of the bright discoveries are related precisely to what is happening outside our planet. There are five most important and significant discoveries made in the past year.

It has been established that black holes play an important role in the evolution of galaxies and stimulate the emergence of life. In January 2022, the Hubble telescope discovered a black hole in the center of the dwarf galaxy Henize 2-10, which did not absorb, but created new stars. German astrophysicist Rob Farmer (Max Planck Institute) found that a large star paired with a black hole emits almost six times more carbon into space than a similar lone star should. The gas flowing from the black hole leads to the birth of a new star.

On January 11, 2022, China's Chang'e-5 probe discovered water on the moon. Before that, in samples of lunar soil delivered to Earth, scientists found signs of water. But in samples of light bubble rock, it turned out to be 1.5 times more water, which is stored under a layer of soil in the form of ice.

In February 2022, engineers at the Massachusetts Institute of Technology created a unique polymer material 2DPA-1, which is lighter than plastic and stronger than steel. The material is impervious to gases and liquids, it can be used to make cars and even build houses.

In July 2022, the James Webb Space Telescope obtained the first high-resolution image of distant galaxies, confirming the effect of gravitational lensing. It is proved that the trajectory of light from distant objects, when passing inside massive accumulations of matter, is curved.

Until 2022, the part of DNA that does not code for protein, but is responsible for various aspects of cell functioning, remained unsolved. A team of scientists from 54 institutes from different countries - T2T-Consortium deciphered the remaining 8% and received a complete genome, which, as a new standard in genetics, will allow more accurate identification of individual genetic characteristics.

In this issue readers are offered articles based on the results of research on topical problems of physics and technology. These scientific researches were also highlighted in the Concept for the Development of Science of the Republic of Kazakhstan for 2022-2026 as “priority areas of science”.

In the Materials Science section of an article by scientists from Orenburg, the results of studying the effect of a magnetic field generated by a ferromagnetic nanoparticle on the annihilation of triplet-excited organic molecules or triplet excitons in the surface layer of particles are presented. It was found that "the influence of the magnetic field gradient on the reaction yield dominates over other known mechanisms of spin dynamics in triplet-triplet pairs." Important practical results were obtained by domestic scientists, who proved the fundamental possibility and effectiveness of processing by "high-pressure torsion to form an ultra-fine-grained structure and increase the strength properties of steel rings." In the article by authors from Tashkent, “radiation defects in steatite ceramics were studied by the method of diffuse reflection”, when irradiated with high doses of gamma radiation from a source and mixed reactor no-gamma irradiation. "The formation of structural defects under gamma irradiation in the form of oxygen vacancies in the ultraviolet region of the spectrum" and the appearance of various hole centers were found. In the article by the authors of our university, the influence of the anodizing voltage during synthesis on the specific surface area and on the photocatalytic activity of titanium dioxide nanotubes was studied. “The specific surface area of titanium dioxide nanotube films was

determined by the method of low-temperature nitrogen adsorption, the value of which decreases with increasing voltage."

Articles in the Energy section are devoted to solving the environmental problems of traditional energy and the use of alternative energy sources. In the work of Moscow authors, an assessment was made of the "carbon footprint for combined-cycle and oxygen-fuel plants operating for 20 years both on natural gas and on coal with intracycle gasification." It is shown that "the transition to oxygen-fuel power plants can reduce the carbon footprint by about 90% in the case of natural gas and about 75% for coal fuel." To further reduce the carbon footprint, it is proposed to introduce carbon dioxide capture and storage systems. In the work of the authors from Uzbekistan, the results of a comparison of the electrical parameters of solar batteries used in natural conditions of a hot climate are presented. It has been experimentally shown that single-crystal photovoltaic and photothermal batteries are the most efficient.

Interesting technical and innovative developments are offered in the Engineering section. The work of Ryazan scientists presents a measuring and analytical complex for automated study of low-frequency noise spectra in electronic elements, components and semiconductor materials and structures. The complex is adapted with an atomic force microscope for local measurements of the noise characteristics of electronic materials and structures. The results of checking the operation of the measuring complex are presented on the example of the study of the Schottky diode structure. The article by Kazakh scientists presents the development of the architecture of the onboard nanosatellite control complex with hardware and circuitry solutions. The main functions of the onboard software necessary for the design and development of ultra-small artificial satellites are described. In the next article, on the basis of modern methods of mechanics of a deformable solid body, the reliability of the technological scheme of a coal mine is assessed, taking into account the stress state of mine workings, depending on the combination of mining, geological and technological factors.

The section Physics and Astronomy presents the results of studies of "fine" phenomena of absorption of nanoparticles and defects on the mass spectra of mesons. The scientists of the Molecular Nano-photonics Institute have studied the transient absorption of gold nanoparticles of a certain diameter upon photoexcitation by nanosecond laser pulses. It has been experimentally shown that the "stationary absorption maximum is represented by a wide structureless band, which has a fine structure with a certain periodicity of maxima and does not depend on the size of nanoparticles. The nanosecond duration of the transient absorption of gold nanoparticles is the result of a protracted relaxation process as a manifestation of hindered heat exchange with the environment". In an article by authors from research centers in Nigeria, the influence of a topological defect on the mass spectra of heavy and heavy-light mesons was studied. Approximate solutions of the Schrödinger equation for the energy spectrum and the non-normalized wave function were obtained by the Nikiforov-Uvarov method. It is shown that as "the topological defect increases, the mass spectra shift".

We hope that the presented research results will be of interest to scientists, teachers, researchers, doctoral students and undergraduates.

I would especially like to express deep gratitude to our reviewers for an objective and qualified examination of the materials, which helps to ensure the articles quality.

We will be glad to see you among our readers and authors of the next issues, in which it is planned to publish custom-made review articles by leading scientists on the most relevant and priority areas of modern physics and technology.

Best wishes,
Editor-in-chief, professor Sakipova S.E.
September, 2022

DOI 10.31489/2022No4/5-16

UDC 537.636; 538.971; 539.22; 53.098

SPIN-SELECTIVE INTERACTION OF TRIPLET-EXCITED MOLECULES ON THE SURFACE OF A FERROMAGNETIC NANOPARTICLE

Kucherenko M.G., Neyasov P.P.*

Orenburg State University, Center for Laser and Information Biophysics, Orenburg, Russia, nejapetr@yandex.ru

Influence of a magnetic field generated by a ferromagnetic nanoparticle on the annihilation of triplet-excited organic molecules or triplet excitons in a near-surface particle layer is studied. A detailed mathematical model is presented that accounts for electron excitation diffusive mobility and geometry of the system. The kinetic operator is given in the complete 9x9 basis of triplet- triplet pair spin states. Time dependencies of the singlet spin state population of the triplet-triplet pair and the dependence of the triplet-triplet annihilation magnetic response profile (magnetic reaction effect) from the magnetic field induction are obtained. It is found that the influence of a magnetic field gradient on the reaction yield dominates over the other known mechanisms of spin-dynamics in triplet- triplet pairs.

Keywords: triplet-triplet annihilation, ferromagnetic nanoparticle, inhomogeneous magnetic field, magnetic effect.

Introduction

Contemporary studies of magnetically controlled processes in polymeric media, in particular, polymer light emitting diodes (PLEDs), present a special interest. For instance, paper [1] is devoted to the influence of an external magnetic field on the triplet-triplet annihilation (TTA) on the magnetically dependent electric conductivity (MEC) and on the magnetically dependent electroluminescence (MEL) of SY-PPV polymer (poly (para-phenylenevinylene)). In the present paper it is shown that in weak magnetic fields (<200 Oe) the positive magnetic effect occurs both for MEC and MEL. In magnetic fields H>200 Oe the decrease of MEL was explicitly observed; it is due to the increase of the triplet excitons lifetime and TTA suppression.

In paper [2] the influence of ferromagnetic $Co_{53}Pt_{47}$ nanowires induced in MEHPPV polymer (poly [2-methoxy,5-(2-ethylhexyloxy)-1,4-phenylenevinylene]) on electroluminescence was studied alongside the influence on phosphorescence of the iridium complex $Ir(ppy)_3$ (three-(2-phenylpyridinate) iridium (III)). Study performed in this paper shows that a doping with dispersed $Co_{53}Pt_{47}$ nanowires increases the probability of singlet-triplet exciton transitions in semiconductor MEHPPV films which are induced by the strong nanowires magnetic field. The influence of strong magnetic fields (B~9 T) on the magnetic fluorescence effect and phosphorescence in OLEDs was studied in [3].

Study of TTA involving electronically excited I_2-Bodipy molecules in various media was conducted in [4]. The influence of various solvent types on the quantum yield, delayed fluorescence frequency shift, and triplet states lifetime was studied. In paper [5] kinematics of the triplet excitation annihilation and the delayed fluorescence damping of an isolated 1,12-benzperylene pairs in n-hexane were studied; it was shown that their triplet excitation annihilation rate, decrease of the number of triplet-excited pairs, and damping of the annihilation delayed fluorescence are subjected to an exponential law provided the statistical spread of molecules by the rate constants vanishes. Exchange-resonance processes of homo- and heterogeneous annihilation of erythrosine and anthracene molecules placed on the surface of anodized aluminum were studied in a wide temperature interval [6]. The results show that the exchange photo-processes involving dye molecules adsorbed on the surface of anodized aluminum can be described within a fractal model. The direct influence of local magnetic fields of superparamagnetic Fe_2O_3 nanoparticles on the kinematics of the delayed fluorescence alongside 6G rhodamine and acriflavine fluorescence in the polyvinyl alcohol polymer matrix was empirically studied in [7].

Currently certain attempts to unite the descriptions of two physical processes, namely, plasmon resonance and TTA are conducted. In paper [8] an opportunity was studied to create a composite system for a photocatalytic destruction of an air pollutant, namely, acetaldehyde, based on the triplet-triplet annihilation which total photocatalytic efficiency is enhanced with plasmonic AgNP-SiO_2 nanoparticles. Plasmonic enhancement of the triplet-triplet annihilation within thin films of polymethylmethacrylate containing

.

palladium (II) octaethylporphyrin and 9,10-diphenylanthracene doped with silver nanoplates was found in [9]. The plasmon resonance allows one to detect fluorescence even if its intensity is extremely low. This fact was studied in details in paper [10]. Fluorescence of thin copper phthalocyanine on a golden platform was studied. The authors argued that the plasmon amplification of the triplet-triplet annihilation was also detected in the research.

Further studies of ferromagnetic particles influence on TTA in nanostructured media requires development of synthesis methods for such systems, for instance, nano-dispersed inclusions in the matrix can be polymer spheres [11-12]. These papers present a detailed discussion of ferromagnetic nanoparticles synthesis based on $FeCl_2$ and $FeCl_3$ electroless code position and their stabilization alongside the discussion of polymer spheres synthesis base on SAW (sodium dodecyl sulfate) and styrene. Nanoreactors are often synthesized on mesoporous silica base [13] and can also be based on ordered mesoporous carbon [14].

Paper [15] is devoted to a study of the pair spin states dynamics of two triplet (T) molecules which are partners in the spin-selective reaction and that were placed in a reaction cell with a ferromagnetic nanoparticle. It was taken into account that such a particle has residual magnetization, or acquires it in an external magnetic field. A theoretical model describing the T-T electronic perturbations annihilation in a nanoreactor containing a globular magnetic nanoparticle serving as the catalytic element was proposed and it is based on the so-called «Δg-mechanism» (which is due to the difference in molecules g-factors) which is due to a split of the cell volume in three areas divided by potential barriers. Within a strong field and hop reagent migration approximations it was evaluated how the magnetic annihilation effect value depends on the magnetic field induction generated by the catalytic nanoparticle in each of the spatially-separated areas.

Thus, despite the expressed interest in the problem of magnetically controlled annihilation of triplet electronic excitations near ferromagnetic nanoparticles, the analysis of the results obtained based on an adequate theoretical model of spin-selective reactions, which takes into account the inhomogeneous nature of the magnetic field in the vicinity of ferromagnetic nanoparticles, has not yet been carried out, due to the lack of such a model.

In this paper, a corresponding model is proposed and, on its basis, the spin dynamics of molecular T–T pairs in the magnetic field of a globular ferromagnetic nanoparticle is studied, taking into account the gradient effects of the field. In a typical variant of the migration of a spin-carrying molecule, i.e., its free diffusion in a circular or spherical region with a nanoparticle located in the center of the region and reflection at its boundary, the TTA magnetic effect was calculated from the modulation of the spin-selective reaction rate by the field. Moreover, in contrast to [15], the spin dynamics was analyzed in the general case, i.e., outside the framework of the strong magnetic field approximation. For this purpose, the 9x9 force matrix describing interactions between T-molecules is constructed (Table 1).

Giant palladium clusters have an icosahedral core with N=561 atoms (five-layer cluster). In a large number of works devoted to magnetic nanoclusters, clusters of spherical and spheroidal shapes are considered. Experimental observations of the shell structure of metal clusters show that clusters with a magic number of atoms have a spherical shape (N=13; 55; 147) [16]. Analysis of the rearrangement of the magnetization of Fe clusters at R>Rc was carried out for spherical clusters [17, 18].

1. Mathematical model

Magnetized ferromagnetic nanoparticle in a nanocavity creates a magnetic field that affects nearby spin-selective reactions involving paramagnetic molecules or triplet excitons. Be-cause of this it is important to search for a detailed description of the reaction kinematics in such nanoreactor systems with a magnetized core [15]. In this paper, we consider layered (shell) magnetic particles of a cylindrical or spherical shape, on the surface of which particles of two types (molecules or quasiparticles-excitons), with different diffusion coefficients D_1 and D_2, can freely move, annihilating at a distance is especially effective when they approach the interaction radius. Magnetic particles are placed inside nanoreactors.

The magnetic field arising in the shell does not significantly affect the nature of particle motion in the layer between the ferromagnetic particle and the inner surface of the nanoreactor. At the same time, the spin dynamics of molecules with a nonzero electronic or nuclear magnetic moment depends on the magnitude of the induction B of the magnetic field **B**.

In certain cases, spatial and spin dynamics can be studied independently. Nonetheless, the spin-selective annihilation yield is to be defined both by spatial and spin properties. In the case to be discussed further the

reaction rate depends on positions $\mathbf{r}_1$ and $\mathbf{r}_2$ of the reagents placed within the layer at a given time *t* which are "marked" with magnetic field induction vectors $\mathbf{B}(\mathbf{r}_1)$ and $\mathbf{B}(\mathbf{r}_2)$. We define the coordinate-spin density operator $\hat{\rho}(\mathbf{r}_1,\mathbf{r}_2,t\,|\,\mathbf{r}_1',\mathbf{r}_2',\mathbf{B}(\mathbf{r}_1),\mathbf{B}(\mathbf{r}_2))$ which defines the population growth rate of the state $|JM\rangle$ optimal for the reaction (here *J*, *M* are the total spin moment and its z-projection correspondingly). For the rate constant $K(\mathbf{r}_1',\mathbf{r}_2')$ of the spin-selective triplet (T) states annihilation the following holds

$$K(\mathbf{r}_1',\mathbf{r}_2')=\int_0^\infty dt\iint_{\Delta V_R} U(|\,\mathbf{r}_1-\mathbf{r}_2\,|)\frac{1}{2}\mathrm{Tr}\left\{\hat{P}_S,\hat{\rho}(\mathbf{r}_1,\mathbf{r}_2,t\,|\,\mathbf{r}_1',\mathbf{r}_2',\mathbf{B}(\mathbf{r}_1),\mathbf{B}(\mathbf{r}_2))\right\}_+ d^3r_1d^3r_2\,, \tag{1}$$

where $\mathrm{Tr}\left\{\hat{P}_S,\hat{\rho}\right\}_+=\sum_{J,M}\langle JM\left|\left(\hat{P}_S\hat{\rho}+\hat{\rho}\hat{P}_S\right)\right|JM\rangle=\langle 00|\hat{\rho}|00\rangle$, because $\hat{P}_S=|00\rangle\langle 00|$ is the operator performing a projection of the T-T pair singlet state; $\mathbf{r}_1',\mathbf{r}_2'$ are the initial positions of the mobile particles. ΔV_R - integration volume (volume of the layer between the ferromagnetic particle and the inner surface of the nanoreactor), $U(r)$ is the distance-dependent rate of an annihilation act. The spin-Hamiltonian of a T-T pair $\hat{H}(\mathbf{r}_1,\mathbf{r}_2)$ is given by the following

$$H=g_1\mu_B B(\mathbf{r}_1)S_{1Z}+g_2\mu_B B(\mathbf{r}_2)S_{2Z}-2J_{exc}(r_{12})\mathbf{S}_1\mathbf{S}_2-\mathbf{S}_1\mathbf{D}(\Omega_1)\mathbf{S}_1-\mathbf{S}_2\mathbf{D}(\Omega_2)\mathbf{S}_2\quad. \tag{2}$$

Description of the kinetic of the spin-selective triplet electronic excitations annihilation within a potential field $V(\mathbf{r}_1,\mathbf{r}_2)$ can be based on the density operator $\hat{\rho}(\mathbf{r}_1,\mathbf{r}_2,t)$ (we do not highlight here the explicit dependence on the magnetic field induction **B**, parameters $\mathbf{r}_1',\mathbf{r}_2'$ omitted) satisfying the following equation with the spin-Hamiltonian $\hat{H}(\mathbf{r}_1,\mathbf{r}_2)$ of the T-T pair and for the Fokker-Planck transport operator (the diffusion operators for a layer with the coefficient D_j)

$$\begin{aligned}\frac{\partial}{\partial t}\hat{\rho}(\mathbf{r}_1,\mathbf{r}_2,t)&=-\frac{i}{\hbar}\left[\hat{H}(\mathbf{r}_1,\mathbf{r}_2),\hat{\rho}(\mathbf{r}_1,\mathbf{r}_2,t)\right]-\Gamma\hat{\rho}(\mathbf{r}_1,\mathbf{r}_2,t)+\\&+\sum_{j=1}^{2}D_j\,\mathrm{div}\left(\nabla_j+\frac{1}{k_BT}\nabla_j V\right)\hat{\rho}(\mathbf{r}_1,\mathbf{r}_2,t)-\frac{1}{2}U(|\,\mathbf{r}_1-\mathbf{r}_2\,|)\left\{\hat{\rho}(\mathbf{r}_1,\mathbf{r}_2,t)\hat{P}_S+\hat{P}_S\hat{\rho}(\mathbf{r}_1,\mathbf{r}_2,t)\right\}.\end{aligned} \tag{3}$$

The first two terms define Zeeman interaction of single triplets (with different g-factors g_1 and g_2) of a T-T-pair with the local magnetic field induction $B(\mathbf{r}_j)$ generated by the ferromagnetic nanoparticle at the points of placement of molecules 1 and 2; the third term describes the intermolecular exchange interaction with the exchange $J_{exc}(r_{12})$ depending on the distance between triplet pairs r_{12}; the last two terms describe the inter-triplet spin-spin interaction. Operators S_1, S_2 are vector operators of molecules (1) and (2) electronic spins; $\mathbf{D}(\Omega_{1(2)})$ is the tensor of the magnetic dipole-dipole interaction; $\Omega_{1(2)}$ are the angular parameters; μ_B is the Bohr magneton. Hamiltonian of the spin-spin interaction $H_{SS}=-S_1D_1S_1-S_2D_2S_2$ accounts only for the magnetic dipole intermolecular interaction, while the inter-triplet spin-spin interaction is assumed to be negligibly small due to the relatively large radius of the molecular pair. The exchange interaction operator is diagonal in the pair basis $|JM\rangle$ of the total electronic spin of the T-T pair $S = S_1 + S_2$. The value of the exchange integral fall with the intermolecular distance *r* and tends to zero in the following conditions $R_0 << r < R:\ J_{exc}(r)\to 0$.

In the case when the diffusion fluxes are determined by the density gradients of the initial distribution, and not by the gradients formed by distance annihilation, it can be assumed - at a sufficiently low annihilation rate - that diffusion occurs almost independently of the reaction. In that case the density operator $\hat{\rho}(\mathbf{r}_1,\mathbf{r}_2,t)$ can be factorized $\hat{\rho}(\mathbf{r}_1,\mathbf{r}_2,t)=\hat{\rho}_S(\mathbf{r}_1,\mathbf{r}_2,t)G_2(\mathbf{r}_1,\mathbf{r}_2,t)$, where $G_2(\mathbf{r}_1,\mathbf{r}_2,t)$ is the two-particle Fokker-Planck equation Green function for massless particles that do not interact with each other. Such a split of spatial and spin variables is justified be the following reasoning. The operator

.

$\hat{\rho}(\mathbf{r}_1,\mathbf{r}_2,t)=\hat{\rho}_S(\mathbf{r}_1,\mathbf{r}_2,t)G_2(\mathbf{r}_1,\mathbf{r}_2,t)$ can be placed into equation (2) and we are to assume that the following approximation holds

$$\sum_{j=1}^{2} D_j \nabla_j^2 \hat{\rho}_S(\mathbf{r}_1,\mathbf{r}_2,t)G_2(\mathbf{r}_1,\mathbf{r}_2,t) \approx \hat{\rho}_S(\mathbf{r}_1,\mathbf{r}_2,t)\sum_{j=1}^{2} D_j \nabla_j^2 G_2(\mathbf{r}_1,\mathbf{r}_2,t) \tag{4}$$

which is due to the small values of gradients $\nabla_j \hat{\rho}_S(\mathbf{r}_1,\mathbf{r}_2,t)$; therefore, the following inequalities hold

$$\sum_{j=1}^{2} D_j \nabla_j \hat{\rho}_S(\mathbf{r}_1,\mathbf{r}_2,t)\nabla_j G_2(\mathbf{r}_1,\mathbf{r}_2,t) << \hat{\rho}_S(\mathbf{r}_1,\mathbf{r}_2,t)\sum_{j=1}^{2} D_j \nabla_j^2 G_2(\mathbf{r}_1,\mathbf{r}_2,t)$$

and

$$G_2(\mathbf{r}_1,\mathbf{r}_2,t)\sum_{j=1}^{2} D_j \nabla_j^2 \hat{\rho}_S(\mathbf{r}_1,\mathbf{r}_2,t) << \hat{\rho}_S(\mathbf{r}_1,\mathbf{r}_2,t)\sum_{j=1}^{2} D_j \nabla_j^2 G_2(\mathbf{r}_1,\mathbf{r}_2,t).$$

In that case equation (2) allows one to obtain the following equation for the spin-density operator $\hat{\rho}_S(\mathbf{r}_1,\mathbf{r}_2,t)$ which is free from the Laplacian and any other spatial derivatives

$$\begin{aligned}\frac{\partial}{\partial t}\hat{\rho}_S(\mathbf{r}_1,\mathbf{r}_2,t) &= -\frac{i}{\hbar}\left[\hat{H}(\mathbf{r}_1,\mathbf{r}_2),\hat{\rho}_S(\mathbf{r}_1,\mathbf{r}_2,t)\right] - \Gamma\hat{\rho}_S(\mathbf{r}_1,\mathbf{r}_2,t) - \\ &-\frac{1}{2}U(|\mathbf{r}_1-\mathbf{r}_2|)\left\{\hat{\rho}_S(\mathbf{r}_1,\mathbf{r}_2,t)\hat{P}_S + \hat{P}_S\hat{\rho}_S(\mathbf{r}_1,\mathbf{r}_2,t)\right\}.\end{aligned} \tag{5}$$

In such a way the spatial variables $\mathbf{r}_1,\mathbf{r}_2$ in operator $\hat{\rho}_S(\mathbf{r}_1,\mathbf{r}_2,t)$ serve as parameters. Namely, in case of the triplet (T) excitations annihilation via the single channel the following holds

$$\hat{\rho}_S(\mathbf{r}_1,\mathbf{r}_2,t)=\exp[-\Gamma t]\exp(\hat{K}t)\hat{\rho}_S(\mathbf{r}_1',\mathbf{r}_2',0)\exp(\hat{K}^* t) \tag{6}$$

where are non-Hermitian evolution operators

$$\begin{aligned}\hat{K}(\mathbf{B}(\mathbf{r}_1),\mathbf{B}(\mathbf{r}_2)) &= -\frac{i}{\hbar}\left(\hat{H}(\mathbf{B}(\mathbf{r}_1),\mathbf{B}(\mathbf{r}_2)) - i\frac{\hbar}{2}\hat{\Lambda}(r_{12})\right), \\ \hat{K}^*(\mathbf{B}(\mathbf{r}_1),\mathbf{B}(\mathbf{r}_2)) &= \frac{i}{\hbar}\left(\hat{H}(\mathbf{B}(\mathbf{r}_1),\mathbf{B}(\mathbf{r}_2)) + i\frac{\hbar}{2}\hat{\Lambda}(r_{12})\right).\end{aligned} \tag{7}$$

And the annihilation influence on the T-T pair spin-dynamics is explicitly accounted by the following operator

$$\hat{\Lambda}(r_{12}) = U(|\mathbf{r}_1-\mathbf{r}_2|)\hat{P}_S.$$

The matrix $\langle JM|K|J'M'\rangle$ of the kinetic operator (7) is given by the following Table 1. In the table 1: $H_Z^{\pm}=\mu_B\frac{i}{\hbar}(g_1B_1 \pm g_2B_2)$ are Zeeman interaction matrix elements; $H_{exc}=2\frac{i}{\hbar}J_{exc}$ is the exchange interaction matrix element; $H_E^{\pm}=\frac{i}{\hbar}(E_1 \pm E_2)$, $H_D^{\pm}=\frac{i}{\hbar}(D_1 \pm D_2)$ are matrix elements of the spin-spin interaction.

We introduce the following notations $g_1=g$, $g_2=g+\Delta g$, $B_1=B$, $B_2=B+\Delta B$. In these notations the Hamiltonian (3) reads

$$\hat{H}=g\mu_B B\left(\hat{S}_{1Z}+\hat{S}_{2Z}\right)+\left[g\Delta B+\Delta g(B+\Delta B)\right]\mu_B\hat{S}_{2Z}-J_{exc}(r)\left(\hat{\mathbf{S}}^2-4\right)+\hat{V}_{SS}, \tag{3'}$$

or

$$\hat{H}=\hat{H}_0+V_{SS},\ \hat{H}_0=\hat{H}_0^{(1)}+\hat{H}_0^{(2)},\ \hat{H}_0^{(1)}=g\mu_B B\hat{S}_Z-J_{exc}(\hat{\mathbf{S}}^2-4),\ \hat{H}_0^{(2)}=[g\Delta B+\Delta g(B+\Delta B)]\mu_B\hat{S}_{2Z}.$$

Terms of Hamiltonian (3') should be grouped up as follows: $\hat{H} = \hat{H}_0^{(1)} + [\hat{H}_0^{(2)} + \hat{V}_{SS}] = \hat{H}_0^{(1)} + \hat{V}$. The pair basis sates $|JM\rangle$ are eigenstates for $\hat{H}_0^{(1)}$, but not for $\hat{H}_0^{(2)}$. Consequently,

$$\hat{H}_0^{(1)}|JM\rangle = \left[g\mu_B BM - J_{exc}\left(J(J+1)-4\right)\right]|JM\rangle,\ M = m_1 + m_2,$$

while operators $\hat{H}_0^{(2)}, \hat{V}_{SS}$ induce transitions between states of the pair basis $|JM\rangle$.

Table 1. The kinetic operator matrix $\langle JM|K|J'M'\rangle$

J \ J'		**0**	**1**			**2**				
	M \ M'	**0**	**-1**	**0**	**1**	**-2**	**-1**	**0**	**1**	**2**
0	**0**	$2H_{exc} - K_S$	0	$-\frac{2}{\sqrt{6}}H_Z^{\pm}$	0	$-\frac{1}{\sqrt{3}}H_E^{\pm}$	0	$-\frac{\sqrt{2}}{3}H_D^{\pm}$	0	$-\frac{1}{\sqrt{3}}H_E^{\pm}$
1	**-1**	0	$\frac{1}{2}H_Z^{\pm} + H_{exc} + (1/6)H_D^{\pm}$	0	$\frac{1}{2}H_E^{\pm}$	0	$\frac{1}{2}(H_D^{\pm} - H_Z^{\pm})$	0	$\frac{1}{2}H_E^{\pm}$	0
	0	$-\frac{2}{\sqrt{6}}H_Z^{\pm}$	0	$H_{exc} - \frac{1}{3}H_D^{\pm}$	0	$-\frac{1}{\sqrt{2}}H_E^{\pm}$	0	$-\frac{2\sqrt{3}}{6}H_Z^{\pm}$	0	$\frac{1}{\sqrt{2}}H_E^{\pm}$
	1	0	$\frac{1}{2}H_E^{\pm}$	0	$H_{exc} - \frac{1}{2}H_Z^{\pm} + (1/6)H_D^{\pm}$	0	$-\frac{1}{2}H_E^{\pm}$	0	$-\frac{1}{2}(H_Z^{\pm} + H_D^{\pm})$	0
2	**-2**	$-\frac{1}{\sqrt{3}}H_E^{\pm}$	0	$-\frac{1}{\sqrt{2}}H_E^{\pm}$	0	$H_Z^{\pm} - H_{exc} - (1/3)H_D^{\pm}$	0	$-\frac{1}{\sqrt{6}}H_E^{\pm}$	0	0
	-1	0	$\frac{1}{2}(H_D^{\pm} - H_Z^{\pm})$	0	$-\frac{1}{2}H_E^{\pm}$	0	$\frac{1}{2}H_Z^{\pm} - H_{exc} + (1/6)H_D^{\pm}$	0	$-\frac{1}{2}H_E^{\pm}$	0
	0	$-\frac{\sqrt{2}}{3}H_D^{\pm}$	0	$-\frac{2\sqrt{3}}{6}H_Z^{\pm}$	0	$-\frac{1}{\sqrt{6}}H_E^{\pm}$	0	$\frac{1}{3}H_D^{\pm} - H_{exc}$	0	$-\frac{1}{\sqrt{6}}H_E^{\pm}$
	1	0	$\frac{1}{2}H_E^{\pm}$	0	$-\frac{1}{2}(H_Z^{\pm} + H_D^{\pm})$	0	$-\frac{1}{2}H_E^{\pm}$	0	$\frac{1}{6}H_D^{\pm} - \frac{1}{2}H_Z^{\pm} - H_{exc}$	0
	2	$-\frac{1}{\sqrt{3}}H_E^{\pm}$	0	$\frac{1}{\sqrt{2}}H_E^{\pm}$	0	0	0	$-\frac{1}{\sqrt{6}}H_E^{\pm}$	0	$-H_Z^{\pm} - H_{exc} - (1/3)H_D^{\pm}$

A numerical realization of the solution (6) can be expressed through the following exponential operators' matrices $\langle JM|\exp(Kt)|J'M'\rangle$

$$\langle JM|\hat{\rho}_S(t)|J'M'\rangle = \\ = \exp(-K_{-1}t) \times \sum_{J''M''}\sum_{J'''M'''} \langle JM|\exp(Kt)|J''M''\rangle\langle J''M''|\hat{\rho}_S(0)|J'''M'''\rangle\langle J'''M'''|\exp(K^*t)|J'M'\rangle \cdot \quad (8)$$

.

For 9×9 basis $|JM\rangle$ the representation $\langle JM|\exp(Kt)|J'M'\rangle$ obtained via the Sylvester theorem can be constructed numerically when the matrix $\langle JM|K|J'M'\rangle$ eigenvalues are found.

Solution of the diffusive part of the problem is obtained via the kinetic equation for the time-dependent two-particle Green function $G_2(\mathbf{r}_1,\mathbf{r}_2,t)$ for the within layer free diffusion equation

$$\frac{\partial}{\partial t}G_2(\mathbf{r}_1,\mathbf{r}_2,t)=D_1\nabla_1^2G_2(\mathbf{r}_1,\mathbf{r}_2,t)+D_2\nabla_2^2G_2(\mathbf{r}_1,\mathbf{r}_2,t). \tag{9}$$

Here $\nabla^2_{1(2)}$ is the tree-dimensional Laplace operator in coordinates $\mathbf{r}_1(\mathbf{r}_2)$. Being near one of the boundaries (spherical or cylindrical surface), $S(R_1)$ or $S(R_2)$ the particle gets into other conditions for its annihilation with another particle, in comparison with the case of a region without boundaries for the analytical Green function $G_2(\mathbf{r}_1,\mathbf{r}_2,t)$ is a more sophisticated problem. The absence of the annihilation term in (9) reduces its applicability only to the weak annihilation case. The following inequality for the rate amplitude can server as a suitable criterion for the weak annihilation regime within the studied problem $U_0=\max U(r_{12}):\ U_0<<D_{1(2)}/R^2_{1(2)}$. When the inequality is satisfied, the equation for the two-point Green function $G_2(\mathbf{r}_1,\mathbf{r}_2,t)$ is spited in two independent diffusion equations for each particle. Consequently, the Green function $G_2^{(0)}(\mathbf{r}_1,\mathbf{r}_2,t)$ is factorized with respect to the particle's coordinates: $G_2^{(0)}(\mathbf{r}_1,\mathbf{r}_2,t)=G_1(\mathbf{r}_1,t)G_1(\mathbf{r}_2,t)$.

Within the spherical frame with the z-axis being co-oriented with the magnetic moment vector **M** defining axial field in the gap, the Green function $G_1(r,\theta,\varphi,t)$ of each annihilating particle has the form

$$G_1(r,\theta,\varphi,t\,|\,r',\theta',\varphi')=\frac{3}{4\pi(R_2^3-R_1^3)}+\sum_{n=1}^{\infty}\exp\left[-D\left(\lambda_k^{(0)}\right)^2t\right]\frac{Z_{1/2}\left(\lambda_n^{(0)}r\right)Z_{1/2}\left(\lambda_n^{(0)}r'\right)}{4\pi\sqrt{rr'}\int\limits_{R_1}^{R_2}rZ^2_{1/2}\left(\lambda_n^{(0)}r\right)dr}+$$

$$+\sum_{n,l=1}^{\infty}\sum_{m=0}^{l}\exp\left[-D\left(\lambda_n^{(l)}\right)^2t\right]\frac{(2l+1)}{2\pi}\frac{(l-m)!}{(l+m)!}\frac{Z_{l+1/2}\left(\lambda_n^{(l)}r\right)Z_{l+1/2}\left(\lambda_n^{(l)}r'\right)}{\sqrt{rr'}\int\limits_{R_1}^{R_2}rZ^2_{l+1/2}\left(\lambda_n^{(l)}r\right)dr}\times \tag{10}$$

$$\times P_l^m(\cos\theta)\cdot P_l^m(\cos\theta')\cos m(\varphi-\varphi'),$$

here $Z_{l+1/2}(\lambda_n^{(l)}r)$ is a combination of the Bessel function $J_{l+1/2}(x)$ $N_{l+1/2}(x)$ of a semi-half index *l*+1/2

$$Z_{l+1/2}(\lambda_n^{(l)}r)=\left[\lambda_n^{(l)}J'_{l+1/2}(\lambda_n^{(l)}R_1)-J_{l+1/2}(\lambda_n^{(l)}R_1)/(2R_1)\right]N_{l+1/2}(\lambda_n^{(l)}r)-$$
$$-\left[\lambda_n^{(l)}N'_{l+1/2}(\lambda_n^{(l)}R_1)-N_{l+1/2}(\lambda_n^{(l)}R_1)/(2R_1)\right]J_{l+1/2}(\lambda_n^{(l)}r).$$

$P_l^m(\cos\theta)$ is the Legendre polynomials; $\lambda_n^{(l)}$ are the positive roots of the equation $\lambda_n^{(l)}\cdot Z'_{l+1/2}(\lambda_n^{(l)}R_2)-Z_{l+1/2}(\lambda_n^{(l)}R_2)/(2R_2)=0$.

Calculations based on the diffusion Green function (10) are complicated, so for the sake of illustration we assume that the moving molecule placed in the nanoreactor makes it diffusion walk in a certain plain within a circular area α which is a nanocell section passing through its diameter (Fig. 1a). In the circular symmetry case, which is due when the Green function does not depend on the angle φ the following equation holds for the radial Green function $G_1(r,t\,|\,r')$ of two-dimensional diffusion walk

$$G_1(r,t\,|\,r')=\frac{1}{\pi R^2}\left\{1+\sum_{k=1}^{\infty}\exp\left[-\frac{D}{R^2}\left(\mu_k^{(0)}\right)^2t\right]\frac{J_0\left(\mu_k^{(0)}r/R\right)J_0\left(\mu_k^{(0)}r'/R\right)}{J_0^2\left(\mu_k^{(0)}\right)}\right\}. \tag{11}$$

Here $\mu_k^{(n)}$ are positive roots of the equation $J'_n(\mu_k^{(n)})=0$; $J_n(x)$ is the Bessel functions of the first kind.

When a solution for equation (9) for two-particle Green function $G_2(\mathbf{r}_1,\mathbf{r}_2,t)$ is obtained, then the spin-selective biomolecular reaction rate constant $K(\mathbf{r}_1',\mathbf{r}_2')$ can be evaluated as follows

$$K(\mathbf{r}_1',\mathbf{r}_2') = \int_0^\infty dt \iint_{\Delta V_R} U(|\mathbf{r}_1-\mathbf{r}_2|)\frac{1}{2}\mathrm{Tr}\left\{\hat{P}_S,\hat{\rho}(\mathbf{r}_1,\mathbf{r}_2,t\,|\,\mathbf{B}(\mathbf{r}_1),\mathbf{B}(\mathbf{r}_2))\right\}_+ G_1(\mathbf{r}_1,t\,|\,\mathbf{r}_1')G_1(\mathbf{r}_2,t\,|\,\mathbf{r}_2')d^3r_1d^3r_2 . \quad (12)$$

Expression (12) provides an exact solution of the stated problem with the main emphasis on the influence of boundaries S_1, S_2 on the kinematics. Radius-vectors $\mathbf{r}_1',\mathbf{r}_2'$ in (12) define the initial positions of particles 1 and 2. Therefore, the specific rate $K(\mathbf{r}_1',\mathbf{r}_2')$ of the biomolecular reaction depends on the initial configuration of the particle pair $\mathbf{r}_1',\mathbf{r}_2'$. It was assumed that the T-T annihilation rate $U\left(|\mathbf{r}_1-\mathbf{r}_2|\right)$ in (12) is represented by subjected to the exponential law

$$U\left(|\mathbf{r}_1-\mathbf{r}_2|\right) = U_0\exp\left[-2\frac{|\mathbf{r}_1-\mathbf{r}_2|}{l}\right],$$

where *l* is the characteristic scale of the overlapping of interaction molecules electron shells.

2. Results and discussion

It is assumed that some porous media when wetting form a thin liquid layer impregnated with ferromagnetic particles due to the adhesion. This assumption allows one to create a model for two-dimensional diffusion walk of T-molecules in a circular region (Figure 1a) which simplifies further calculations. A magnetized ferromagnetic core creates a heterogeneous field within the nanostructure. To be exact, in the case of two-dimensional walk within a circular section α the nanoparticle magnetic field induction distribution reads $B_2(r) = B/r^3$ (Figure 1b).

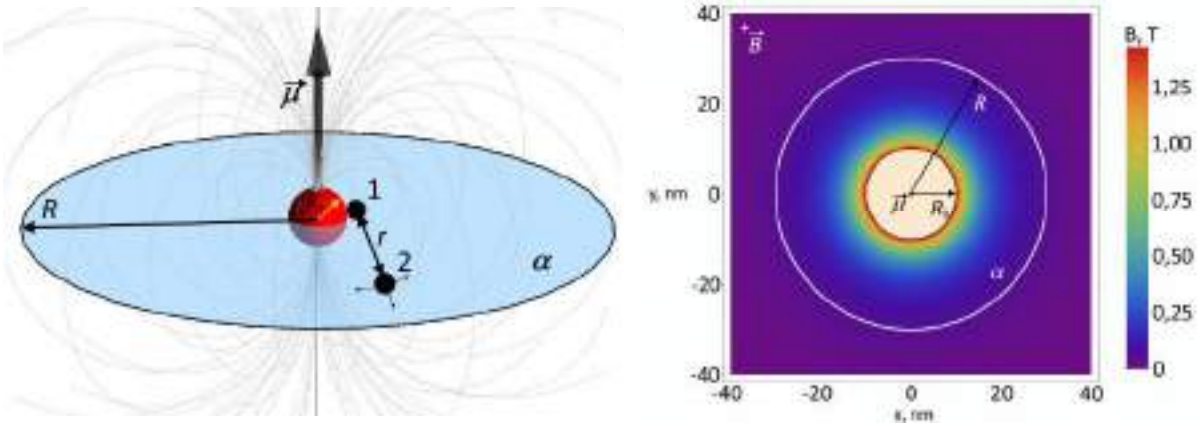

a) *b*)

Fig. 1. The structure of the studied system: the coherent T-T molecule pair-(1), (2) with the intermolecular distance *r* within a circular area α with the radius *R* containing a ferromagnetic particle in the center with the radius R_0 and the magnetic moment $\boldsymbol{\mu}$ ($\boldsymbol{\mu} = \mathbf{M}_0V$) (*a*); the distribution of the magnetic field induction B_2 generated by the ferromagnetic nanoparticle within the plane α given by $B_2(r) = B/r^3$ (*b*)

To study the influence of the ferromagnetic nanoparticle magnetic field (mainly, the influence which is due to the degree of its non-homogeneity) on the triplet-triplet excitation annihilation rate of excited molecules making diffusion walk in a proximity of such a particle we evaluated both space-time (Fig. 2) and time (Fig. 3-5) dependencies of the singlet matrix elements $\langle 00|\hat{\rho}_S(r,t)|00\rangle$ of the T-T pair spin density operator for various field values and molecular system parameters. Further we neglect the index *S* of the density operator $\hat{\rho}_S$, but we are to use indices *hom* or *het* to indicate homogeneity or heterogeneity of the field correspondingly. The radius *r* defines the position of the moving molecule with respect to the center of the nanoparticle. Heterogeneity of the magnetic field leads to the dependence of the population of the pair

.

singlet state $\langle 00|\rho_{het}(r,t)|00\rangle$ from the T-molecule coordinates. Results of calculations are presented on Fig. 2a and Fig. 2b. They show that the population is modulated by the T-molecule position both for weak residual fields $B<0.1$ T (Fig. 2a) and for strong residual fields (> 0.1 T) (Fig. 2b). In weak heterogeneous fields the influence of the ΔB -mechanism weakens, so states $|2\pm1\rangle$ and $|1\pm1\rangle$ are mixed mainly because of the Δg -mechanism.

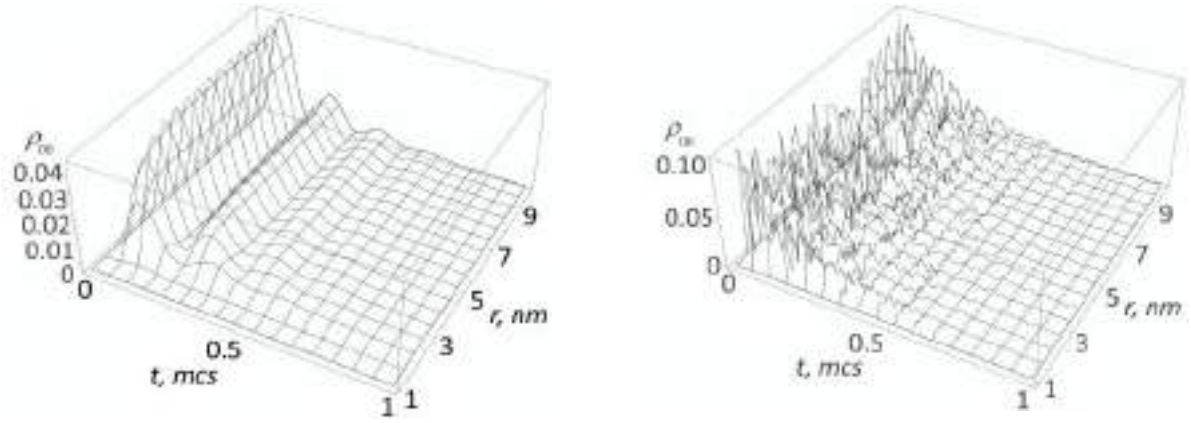

a) $B=10^{-4}$ T, $B_2(r)=B/r^3$ *b*) $B=0.1$ T, $B_2(r)=B/r^3$

Fig. 2. Evolution of the singlet T-T pair density population $\langle 00|\rho_{het}(r,t)|00\rangle=\rho_{00}$ placed in a residual magnetic field of the nanoparticle versus the position of the moving T-molecule. The following parameter values are used: $K_{-1}=10^7$ s^{-1}, $\omega_{exc}=10^7$ s^{-1}, $\Delta g=10^{-3}$, $\omega_{ss}^{(1)}=10^7$ s^{-1}, $\omega_{ss}^{(2)}=2\cdot10^7$ s^{-1}, $K_s=10^7$ s^{-1}

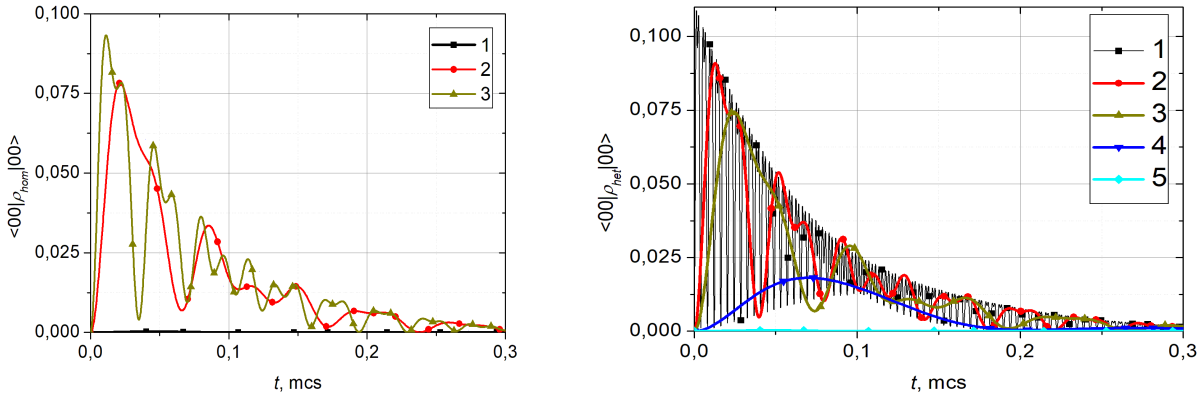

a) $B=B_2$: 0 (1), 1 (2) и 2 T (3) *b*) B: 10^{-2} (1), 10^{-3} (2), $5\cdot10^{-4}$ (3), 10^{-4} (4), 0 T (5); $B_2(r)=B/8$

Fig. 3. Kinetics of the singlet spin state population $\langle 00|\rho(r,t)|00\rangle$ of the T-T molecule pair at various values of the external magnetic field induction. (*a*) – non-magnetic nanoparticle, uniform magnetic field, (*b*) – ferromagnetic nanoparticle, inhomogeneous magnetic field. The following parameter values are used: $K_{-1}=10^7$ s^{-1}, $\omega_{exc}=10^7$ s^{-1}, $\Delta g=10^{-3}$, $\omega_{ss}^{(1)}=10^7$ s^{-1}, $\omega_{ss}^{(2)}=2\cdot10^7$ s^{-1}, $K_s=10^7$ s^{-1}, $r=2$ nm

The existence of an external heterogeneous field **B** and its ΔB-mechanism influence result in a significant growth of the oscillation frequency of the pair singlet state population $\langle 00|\rho_{het}(r,t)|00\rangle$. This fact is well-illustrated with Figure 3. The population oscillation frequency within a homogeneous external field with induction 1-2 T is ~0,14-0,25 MHz (Fig. 3a), while in a heterogeneous field of weak induction B~10^{-2} T it rises up to ~ 24 MHz (Fig. 3b). The oscillation frequency for the case $\langle 00|\rho_{het}(r,t)|00\rangle$ matches the frequency for the case of a heterogeneous field with an amplitude B of the order of (~1) mT. Therefore, ΔB-mechanism results are a significant growth of the population oscillation frequency by 4-5 orders of magnitude.

The growth of the exchange frequency ω_{exc} in the generalized model accounting for the field heterogeneity describes previously unknown results, namely, the increase of the population probability of the pair singlet state $\langle 00|\rho(r,t)|00\rangle$ both for homogeneous and heterogeneous fields (Fig. 4). It also should be noted, that the increase of the exchange frequency ω_{exc} up to 10^9 Hz in case of $\langle 00|\rho_{het}(r,t)|00\rangle$ results in an insignificant fall of the amplitude (about 2,5 %), while $\langle 00|\rho_{hom}(r,t)|00\rangle \to 0$ due to the effective action of the ΔB -mechanism.

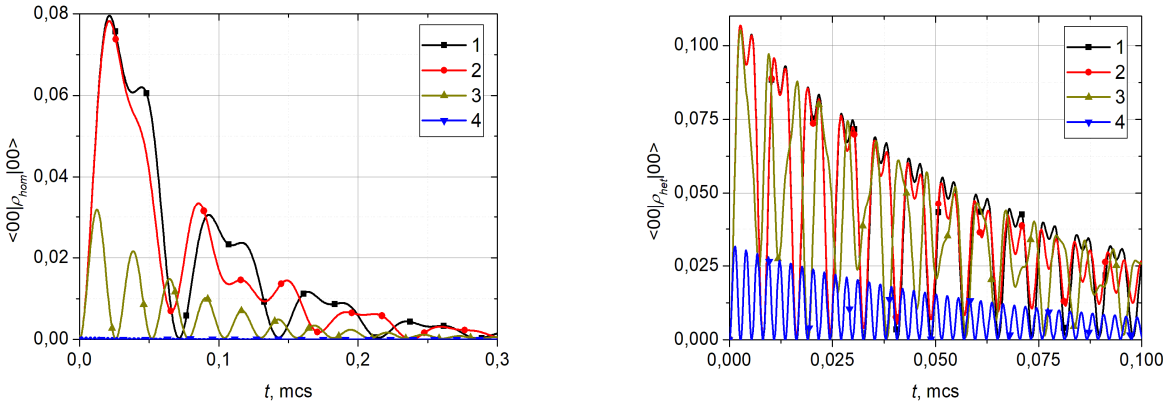

a) $B = B_2 = 1$ T; ω_{exc} : 10^6 (1), 10^7 (2), 10^8 (3), 10^9 (4) s^{-1}.

b) $B = 5 \cdot 10^{-3}$, $B_2(r) = 6{,}3 \cdot 10^{-4}$ T; ω_{exc} : 10^5 (1), 10^7 (2), 10^8 (3), 10^9 (4) s^{-1}.

Fig. 4. Kinetics of the spin singlet state population $\langle 00|\rho(r,t)|00\rangle$ of the T-T molecule pair at various values of the exchange frequency ω_{exc}. (*a*) – non-magnetic nanoparticle, uniform magnetic field, (*b*) – ferromagnetic nanoparticle, inhomogeneous magnetic field. The following parameter values are used: $K_{-1} = 10^7$ s^{-1}, $\Delta g = 10^{-3}$, $\omega_{ss}^{(1)} = 10^7$ s^{-1}, $\omega_{ss}^{(2)} = 2 \cdot 10^7$ s^{-1}, $K_s = 10^7$ s^{-1}, $r = 2$ nm

Elementary annihilation act rate K_s enters the matrix element $\langle JM|K|J'M'\rangle$ of the kinetic operator (Table 1). The increase of the rate K_s results in a decree of the amplitude of population $\langle 00|\rho(r,t)|00\rangle$ in an analogy with homogeneous (Fig. 5a) and heterogeneous magnetic field cases (Fig. 5b).

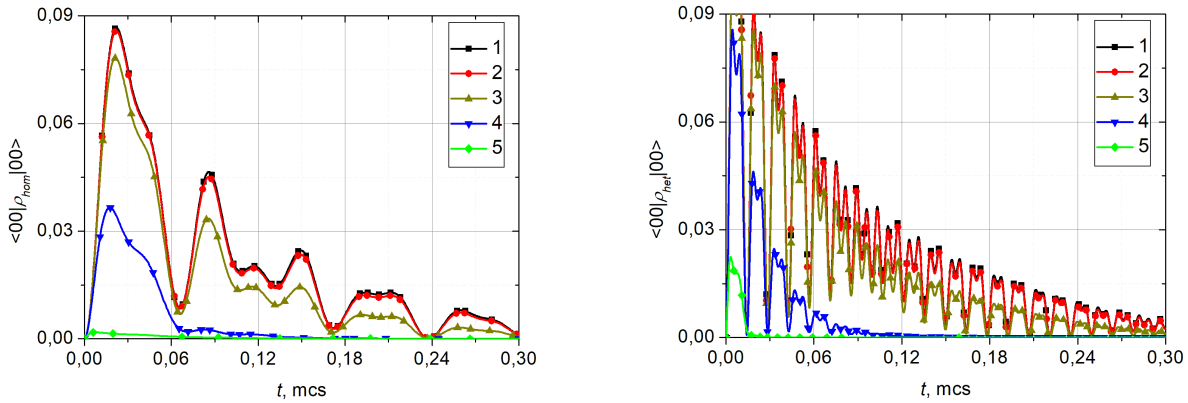

a) $B = B_2 = 1$ T; K_s : 10^5 (1), 10^6 (2), 10^7 (3), 10^8 (4), 10^9 (5) s^{-1}.

b) $B = 5 \cdot 10^{-3}$, $B_2(r) = 6{,}3 \cdot 10^{-4}$ T; K_s :10^5 (1), 10^6 (2), 10^7 (3), 10^8 (4), 10^9 (5) s^{-1}.

Fig. 5. Kinetics of the spin singlet state population $\langle 00|\rho(r,t)|00\rangle$ of the T-T molecule pair at various values of the elementary annihilation act rate K_s. (*a*) – non-magnetic nanoparticle, uniform magnetic field, (*b*) – ferromagnetic nanoparticle, inhomogeneous magnetic field. The following parameter values are used: $K_{-1} = 10^7$ s^{-1}, $\omega_{exc} = 10^7$ s^{-1}, $\Delta g = 10^{-3}$, $\omega_{ss}^{(1)} = 10^7$ s^{-1}, $\omega_{ss}^{(2)} = 2 \cdot 10^7$ s^{-1}, $r = 2$ nm

.

Moreover, calculations allow one to recover the dependency of the relative TTA (magnetic effect) rate change $\gamma(B)=[K(0)-K(B)]/K(0)$ from the magnetic field induction B (Fig. 6-8). The influence of the spin-spin interaction on the TTA reaction magnetic sensitivity results in a change of the interval where $\gamma(B)$ approaches asymptote (Fig. 6). This effect most clearly manifests itself in homogeneous fields (Fig. 6a). In a heterogeneous magnetic field, the effect is leveled out by the fast yield saturation due to the ΔB -mechanism (Fig. 6b). Figure 6 shows that the spin-spin interaction does not affect the form of curves $\gamma(B)$ for the frequencies $\omega_{ss}<10^7$ Hz. The modulation of the TTA reaction rate $\gamma(B)$ shows even more specific behavior in a proximity of either magnetic or non-magnetic nanoparticle when the T-molecules g-factor difference is changing (Fig. 7).

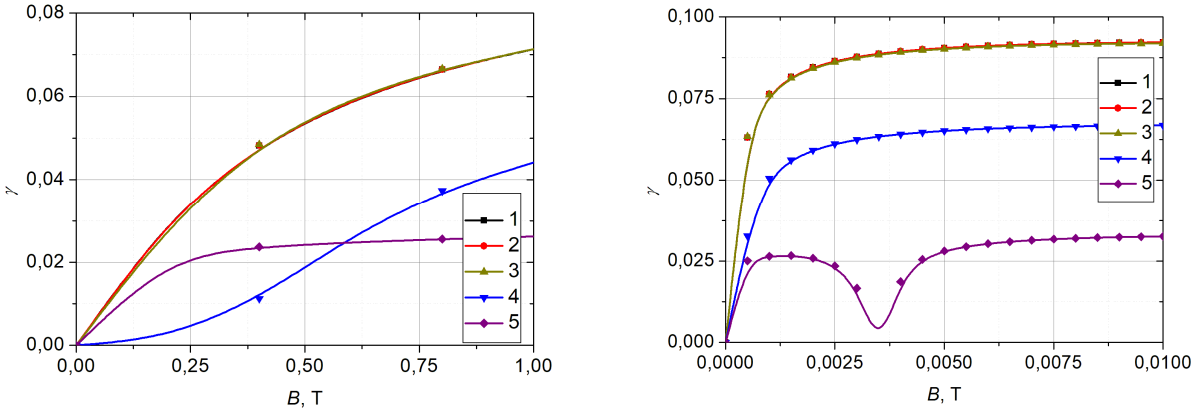

a) $B=B_2$; ω_{ss}: 10^5 (1), 10^6 (2), 10^7 (3), 10^8 (4), 10^9 (5) s^{-1}.

b) $B_2=B/r^3$; ω_{ss}: 10^5 (1), 10^6 (2), 10^7 (3), 10^8 (4), 10^9 (5) s^{-1}.

Fig. 6. The influence of the spin-spin interaction frequency ω_{ss} on the magnetic field effect $\gamma(B)$ within TTA reaction. (*a*) – non-magnetic nanoparticle, uniform magnetic field, (*b*) – ferromagnetic nanoparticle, inhomogeneous magnetic field. The following parameter values are used: $K_{-1}=10^7$ s^{-1}, $\omega_{exc}=10^7$ s^{-1}, $\Delta g=10^{-3}$, $K_s=10^7$ s^{-1}, $r'=2$ nm, $D=10^9$ nm^2/s, $R=10$ nm, $U_0=10^9$ s^{-1}, $r_0=0,5$ nm, $l=0,2$ nm, $a=0,99$

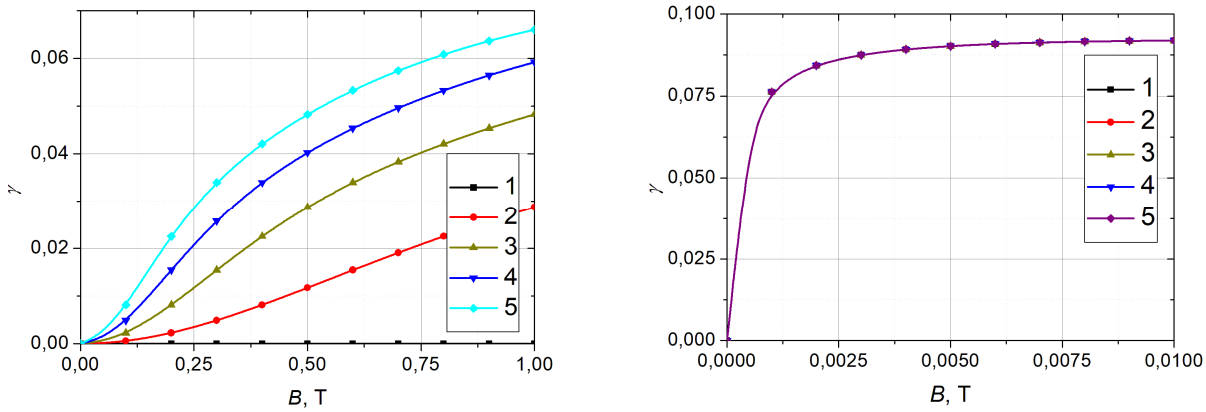

a) $B=B_2$; Δg: 0 (1), $2\cdot10^{-4}$ (2), $4\cdot10^{-4}$ (3), $6\cdot10^{-4}$ (4), $8\cdot10^{-4}$ (5)

b) $B_2=B/r^3$; Δg: 0 (1), $2\cdot10^{-4}$ (2), $4\cdot10^{-4}$ (3), $6\cdot10^{-4}$ (4), $8\cdot10^{-4}$ (5)

Fig. 7. The influence of the g-factors difference (Δg) of T-molecules on the magnetic field effect $\gamma(B)$ in TTA reaction. (*a*) – non-magnetic nanoparticle, uniform magnetic field, (*b*) – ferromagnetic nanoparticle, inhomogeneous magnetic field. The following parameter values are used: $K_{-1}=10^7$ s^{-1}, $\omega_{exc}=10^7$ s^{-1}, $\omega_{ss}^{(1)}=10^7$ s^{-1}, $K_s=10^7$ s^{-1}, $\omega_{ss}^{(2)}=2\cdot10^7$ s^{-1}, $r'=2$ nm, $D=10^9$ nm^2/s, $R=10$ nm, $U_0=10^9$ s^{-1}, $r_0=0,5$ nm, $l=0,2$ nm, $a=0,99$

In case of a heterogeneous magnetic field B_2 variations of Δg do not result in any observable changes for the magnetic effect $\gamma(B)$ (Fig. 7b). This feature is due to the suppressing action of the ΔB-mechanism in the presence of the weak Δg-mechanism. Diffusive Green functions (10)-(11) with reflective boundary conditions (at the boundary of the nanoreactor) were used for evaluation of the TTA reaction rate (12). Variations in the radius R of the nanoreactor circular area were the TTA processes occurs results in variations in the magnetic effect amplitude $\gamma(B)$ (Fig. 8). The spatial constraint of the T-molecules motion leads to their localization in the area of high magnetic field induction which, in turn, results in the increase of both reaction efficiency and magnetic response ($\gamma(B)$ ~26 %) in both cases.

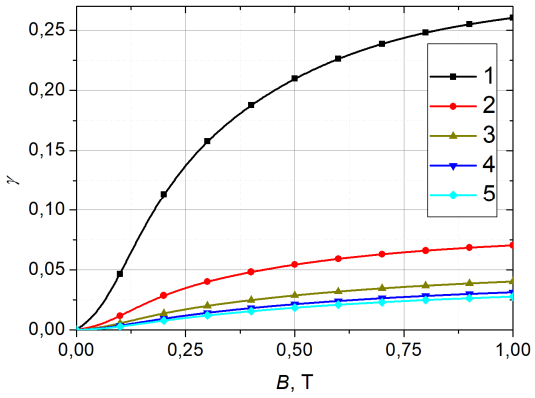

a) $B = B_2$; *R*: 5 (1), 10 (2), 15 (3), 20 (4), 25 (5) nm.

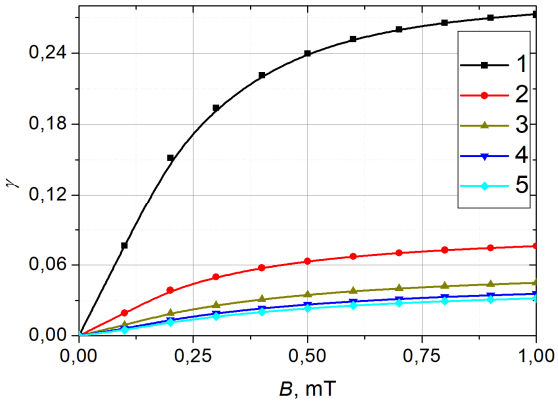

b) $B_2 = B/r^3$; *R*: 5 (1), 10 (2), 15 (3), 20 (4), 25 (5) nm.

Fig. 8. The influence of the radius *R* of the circular area α of the nanoreactor on the magnetic field effect $\gamma(B)$ in TTA reaction. (*a*) – non-magnetic nanoparticle, uniform magnetic field, (*b*) – ferromagnetic nanoparticle, inhomogeneous magnetic field. The following parameter values are used: $K_{-1} = 10^7$ s^{-1}, $\omega_{exc} = 10^7$ s^{-1}, $\Delta g = 10^{-3}$, $\omega_{ss}^{(1)} = 10^7$ s^{-1}, $\omega_{ss}^{(2)} = 2 \cdot 10^7$ s^{-1}, $K_s = 10^7$ s^{-1}, $r' = 2$ nm, $D = 10^9$ nm^2/s, $U_0 = 10^9$ s^{-1}, $r_0 = 0{,}5$ nm, $l = 0{,}2$ nm, $a = 0{,}99$

It should be noted that the increase of the radius *R* of the "reaction-diffusion" area alongside the diffusion coefficient *D* growth leads to a saturation of the reaction efficiency with respect to variation of *R* and *D*. This is due to the fact that the spin non-selective reaction rate rapidly approaches its asymptote and the T-T pairs spin dynamics remains relatively fast.

Conclusion

Magnetosensitivity of a reaction involving T-molecules in the most general case is affected by the inter-triplet electronic spin-spin interaction mechanism or the associated spin-relaxation mechanism. However, in the case of molecules high orientation mobility their chaotic reorientation can completely level out their anisotropic spin-spin interaction within the triplet. In an analogy with the spin radicals' case the reaction magnetic sensitivity can be driven by the Δg-mechanism of the magnetic response which is due to annihilation of T-molecules of various types. In homogeneous magnetic fields it can become the dominant factor generating the T-T pairs spin-dynamics. Consequently, within calculations of both pair singlet state population dynamics and the TTA specific rate magnetic effect we did account for the fine triplet energy structure associated with the spin-spin interaction operator $V_{SS} = -S_1 D_1 S_1 - S_2 D_2 S_2$ alongside the Δg-mechanism and the specific delta B-mechanism (or grad $B(\mathbf{r})$-mechanism). To put it otherwise, the influence of the field heterogeneity on the T-T molecular pair dynamics was taken into account. It was shown that it is ΔB-mechanism that can effectively influence the singlet state $\langle 00|\rho(r,t)|00\rangle$ population dynamics of T-T molecular pair and lead to a positive TTA reaction magnetic response both for multi-sorted and single-sorted molecules (for which $\Delta g = 0$). In other words, in a heterogeneous magnetic field the ΔB-

.

mechanism replaces the Δg -mechanism in its influence of the magnetic field, as it provides the dominant contributions to the reaction rate magnetic response in nanostructures containing ferromagnetic particles.

REFERENCES

1 Nidya Ch., Ting-Yi Ch., Ping-Tsung H., Ten-Chin W., Tzung-Fang G. The triplet-triplet annihilation process of triplet to singlet excitons to fluorescence in polymer light-emitting diodes. *Organic Electronics*, 2018, Vol.62, pp.505-510. https://doi.org/10.1016/j.orgel.2018.06.021

2 Bin H., Yue W., Zongtau Zh., Sheng D., Jian Sh. Effects of ferromagnetic nanowires on singlet and triplet exciton fractions in fluorescent and phos-phorescent organic semiconductors. *Applied Physics Letters*, 2006, Vol. 88, pp. 022114. https://doi.org/10.1063/1.2162801

3 Toshihiro Sh. Effect of High Magnetic Field on Organic Light Emitting Diodes. *Organic Light Emitting Diode – Material, Process and Devices*, 2011, pp. 311-322. https://doi.org/10.5772/20743

4 Qiaohui Zh., Miaomiao Zh., Yaxiong W., Xiaoguo Zh., Shilin L., Song Zh., Bing Zh. Solvent effects on the triplet–triplet annihilation upconversion of diiodo-Bodipy and perylene. *Physical Chemistry Chemical Physics*, 2017, Vol. 19, pp. 1516-1525. https://doi.org/10.1039/C6CP06897A

5 Kolosov D.A., Deryabin M.I. Kinetics of annihilation of triplet excitations and decay of delayed fluorescence for isolated 1,12-benzoperylene pairs. *Journal of Applied Spectroscopy*, 2011, Vol. 78, No. 4, pp. 601-604. https://doi.org/10.1007/s10812-011-9504-z

6 Samusev I.G., Bruchanov V.V., Ivanov A.M., Labutin I.S., Loginov B.A. Heterogeneous triplet-triplet annihilation of erythrosine and anthracene molecules on a fractal anodized aluminum surface. *Journal of Applied Spectroscopy*, 2007, Vol. 74, No. 2, pp. 230-236. https://doi.org/10.1007/s10812-007-0036-5

7 Zarezin A.B., et al. Study of photophysical processes involving organic dye molecules and superparamagnetic nanoparticles in thin polymer films. *Kazan science*, 2011, No. 4, pp. 10-13. [in Russian]

8 Kim H., Weon S., Kang H., et al. Plasmon-Enhanced Sub-Bandgap Photocatalysis via Triplet–Triplet Annihilation Upconversion for Volatile Organic Compound Degradation. *Environmental Science & Technology*, 2016, Vol. 50, No. 20, pp. 11184-11192. https://doi.org/10.1021/acs.est.6b02729

9 Poorkazem K., Hesketh A.V., Kelly T.L. Plasmon-Enhanced Triplet–Triplet Annihilation Using Silver Nanoplates. *The Journal of Physical Chemistry C*, 2014, Vol. 118, No.12, pp. 6398-6404. https://doi.org/10.1021/jp412223m

10 Uemura T., Furumoto M., Nakano T., et al. Local-plasmon-enhanced up-conversion fluorescence from copper phthalocyanine. *Chemical Physics Letters*, 2007, Vol. 448, pp. 232-236. https://doi.org/10.1016/j.cplett.2007.09.084

11 Hervald A.Yu., Gritskova I.A., Prokopov N.I. Synthesis of magnetic-containing polymer microspheres. *Success of chemistry*, 2010, Vol. 79, No. 3, pp. 249-260. [in Russian]

12 Bronstein L.M., Sidorov S.N., Walecki P.M. Nanostructured polymer systems as nanoreactors for the formation of nanoparticles. *Success of chemistry*, 2004, Vol. 73, No. 5, pp. 542-558. [in Russian]

13 Mamoru M., Yuri Ya., Tadashi N., Kazuhisa Ya. Anomalous Pore Expansion of Highly Monodispersed Mesoporous Silica Spheres and Its Application to the Synthesis of Porous Ferromagnetic Composite. *Chemistry of Materials*, 2008, Vol. 20, No. 14, pp. 4777-4782. https://doi.org/10.1021/cm702792e

14 Jinwoo L., Sunmi J., Yosun H., Je-Geun P., Hyun Min P., Taeghwan H. Simple synthesis of mesoporous carbon with magnetic nanoparticles embedded in carbon rods. *Carbon*, 2005, Vol. 43, No. 12, pp. 2536-2543. https://doi.org/10.1016/j.carbon.2005.05.005

15 Kucherenko M.G., Neyasov P.P. Features of spin dynamics and annihilation of triplet molecular excitations in nanoreactors with ferromagnetic particles. *Chemical Physics and Mesoscopy*, 2018, Vol. 20, No. 1, pp. 33-48. [in Russian]

16 Heer W.A. de, Knight W.D., Chou M.Y., Cohen M.L. Electronic Shell Structure and Metal Cluster. *Solid State Physics*, 1987, Vol. 40, pp. 93-181. https://doi.org/10.1016/S0081-1947(08)60691-8

17 Afanas'ev A.M., Suzdalev I.P., Gen M. Ya., et al. Investigation of super-paramagnetism of ferromagnetic particles by Mossbauer spectroscopy. *Soviet Physics Jetp*, 1970, Vol. 31, No. 1, pp. 65-69.

18 Amulyavichu A.P., Suzdalev I.P. Investigation of the superparamagnetic properties of ultrafine iron particles by Mossbauer spectroscopy. *Zh. Eksp. Teor. Fiz,*. Vol. 64, pp. 1702-1711.

Article accepted for publication 30.11.2022

DOI 10.31489/2022No4/17-21

UDC 620.22

EFFECT OF HIGH-PRESSURE TORSION ON MICROSTRUCTURE CHANGES IN MICROALLOYED STEEL

Volokitina I.E.[1], Naizabekov A.B. [1], Volokitin A.V.[2]

[1]Rudny Industrial Institute, Rudny, Kazakhstan, irinka.vav@mail.ru
[2] Karaganda Industrial University, Temirtau, Kazakhstan

The most common method of manufacturing parts is metal pressure treatment, as a result of which the entire reserve of strength and ductility of the material is not exhausted. Therefore, the issues of the influence of plastic deformation on the cyclic durability and endurance limits of steel rings are relevant. In this article experimental studies of the effect of high pressure torsion in a die of new design on the evolution of the microstructure and the change of mechanical properties have been carried out. As a result, the fundamental possibility and efficiency of using the proposed method for the formation of ultrafine grained structure and increasing the strength properties of steel rings has been proved. Strain was carried out at ambient temperature in six passes. The strain resulted in an ultrafine-grained structure with an average grain size of 0.5 μm and a great number of large-angle boundaries. The strength properties of microalloyed steel increased almost threefold compared to the initial state, the microhardness also increased threefold, i.e. increased from 760 MPa in the initial state to 1935 MPa after strain. The greatest increase in strength properties occurred in the first 3 cycles of strain.

Keywords: severe plastic deformation, microstructure, high pressure torsion, steel, mechanical properties

Introduction

The desire for the highest possible efficiency in the production and use of components is reflected in the growing development of complex production processes and specialized materials. For the development of production processes, this means a tendency to reduce the number of different production steps while using materials as efficiently as possible. In terms of material performance, against a background of increasingly important, lightweight construction, high strength with good ductility is of great importance [1,2]. Most manufacturing processes for processing metallic materials cause local or global changes in material properties. These production properties, in turn, can be used purposefully to increase component performance or decrease material usage in reverse order. Thus, by adapting the manufacturing process to purposefully tune certain local material properties, synergistic effects can be used to improve overall component production efficiency.

The dynamic development of various industries, including aviation and mechanical engineering, as well as the ever-increasing requirements for structural materials contribute to the improvement of research on improving their mechanical properties. One of the ways to improve mechanical properties is to refine the material structure.

Ultrafine grained and nanocrystalline materials have been the subject of extensive research for a long time, since their mechanical properties allow us to expect great potential as structural materials [3-7]. To expand the possibilities of using ultrafine-grained materials as structural and functional materials, to make products with unique mechanical and physical properties, it is necessary to develop a method that would allow obtaining semi-finished products with improved characteristics. These include large cross-section, uniform grain size equiaxed ultrafine grained structure in any cross-section, high proportion of large-angle grain boundaries, and without sharp texture and areas with crystallo-graphically close grain orientation. The new method should take into account the factory realities, i.e. it should be easily adaptable to the existing press equipment equipped with simple and inexpensive technological tooling, and have market potential, which implies minimization of the introduced strain energy per unit mass of the ultrafine-grained product.

Such a method, apparently, should be sought among cyclic methods of deformation processing of metals and alloys, which include comprehensive isothermal forging, equal channel angular pressing (ECAP), helical extrusion and others that allow during the deformation processing to preserve or restore the original three-dimensional shape of the blank, regardless of the degree of deformation [8-15].

.

One such method is high-pressure torsion (HPT). In the process, shear strains are introduced into flat disc specimens by torsion under high hydrostatic pressure stresses. During the process, the sample is placed between two dies and twisted by the rotation of one die or the opposite rotation of both dies [16]. Grain size grinding in the HPT process is generally slightly more efficient than in the ECAP process, so a finer grain structure and higher mechanical properties can be obtained through this method [17,18]. However, although extensive research has been carried out in this area, the behavior and fundamental principles are not yet fully understood because, for example, such materials have extraordinary strength. The ductility, though, is too low, and also discs treated in this way have anisotropic properties between the center and the edges. As a result of the analysis of scientific and patent literature, the high-pressure torsion technology was selected as the most optimal processing technology for ring workpieces. However, this technology is most often applied to disk-shaped workpieces. So the next stage of research is to develop a special design of the die allowing to implement this process of severe plastic deformation, as well as to assess the possibility of stable flow of the process.

As is known, during high-pressure torsion, the movement of the straining tool consists of two types: translational and rotational. Presses are ideally suited as a working mechanism to implement this method, allowing for high hydrostatic pressure during compression. However, the main difficulty is the need to perform the torsion operation along the axis of the workpiece. This requires a certain torque to be transmitted to the straining tool, which is often not possible due to the design features of most presses. So the only possible option in this case is to ensure the torsion of the straining tool at a constant rectilinear motion of the press punch. The solution to this technical problem can only be realized in practice with a compound straining tool that includes both displacement and rotation units.

On the basis of modeling in the software package Deform given in papers [20-22] drawings of design have been developed. The design consists of several parts: the upper striker which is driven by the progressive motion of the press; the lower striker which is driven by the progressive motion of the upper striker and the die. There are 4 periodic spiral shaped notches on the bottom edge of the upper striker. A cylindrical hole is provided in the center of the upper striker for the rod of the straining element and to ensure alignment of both strikers. The lower striker has several steps. This design solution is necessary because in this case we are talking about straining a circular workpiece and not a disk workpiece (Fig. 1).

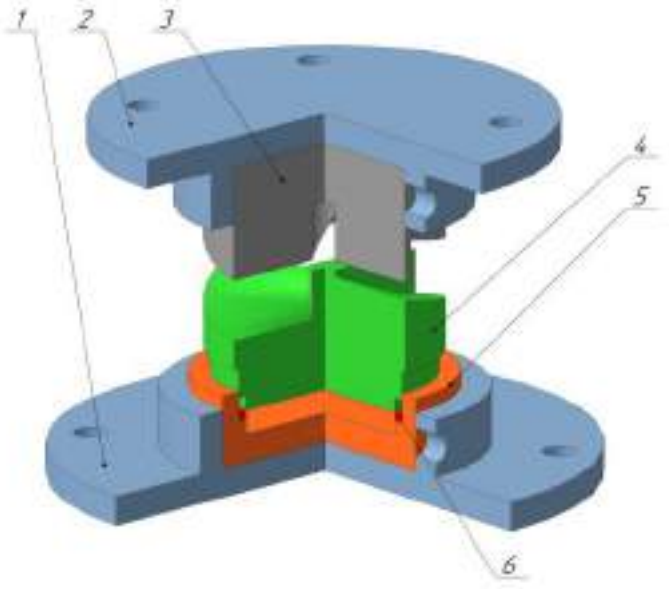

Fig.1. General view of the complete construction: 1 - bottom carrier, 2 - top carrier, 3 - upper striker, 4 - lower striker, 5 - matrix, 6 - piston ring.

The purpose of this work is to study the effect of high-pressure torsion in dies of new design on the structure and properties of 06MBF steel.

1. Materials and Methods

The initial workpiece had a ring shape with a diameter of 76 mm, a width of 3.5 mm, and a thickness of 3 mm. Steel 06MBF (Fe-0,1Mo-0,1V-0,06Nb-0,09C, wt.%) in the initial ferrite state was chosen as an object of the study. Initial workpieces of 06MBF steel were quenched at 910°C (15 min.), followed by high tempering at 660°C (30 min.). Assembly of the structure and the experiment itself was carried out in the laboratory on a single-column hot-stamping crank press model PB 6330-02, the force of which is 1000 kN. The strain was carried out at room temperature. Number of strain cycles is 6. To verify the ability to maintain the microstructure and mechanical properties during heating, the specimens were subjected to heating after strain. For this purpose, the samples after the HPT were cut into thin plates 10 mm thick and exposed to 450 - 600°C for 15 min with cooling in water. The fine structure was studied on a JEM 2100 transmission electron microscope. Thin foil for microstructure study was prepared by thinning with electrolitic polishing in an electrolyte of 400 ml H_3PO_4 and 60 g CrO_3 at room temperature and 20V, the current density was 2.5A/cm^2.

Mechanical tests for uniaxial tension were performed at ambient temperature on Instron 5882 machine with a strain rate of 1.0 mm/min. The tensile specimen were prepared according with method described in [23]. The strain of the sample was measured by an Instron strain gauge. According to the results of tests, the strength and ductility characteristics were determined: yield strength, tensile strength, and elongation.

Micromechanical properties were monitored during all periods of the study by measuring the microhardness. To measure the microhardness, an imprint was made on the sample surface under static load in accordance with GOST 9450-76. The indenter was a diamond tip in the form of a square pyramid with a square base. The load was 1 N. The root mean square error of the micro-hardness determination on many prints is an indication of the accuracy of the instrument. The error in the mechanical tests did not exceed 3%.

2. Results and discussion

In the initial state, the structure of unstrained samples consists of ferrite grains, which inherited the morphology of batch martensite, after quenching, with a grain size of 18 μm (Fig. 2a). High-pressure torsion straining resulted in intensive dispersion of the structural components down to 0.5 μm (Fig. 2b). The grain boundaries are blurred. The electronograms shown in Figure 2 are a system of reflexes with azimuthal blurs and broadened X-ray lines. This indicates a high level of internal stresses in the grains. On the electronogram after strain by the HPT method, the lines have a circular character with clearly distinguishable individual reflexes evenly distributed throughout the ring (Fig. 2b). This indicates the presence of high-angle misorientations between the structural elements from which the electronogram was obtained.

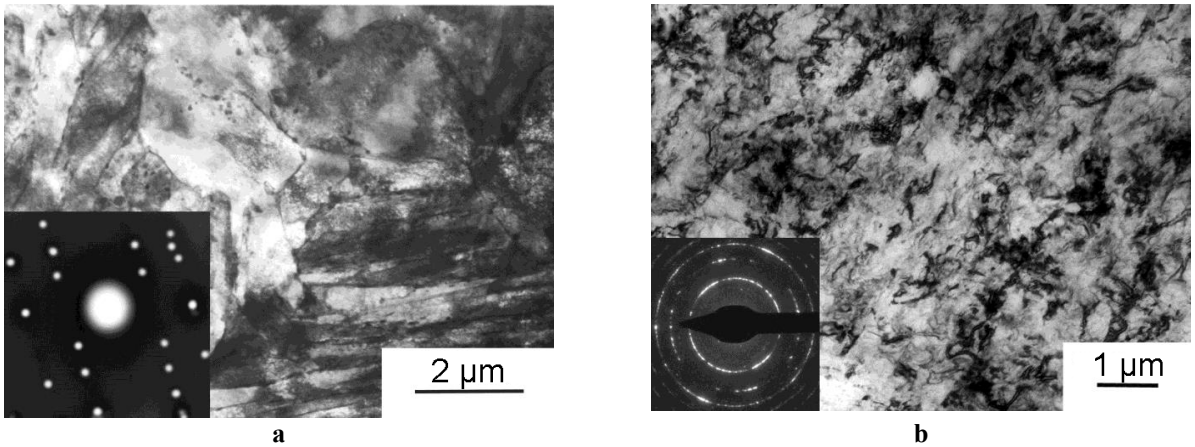

Fig.2. Microstructure of 06MBF steel: a) – initial state; b) – after 6 cycles of deformation.

Figure 3a shows that heating the samples to 450°C does not lead to a significant increase in grain; the structure retains the ultrafine grain structure with an average grain size of 0.6 μm. The electronogram still has a circular character. Increasing the temperature to 500°C leads to a return process, the grain size increases to 1 μm (Fig. 3b). Grain boundaries become equilibrium, dislocation density decreases. Heating to 550°C leads to the beginning of recrystallization processes. This can be seen in the nascent grains, the average grain size is about 2 μm.

.

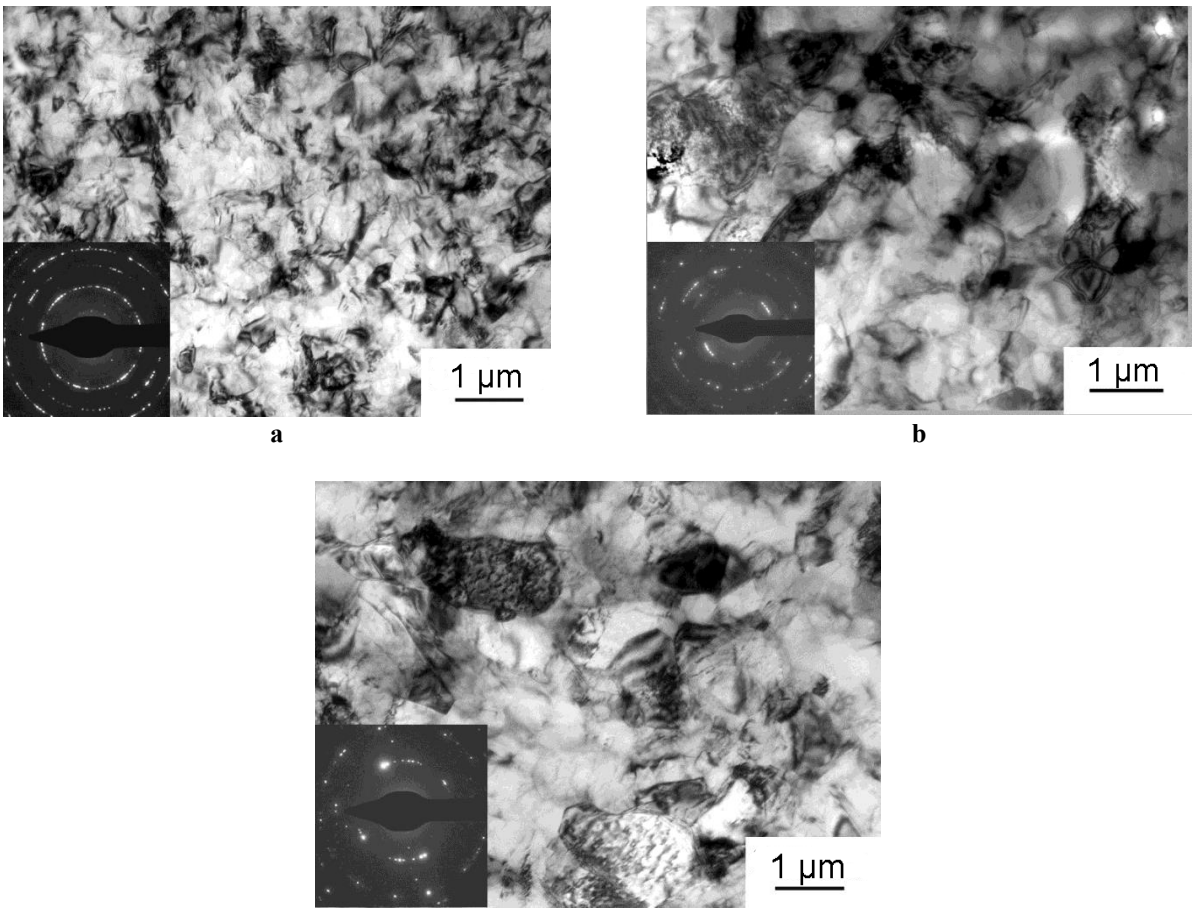

Fig.3. Microstructure of 06MBF steel after heating: a) – 450°C; b) – 500°C; c) – 550°C.

Tensile tests showed that the resulting ultrafine-grained structure has improved strength properties. The results in the initial state are: yield strength is 263 MPa and tensile strength is 465 MPa, and relative elongation is 32%. The formation of ultrafine grained structure after 6 cycles of strain by the HPT method leads to an increase in the ultimate strength up to 1315 MPa compared to the initial state. The yield strength increases to 1064 MPa. The value of ductility decreases sharply compared to the initial state up to 14%.

The microhardness results correlate with the mechanical tensile test data and indicate that the HPT in the new die allows for a fairly uniform hardness across the entire cross-section of the ring. After 6 cycles of strain by the HPT method, the microhardness increases almost threefold from 760 MPa to 1935 MPa as compared to the initial state. In this case, the main increase in hardness falls on the first 3 passes - 65%.

Conclusion

The study confirmed the pattern of strain-hardening of microalloyed steel rings with an increase in the number of strain cycles. Significant changes in microstructure initiated by high-pressure torsion in a new kind of die allowed to achieve the following most important results:

1. The electron microscopic analysis showed that the strain by torsion under high pressure leads to intensive dispersion of structural components from 18 to 0.5 μm. And the obtained ultrafine grain structure is preserved when heated up to 450°C.

2. The tensile tests showed that the obtained ultrafine-grained structure has increased strength properties. The results of microhardness determination correlate with the data of mechanical tensile tests and testify to the fact that the HPT in the new die allows to obtain a sufficiently homogeneous hardness over the entire cross section of the ring.

REFERENCES

1 Surzhikov A.P., Lysenko E.N., Malyshev A.V., Petrova A., Ghyngazov S.A., Aimukhanov A.K. Phase transformations in ferrites during radiation-thermal sintering. *Eurasian phys. tech. j,* 2020, Vol.17, No.1, pp. 144-153. doi:10.31489/2020No1/26-34

2 Alizadeh M., Samiei M. Fabrication of nanostructured Al/Cu/Mn metallic multilayer composites by accumulative roll bonding process and investigation of their mechanical properties. *Materials & Design,* 2014, Vol. 56, pp. 680–684. http://dx.doi.org/10.1016/j.matdes.2013.11.067

3 Valiev R.Z., Estrin Y., Horita Z., et al. Producing bulk ultrafine-grained materials by severe plastic deformation: ten years later. *JOM*. 2016, Vol. 68, pp.1216-1226. doi:10.1007/s11837-006-0213-7

4 Kasenov B.K., Kasenova Sh.B., Sagintaeva Zh.I., et al. Synthesis and X-ray investigation of novel nanostructured copper-zinc manganites of lanthanum and alkali metals. *Eurasian phys. tech. j.*, 2021, Vol. 18, No. 1, pp. 29-33. doi: 10.31489/2021No1/29-33

5 Lezhnev S., Panin E., Volokitina I. Research of combined process rolling-pressing influence on the microstructure and mechanical properties of aluminium. *Advanced Materials Research*, 2013, Vol.814, pp. 68-75. doi:10.4028/www.scientific.net/AMR.814.68

6 Furukawa M., HoritaZ., Langdon T.G. Application of equal-channel angular pressing to aluminum and copper single crystals. *Materials Science Forum,* 2007, Vols. 539-543, pp. 2853-2858. doi::10.4028/www.scientific.net/MSF.539-543.2853

7 Polyakov A.V., Semenova I.P., Raab G.I. Peculiarities of ultrafine-grained structure formation in Ti Grade-4 using ECAP-Conform. *Advanced Materials Science,* 2012, Vol.31, pp. 78-84.

8 Lezhnev S.N., Naizabekov A.B., Panin E., Volokitina I.E. Influence of combined process “rolling-pressing” on microstructure and mechanical properties of copper. *Procedia Engineering,* 2014, Vol.81, pp. 1499 – 1505. doi: 10.1016/j.proeng.2014.10.180

9 Naseri R., et al. An experimental investigation of casing effect on mechanical properties of billet in ECAP process. *International Journal of Advanced Manufacturing Technology,* 2017, Vol. 90, pp. 3203–3216. doi:10.1007/s00170-016-9658-1

10 Murashkin M.Yu., et al. Enhanced mechanical properties and electrical conductivity in ultrafine-grained Al alloy processed via ECAP-PC. *J. Mater. Sci.* 2013, Vol. 48, pp. 4501-4509. DOI:10.1007/s10853-013-7279-8

11 Xu C., Horita Z., Langdon T.G. The evolution of homogeneity in processing by high-pressure torsion. Acta Materialia, 2007, Vol.55, pp. 203-212. doi: 10.1016/j.actamat.2006.07.029

12 Raab G., Valiev R., Lowe T., Zhu Y. Continuous processing of ultrafine grained A1 by ECAP-Conform. *Mater. Sci. and Eng.,* 2004, Vol. 382, pp. 30–34. doi:10.1016/j.msea.2004.04.021

13 Dao M., Lu L., Asaro R., Hosson J., Ma E. Toward a quantitative understanding of mechanical behavior of nanocrystalline metals. *Acta Materialia*, 2007, Vol. 55, pp. 4041-4065. doi:10.1016/J.ACTAMAT.2007.01.038

14 Lezhnev S., Volokitina I., Koinov T. Research of influence equal channel angular pressing on the microstructure of copper. *Journal of Chemical Technology and Metallurgy,* 2014, Vol. 49, pp. 621-630.

15 Chukin M.V., Polyakova M.A., Emaleeva D.G., Gulin A.E. Creating UltrafineGrain Structure in High Strength Bimetallic Steel–Copper Products. *Steel in Translation*, 2014, Vol. 44, No. 4, pp. 320–323.

16 Zhilyaev A., Langdon T. Using high-pressure torsion for metal processing: Fundamentals and applications. *Progress in Materials Science*, 2008, Vol. 53, pp. 893-979. doi:10.1016/J.PMATSCI.2008.03.002

17 Kawasaki M., Ahn B., Lee H.J., et al. Using high-pressure torsion to process an aluminum–magnesium nanocomposite through diffusion bonding. *J. Mater. Res*., 2015, Vol. 31, pp. 88-99. doi:10.1557/jmr.2015.257

18 Volokitina I.E., Volokitin A.V., Panin E.A., Latypova M.A., Kassymov S.S. Microstructure evolution of steel-aluminum wire during deformation by "equal-channel angular press-ing-drawing" method. *Eurasian phys. tech. j.,* 2022, Vol.19, No.1, pp. 73-77. doi:10.31489/2022No1/73-77

19 Choi I., Schwaiger R., Kurmanaeva L., Kraft O. On the effect of Ag content on the deformation behavior of ultrafine-grained Pd-Ag alloys. *Scripta Materialia*, 2009, Vol.61, pp.64-67. doi:10.1016/j.scriptamat.2009.03.007

20 Horita Z., Fujinami T., Langdon T. The potential for scaling ECAP: Effect of sample size on grain refinement and mechanical properties. *Materials Science and Engineering A*., 2001, Vol. 318(1-2), pp. 34-41. doi:10.1016/S0921-5093(01)01339-9

21 Volokitin A., Volokitina I., Panin E., Naizabekov A., Lezhnev S. Strain state and microstructure evolution of AISI-316 austenitic stainless steel during high-pressure torsion (HPT) process in the new stamp design. *Metalurgija,* 2021, Vol. 60(3-4), pp. 325-328.

22 Volokitin A., Naizabekov A., Volokitina I., Lezhnev S., Panin E. Thermomechanical treatment of steel using severe plastic deformation and cryogenic cooling. *Mater. Letters,* 2021, 304, 130598. doi:10.1016/j.matlet.2021.130598

23 Erbel S. Mechanical properties and structure of extremely strain-hardened copper. *Metals Technology,* 1979, Vol.6, pp. 482-486.

Article accepted for publication 19.10.2022

.

DOI 10.31489/2022No4/22-27

UDC:539.2; 621.315.61

INFLUENCE OF IONIZING RADIATION ON THE DIFFUSE REFLECTION SPECTRA OF STEATITE CERAMICS SNC

Ashurov M.Kh., Nuritdinov I., Dzhumanov S., Saidakhmedov K.Kh.*

Institute of Nuclear Physics of the Academy of Sciences of Uzbekistan, Tashkent, Uzbekistan,
skhahramon@ yandex.ru

In this article, the radiation defects induced in steatite ceramics type- SNC- irradiated with high doses of gamma-rays of ^{60}Co source and mixed reactor n^o-gamma-irradiation were studied using optical spectroscopy, i.e. diffuse reflection method. An analysis of the results of the diffuse reflection spectra showed that some structural defects are formed under gamma-irradiation. These are oxygen vacancies, unbound oxygen atoms, and E^1 - centers (a three-coordinated silicon atom that has captured an electron) in the ultraviolet region of the spectrum. In the visible region of the spectrum, the types of hole centers are different. After decomposing the spectrum of the visible region into Gaussians, it was found that in this region of the spectrum, with n^o –gamma- irradiation of the reactor, in comparison with gamma-irradiation, various types of hole centers - (O-Me, Me-metal) are additionally formed. The efficiency of creating these structural defects in n^o-gamma-reactor irradiated samples was higher compared to gamma irradiated samples.

Keywords: steatite ceramics type-SNC, diffuse reflection, gamma-rays, n^o-gamma-irradiation, V-type hole centers.

Introduction

There is a growing need in the nuclear power industry for materials suitable for use in high radiation fields. In addition, there is the problem of effectiveness in using existing materials in extreme conditions. In this aspect, ceramic dielectrics have a special rank, including magnesian ceramics based on $MgSiO_3$, i.e. steatite ceramics. Since in the future the main energy industry is connected with nuclear energy, its role is naturally great in nuclear and thermonuclear energy. In this industry, in some aspects, ceramics is an indispensable material and has been used for a long time. For example, ceramic products effectively work in the shell of a sealed zone of localization of an accident at a nuclear power plant under the conditions of complex exposure to decontaminating solutions and intense gamma radiation, as fire barriers in cable corridors, in the zone of increased radiation of a nuclear reactor at high temperatures, under conditions of powerful neutron fluxes. and other types of radiation. However, radiation processes in ceramic materials haven't been entirely studied in comparison with other dielectrics. Therefore, the study of radiation-stimulated processes in ceramic materials is relevant both from a scientific and application point of view.

The study of the effect of higher doses of γ-radiation on steatite ceramics SK-1 and SNCs showed that at higher doses of γ-radiation ($\geq 10^8$ R (8.8×10^7Rad) in these types of ceramics, structural defects with high thermal stability are formed [1-2]. The aim of this work is to study the nature of defects formed under the action of high doses of γ-radiation by the diffuse reflection (DR) method, as well as to compare them with n^o-γ-irradiated samples of the nuclear reactor in steatite ceramics of the SNC types of ceramics compared to γ-irradiation.

1. Samples and experimental methods

Samples of ceramics of the SNCs type and, for comparison, SK-1 were studied as well. The ceramics are based on crystals of magnesium metasilicate-$MgSiO_3$ and glass of complex composition. The average grain size of crystals is 3-8 microns and occupies 60-70% of the volume of ceramics. The orthorhombic pyroxene enstatite (i.e. the crystalline phase magnesium metasilicate-$MgSiO_3$) belongs to the class of chain silicates. Its structure is well described on the basis of the concept of poling polyhedral: SiO_4–tetrahedron and MgO_6-octahedron (Fig. 1). SiO_4 tetrahedra are linked through common oxygen vertices into endless

zigzag chains $[Si_2O_6]_\infty$. Neighboring chains are not connected to each other and stretch in parallel, and in each individual chain the tetrahedra look either up or down, and in neighboring chains, the tetrahedra look in opposite directions. But the main core of the structure is zigzag chains of MgO_6-octahedra connected by edges, which form odd floors of the overall structure. In even floors, $[Si_2O_6]_\infty$chains are located, thus forming a single structure of the crystal phase of magnesium metasilicate $MgSiO_3$ [3].

The difference in these ceramics lies in the composition of the glass phases. Additionally, the following oxides CaO (0.52 wt%) ZnO (17 wt%) Na_2O (0.13 wt%) are present in the composition of the glass phase of SNC ceramics (Table 1). For 100%, the composition of the glass phase itself is taken, and not its relation to the composition of ceramics, see Table 1 [4,5]. The studied samples had dimensions of $10\times10\times1mm^3$, and the surface of the samples was subjected to polishing to achieve the same surface diffuseness. The samples were irradiated with γ-quanta of the ^{60}Co isotope ($E_{av\gamma}\approx1.25$ MeV), doses from 10^6 to 1.5×10^{10}R ($8.8\times10^5 \div 1.32\times10^{10}$Rad), and neutrons in the channel of the WWR-SM reactor of the Institute of Nuclear Physics of the Academy of Sciences of the Republic of Uzbekistan with fluences $f\sim10^{17}\div10^{20}$ n/cm^2. The traditional optical method for studying color centers (CC) in crystals, based on the study of optical absorption (OA) spectra, is not suitable for most ceramic dielectrics, which strongly absorb and scatter light. Therefore, DR spectra, which in the general case are inversely proportional to the degree of absorption of the medium, can be used to estimate the absorption.

Table 1. The phase-mineralogical composition of steatite materials and chemical composition of glass according to [4]

Materials	Crystal phase ($MgSiO_3$)	Crystal phase	The composition of the glass phase (mass. %)							
			SiO_2	Al_2O_3+ TiO_2	Fe_2O_3	CaO	ZnO	BaO	Na_2O	K_2O
SNC	69.2	30.8	37.33	4.44	2.92	0.52	17.20	37.0	0.13	0.26
SK-1	71.6	28.4	39.46	3.49	2.68	-	-	54.26	-	0.11

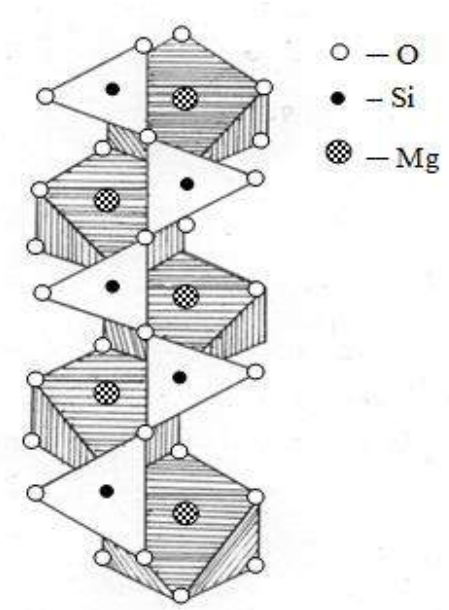

Fig. 1. Fragments of the structure of the crystal phase of the steatite ceramics of the SNC (the relationship between the metasilicate chain and the corresponding chain of cationic octahedra).

.

The DR spectra of ceramics were measured in the wavelength range of 200÷700 nm using a setup whose block diagram is shown in Fig.2. The degree of light reflection was evaluated by the reflection coefficient:

$$R = (I_{irr}/I_{unirr}) \cdot 100\%,$$

where I_{irr} and I_{unir} – intensities of the reflected light from irradiated and unirradiated samples, correspondingly.

Unirradiated samples were used as references (with the same reflectance ~R as the research samples).

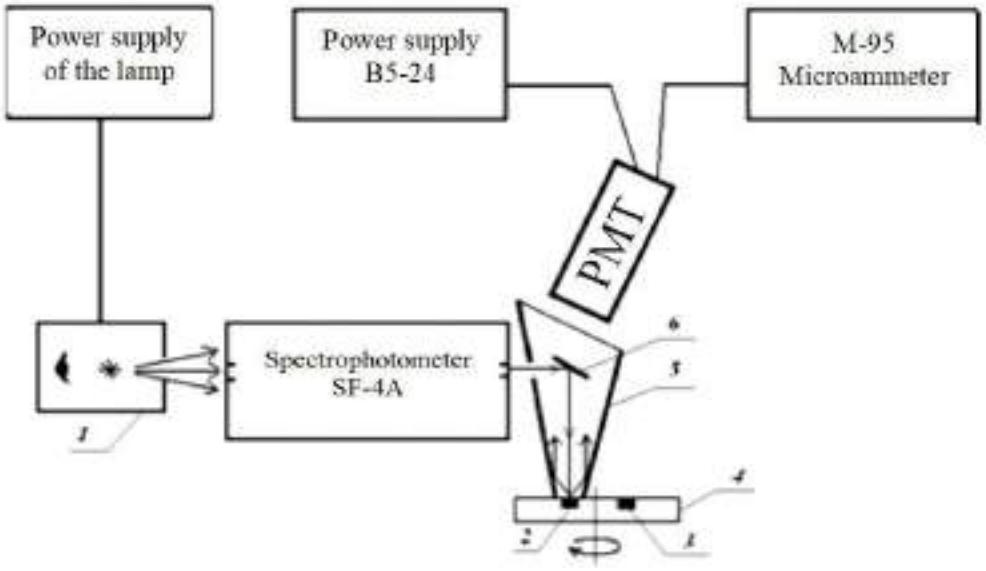

Fig.2. Scheme-of the setup for measuring DR spectra:
1-light source; 2-sample; 3-standard; 4-turn disc; 5-conical mirror; 6-swivel mirror.

When measuring DR spectra, the wavelength resolution of the SF-4A spectrophotometer was 0.1÷0.5 nm, and the error in determining the diffuse reflection coefficient was (R%) 3÷5%. The results obtained were averaged over three samples. When the absorption spectra were decomposed into Gaussians, the error was about 5%.

2. Results and discussion

The studied samples had a white color, and after γ-irradiation, they acquired a brown color, the color density increased with an increase in the dose of γ-irradiation. After γ-irradiation, the DR spectra show additional absorption bands (APB) in the UV region with maxima at λ=220 and 260 nm and a broad absorption band (AB) extending up to 700 nm with maxima at 400÷500. Intensities above the indicated AB increased with increasing dose of γ-irradiation (see Fig. 3, curves 1-3). It should be noted that this type of ceramics has not previously been studied by this method, with the exception of steatite ceramics SK-1 and high-alumina ceramics GB-7, UF-46. Therefore, to identify the detected absorption bands in the diffuse reflection (DR) spectra, we analyzed the literature data on silicates, silicate compounds and glasses, since the basis of this ceramics is the crystalline phase magnesium metasilicate-$MgSiO_3$ and silicate glass of complex composition (see tab.1). Literature data showed that color centers (CC), absorbing light in the region at λ=220 and 260 nm, were observed in quartz, quartz and silicate glasses when irradiated with ionizing radiation [6, 7].

They are associated with defects in the silicon-oxygen framework-SiO_2. Since, in quartz glass and quartz, in the region of λ=215 nm the absorption is due to E^1 -center, which is caused by a three-coordinated silicon atom that captured an electron ($\equiv Si^{3+}$) and EPR signals with g=2.00, characteristic of E^1 -centers of various modifications. In the region of λ=260nm, the absorption is due to a non-bridging oxygen hole center

(NBOHC). It is known that in various types of silicates under γ-irradiation, EPR signals with g = 2.00 were observed, which are characteristic of E^1- centers of various modifications. It should be noted that in all studied silicates, including quartz and silicate glasses, it is associated with the AB at λ=215÷230 nm and the paramagnetic absorption signal with g=2.00. In our case, there are ABs at λ=220 nm and a paramagnetic absorption signal with g=2.0012, which we discovered in [8]. It can be assumed that the AB at λ=220 nm and the paramagnetic absorption signal with g=2.0012 is also associated with the same radiation defect, namely, with the E^1- center.

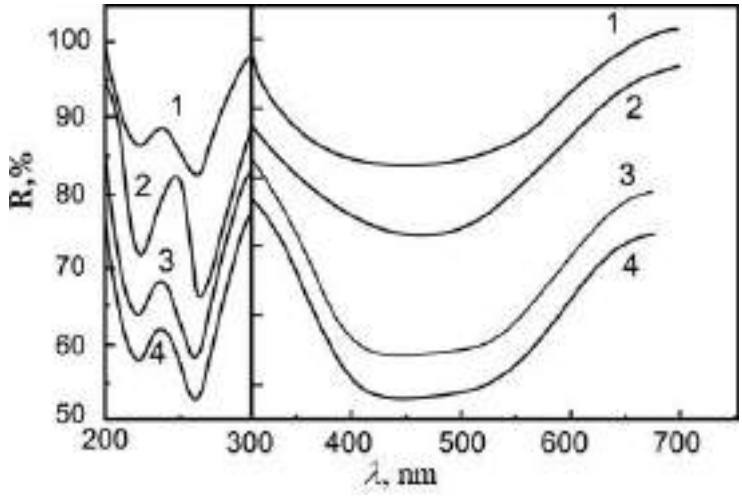

Fig.3. DR spectra of irradiated samples of SNC ceramics:
1-2×10^6 R(1.76×10^6 Rad); 2-10^9 R(8.8×10^8 Rad);3-1.5×10^{10} R(1.32×10^{10}Rad); 4-10^{19} n/cm^2.

It is worth mentioning that in the above-mentioned work [8] in the samples under study in the initial state, one more signal of paramagnetic absorption with g = 4.3 was found in the low-field part of the spectrum. The color center that absorbs light at λ=260nm could be NBOHC. Such a center is observed only in the absorption spectra (AS) of irradiated quartz glass or quartz after n^o-γ irradiation [6,7]. A characteristic feature of NBOHC is the AB with maxima at λ=260 (4.75 eV), 620 (2 eV) nm and luminescence in the region at 660 nm (1.9 eV), which is observed both in the GL spectra and in the PL spectra (λ_{ex}= 260nm).

When excited in the λ=260 nm (4.75 eV) band of non-primary and irradiated ceramic samples, we did not detect luminescence in the region of 660 nm (1.9 eV), which is typical for NBOHC. It follows from here that the observed AB at λ=260nm (4.75 eV) is not related to NBOHC. The following can be suggested about the nature of the AB with a maximum at λ=260 nm (4.75 eV): when analyzing the AS of oxides and silicate compounds with impurities of elements of the iron group, it was shown that in most compounds, for example, in MgO, Al_2O_3 and SiO_2 in the UV region AB can be caused by iron ions.

An analysis of the literature data showed that it is due to Fe^{3+} ions in tetrahedral coordination [6,7]. In silicates and oxides, iron ions can appear in the EPR spectra (electron paramagnetic resonance) both before and after irradiation with ionizing radiation. It is known that, depending on the synthesis conditions, iron ions can be present both in the form of Fe^{2+} and Fe^{3+}. The Fe^{2+} ion has the $3d^6$ electronic configuration, while the Fe^{3+} ion has the $3d^5$ electronic configuration. The iron ion in the Fe^{2+} state does not give a paramagnetic absorption signal at temperatures above 77K [9,10], the Fe^{3+} ion has two paramagnetic absorption signals: with g_1=4.3, corresponding to iron ions in tetrahedral coordination, and a wide anisotropic EPR signal with g_2=2.0026 corresponding to octahedral coordination. The second signal corresponding to octahedral coordination was not revealed by us. This gives grounds to assume that the AB observed in the samples with a maximum at λ==260 nm, which occurs after γ-irradiation, is due to iron ions Fe^{3+} [9,10]. As mentioned above, after γ-irradiation in the visible region of the spectrum, a wide AB is observed with maxima at 400÷550 nm. Literature data on oxide and silicate compounds with ions of the iron group showed that they are associated with hole color centers (CC), which are due to the localization of holes on oxygen ions adjacent to cationic vacancies. In the presence of impurity ions of alkali, alkaline earth metals, or OH groups near the cation vacancy, the characteristics of such centers may change somewhat [11]. Hole-type color centers of various modifications (V-type centers) have wide AB in the visible region of the spectrum;

.

therefore, it can be assumed that the APB observed after γ-irradiation in the visible region can be due to V-type hole centers, which were also observed for SK-1 ceramics [12].

It is known that the specifics of the impact of reactor n°-γ-irradiation differs from γ-irradiation by the formation of many structural defects in their complexes, the displacement of atoms from the site of crystal lattices during elastic and inelastic interactions, etc. After n°-γ-irradiation of the reactor, similar ABs appear in the DR spectra, which were observed in γ-irradiated samples, but the intensity of the bands was higher compared to γ-irradiated samples (see Fig. 3, curve 4). The nature of the AB observed in the UV region of the spectrum with maxima at λ=220 and 260 nm has been discussed above. The study of difference DR spectra ($\Delta R=R_{\gamma}-R_{n\text{-}\gamma}$) of γ- and n°-γ-irradiated samples showed that the spectrum is almost similar to the DR spectrum of ceramics SK-1 [12]. In the DR spectrum of n°-γ-irradiated samples, in contrast to the spectra of γ-irradiated samples, apart from the indicated AB, there are other ones. For example, a new AB appears in the UV region with a maximum of 248 nm. In γ-irradiated samples, this AB is not observed. In the visible region of the spectrum, ABs are observed with maxima at 400 and 450 nm, as well as a wide AB extending from 500 to 700 nm (Fig.3. curve4). An analysis of the literature has shown that AB with a maximum of 248 nm is observed in many silicates and quartz glasses. It is caused by an oxygen vacancy (≡Si–□–Si≡). The formation of ≡Si–□–Si≡ can be due to the approaching of two E^1-centers $\equiv Si^{3+}$ (switching the bond of two $\equiv Si^{3+}$) or direct kicking out of oxygen atoms during neutron irradiation. It can be seen from the figure (Fig. 3, curve 1) that both in the visible and near IR region of the spectrum, the picture is different. There are no obvious ABs here, except for the AB at 400 nm. However, in this region, one can see an overlap (superposition) of several ABs. Such color centers (CCs) are observed in many oxide compounds and complex oxide compounds as well. These can be -O-Me centers or a hole trapped by oxygen ions by an adjacent cationic vacancy. Hole-type color centers of various modifications (V-type centers) have wide ABs in the visible region of the spectrum; therefore, it can be assumed that the AB observed after γ-irradiation in the visible region can be due to V-type hole centers, which were also observed in SK-1 ceramics [12].

Probably, during γ-irradiation, the ≡Si-O-Mg bond is broken with the formation of $\equiv Si^{3+}$;$^{-}$O–Mg, that is, E^1-centers and hole V-centers are formed. The absorption bands of hole V centers are observed in the range from 400 to 700 nm. In particular, they can be V^{2-} (O- ion near the cationic vacancy), V^{-} (cationic vacancy with one trapped hole), V^{O} (cationic vacancy with two trapped holes). In the presence of impurities in oxides, the nature of hole centers also changes [11]. All of these centers, except for E^1-centers, are essentially hole centers, which include the O^{-} ion located in a different environment. In order to separate each AB from the superposition, we decomposed the spectrum in the visible region into Gaussians. After decomposition, the spectrum turned out to be very similar to the decomposition spectrum for steatite ceramics SK-1 [12]. Considering the above mentioned, we also used the data for SNC ceramics. After decomposition into Gaussians, the identification of these centers showed that they consist of four types of V-centers with maxima at 389, 462, 542, and 618 nm (Fig. 4, curve. 2).

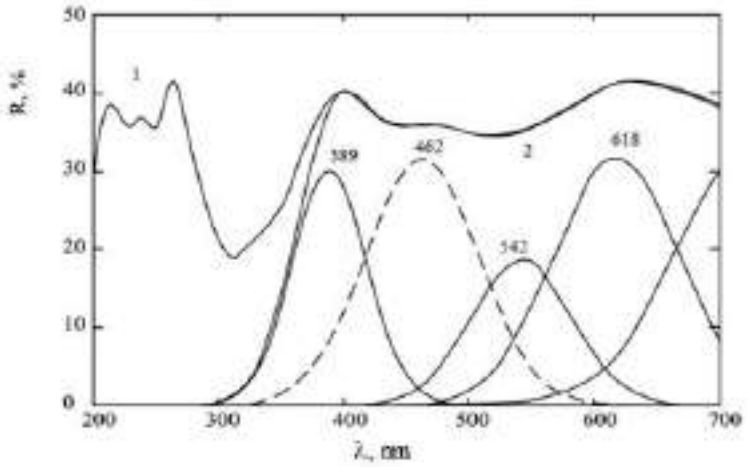

Fig.4. Difference diffuse reflectance spectra of γ- and n°-γ-irradiated SNC ceramics:
($\Delta R=R_{\gamma}-R_{n\text{-}\gamma}$) (curve1) and their decomposition into Gaussians in the visible region of the spectrum (curve2)

The AB with a maximum at 618 nm is characteristic of NBOHC, which is an elementary intrinsic defect in silicate and quartz glasses. This band also appears in γ-irradiated images, but even at high doses ($\geq 10^9$P($8{,}8\times10^8$Rad) its intensity is very weak. The creation of NBOHC may be due to the breaking of the ≡Si-O-Me bond with the removal of Me and the formation of the ≡Si-O^- state. The efficiency of V-center formation in γ-irradiated images was very high compared to NBOHC. The AB with a maximum at 389 nm is associated with -O–Mg, (cationic vacancy in MgO) [11]. Due to the presence of crystalline ($MgSiO_3$) and glassy phases in the steatite ceramics of the SNC, and, consequently, the complex chemical composition [6,7], direct identification of the other two AB centers with maxima at 462 and 542 nm was difficult. However, probably, these ABs are also due to V-type hole centers and are associated with –O–Me states. It is worth mentioning that the difference between the two ceramics lies in the composition of the glass phases, i.e., the presence of oxides such as ZnO (17.20%), CaO (0.52%) and Na_2O (0.13%) in the composition of the SNC glass phase. On the one hand, they are optically inactive elements, especially ZnO, CaO [13], their contribution to the DR spectra is not noticeable, Na_2O may favor the formation of NBOHC, but on the other hand, we do not exclude the contribution of these elements to the formation of (non-radiatively) hole centers in the form of -O–Me (Me-metal, cation) in the visible region of the spectrum, which overlap against the background of intense AB lines, although after decomposing the total spectrum into Gaussians, it is impossible to distinguish them.

Conclusion

Thus, the effect of ionizing radiation on the reflective properties of the SNC steatite ceramics showed that, in contrast to γ-irradiation, the mixed n-γ-irradiation of the reactor additionally creates structural defects. These structural defects are of the type: oxygen vacancies ≡Si–□–Si≡, non-bridging oxygen hole center (NBOHC) ≡Si-O^-. An analysis of the decomposition of the DR spectra into Gaussians in the visible region of the spectrum showed that in the visible region of the spectrum, various hole centers of the type: - -O–Me (Me-metal, cation) are formed.

REFERENCES

1 Gasanov E.M., Chan K.G., Saidakhmedov K.Kh. Action of a high dose of γ-rays on steatite ceramic. *Atomic Energy*, 1996, Vol. 80, No. 2, pp. 127–130.

2 Ashurov M.Kh., Nuritdinov I., Saidakhmedov K.H. Radiative defect formation in steatite ceramics. *Doklady AN RUz,* 2021, No.3, pp.10-14. [in Russian]

3 Belov N.V. *Essays on structural mineralogy*. Moscow, Nedra. 1976, 344 p. [in Russian]

4 Avetikov V.G., Zinko E.I. *Magnesia electroceramics*. Moscow, Energiya, 1973, pp.77 – 79. [in Russian]

5 Myagkova E.S., Tlekhusezh M.A. Reagent and radiation resistance of ceramics. *Nauchnoe obozreniye. Pedagogical Sciences*, 2019, No. 4, pp.77 – 79. [in Russian]

6 Brekhovskikh S.M., Tyulkin V.A. *Radiation-induced centers in inorganic glasses*. Moscow, Ehnergoatomizdat, 1988, 200 p. [in Russian]

7 Silin A. R., Trukhin A. N. *Point defects and elementary excitations in crystalline and vitreous SiO_2.* Riga, Zinatne, 1985, 242 p.[in Russian]

8 Saidakhmedov K Kh., Nuritdinov I. Investigation of Radiation Defects in Steatite Ceramics SK-1 and SNC by the EPR Method. *Proceeding of the XIV Intern. Conf. «Solid state physics, functional materials and new technologies»,* Bishkek. 2018, pp.144 – 146.

9 Tanaka K., Kamiya K., Matsnoka M., et al. ESR-study afolf-gel-derived amorphous Fe_2O_3-SiO_2 system. *J.Non.Cryst.Sol.,* 1987, Vol.94, No. 3, pp.365–373. doi:10.1016/s0022-3093(87)80071-6

10 Bilan O.N., Voropay E.S., Gorbachev S.M., Solovyeva N.D. Luminescence of radiation-oxidized iron in silicate and quartz glasses. *Journal of applied spectroscopy,* 1989, 51 (4), p.244-248. [in Russian]

11 Mironova N.A., Ulmanis U.A. *Radiation Defects and Metal Ions of the Iron Group in Oxides*. Riga. Zinatne. 1988, 202 p. [in Russian]

12 Ashurov M. Kh., Amonov M.Z., Nuritdinov I., Saidakhmedov K.Kh. Diffuse reflection spectra of irradiation SK-1. *Atomic energy,* 2012, Vol. 111, No.4, pp. 301–304.

13 Boksha O.N., Grum-Grkimaylo S.V. *Investigation of the optical spectra of crystals with ions of the iron group at room and low temperatures*. Moscow, Nauka, 1972, 99 p. [in Russian]

Article accepted for publication 13.09.2022

.

DOI 10.31489/2022No4/28-33

UDC 620.22; 53.097

EFFECT OF ANODIZING VOLTAGE ON THE PHOTOCATALYTIC ACTIVITY OF FILMS FORMED BY TITANIUM DIOXIDE NANOTUBES

Serikov T.M., Baltabekov A.S., Aidarova D.D., Zhanbirbayeva P.A., Kuanyshbekova A.B.

E.A. Buketov, Karaganda University, Karaganda, Kazakhstan, serikov-timur@mail.ru

The influence of the anodizing voltage during synthesis on the specific surface area and on the photocatalytic activity of the TiO_2 nanotube was studied. Films formed by titanium dioxide nanotubes were obtained on the surface of titanium foil by electrochemical anodizing. It has been found that an increase in the anodizing voltage from 20 V to 60 V leads to an increase in the inner and outer diameters of nanotubes, an increase in the growth rate and the interpore distance of nanotubes. The photocatalytic activity of the samples was evaluated by measuring the magnitude of the photoinduced current. The film produced at low voltage generated a current 3.5 times higher than the film produced at high voltage, and the degradation of the dye in the presence of the films was 75 and 38%, respectively, over the same period of time. An increase in the photocatalytic activity of the films is mainly associated with an increase in the specific surface area of the nanotubes. Thus, the values of the specific surface area of TiO_2 nanotubes were determined by the method of low-temperature nitrogen adsorption. It has been established that with an increase in the anodizing voltage, the specific surface area of the films decreases.

Keywords: nanotube, titanium dioxide, photocatalysis, specific surface area, splitting of water.

Introduction

Titanium dioxide – TiO_2 nanostructures, due to their semiconductor properties, low toxicity, chemical stability and low cost, are one of the promising photocatalysts for water purification from various pollutants and photocatalytic splitting of water for hydrogen production [1, 2]. However, it has a number of disadvantages, this is mainly due to the rapid recombination of photogenerated electron-hole pairs, a fast reverse reaction occurs in the production of hydrogen, the limitation of the use of visible light (the band gap of TiO_2 is about 2.9–3.2 eV), respectively, only UV-light [3]. The use of one-dimensional TiO_2 nanostructures in the form of nanotubes (NTs) makes it possible to carry out one-dimensional electron transport, which leads to a decrease in the electron free path time from charge generation centers to the anode. In addition, the use of films in the form of an array of NTs will significantly reduce the number of surface defects, which are an obstacle to electron transport, thereby suppressing its recombination [4].

Among the variety of methods for synthesizing NT TiO_2, electrochemical anodizing of metallic titanium is the most promising, since it allows one to control the geometric characteristics of NT by changing the temperature, electrolyte composition, anodizing voltage, and synthesis time [5]. This means that by controlling the geometric characteristics of the NT, one can control the specific surface area of the photocatalyst, since it is proportional to the dispersity or, which is the same, inversely proportional to the size of the nanostructures. The high specific surface of the photocatalyst makes it possible to increase its activity by increasing the amount of adsorbed decomposable substance. For example, the most common and accessible photocatalyst in the form of nanoparticles is Degussa P25, whose specific surface area is about 50 m2/g, and its increase leads to a significant acceleration of the photocatalytic process [6]. A sufficient number of works have been published devoted to increasing the specific surface area of TiO2 NT by various surface modifications [7–13]. However, in the works, NTs were synthesized mainly at one voltage of electrochemical anodization, which were then subjected to modification of the NT surface, and there are practically no works on the study of the photocatalytic activity of NTs with a change in the anodizing voltage. Previously, we have demonstrated how anodizing voltage affects the specific surface area and efficiency of dye-sensitized solar cells based on NTs TiO_2. [14].

In this regard, the present work is devoted to the study of the effect of anodizing voltage during synthesis on the specific surface area and photocatalytic activity of NTs TiO_2.

1. Experimental technique

NTs TiO_2 were obtained by 2-stage electrochemical anodization of titanium foil (VT1–0, 99.7%, Russia) at a temperature of 5–70 C and anodizing voltage varied from 20 to 60 V. The thickness of the foil was 60 μm. The electrolyte used was $C_2H_6O_2$ containing 0.3 wt% NH_4F and 3 wt% H_2O. A Pt electrode served as the cathode. During the anodizing process, the solution was intensively mixed with a magnetic stirrer. The film of LT TiO_2 and by-products of hydrolysis, obtained after the first stage for 2 hours, was removed from the surface of the foil in an ultrasonic bath in HCl solution. The second stage of anodization was 24 hours. After the second anodizing, the obtained NTs TiO_2 was treated with ultrasound to remove by-products, washed with a large amount of distilled water and dried at room temperature. The crystallization of TiO_2 was carried out by heat treatment in a muffle furnace at a temperature of 5000C for 2 hours.

The determination of the phase composition of the samples was carried out using X-ray diffraction patterns obtained on an instrument using an automatic powder diffractometer STOE STADI-P (STOE & Cie GmbH), CuKα radiation, λ=1.54056Å. X-ray patterns were analyzed using the PDF-2 powder database and the standard WinXPow software package. The images of the surface and transverse cleavages of the samples were obtained on a MIRA 3LMU (Tescan) scanning electron microscope. Spectrophotometric measurements were carried out on a Solar SM 2203 spectrophotometer (Solar). The specific surface area of the samples was estimated from low temperature nitrogen adsorption on a Sorbi MS (Meta, Russian). Thermal training of the samples was carried out at a temperature of 100^0C for 180 minutes in the SorbiPrep pre-treatment block. The photocatalytic activity of the samples was evaluated by measuring the magnitude of the photoinduced current with an illuminated area of 1 cm^2 in a standard three-electrode cell using a CS350 potentiostat/galvanostat with an integrated EIS analyzer (Corrtest Instruments, China). The platinum foil served as the opposite electrode, and the AgCl electrode was used as the reference electrode. The measurements were carried out in an electrolyte of 0.1 M NaOH in a specially made photoelectrochemical cell with a quartz window. In addition, the photoactivity of the films was estimated from the photodegradation of the dye methylene blue (MB). Methylene blue dye is used as a model pollutant. Plates sized 1×2 cm were vertically lowered into a quartz reactor containing 50 ml of methylene blue solution with an initial concentration of 10^{-5} mol/l, and kept for 20 hours. Then the used solution was replaced with a similar solution of methylene blue with a concentration of 10^{-5} mol/l. This procedure makes it possible to exclude errors in measuring the optical density of the dye associated with the adsorption of molecules in its pores. The solution was continuously stirred with a magnetic stirrer. A xenon lamp with a power of 300 W/cm^2 (Newport, USA) was used as a radiation source in all experiments. Figure 3b shows a cell in which photocatalytic splitting of water occurs. The amount of released and identification of hydrogen was carried out using an Agilent gas chromatograph located at the Moscow State University named after M.V. Lomonosov. An electrochemical cell was used with solution separation using a Nafion filter and a quartz window to illuminate the surface of the photocatalyst (Minihua Store). The opposite electrode was a Pt plate. Both sides of the chamber are pre-purged with an argon flow. Then, the test gas was taken from the chamber using a syringe and injected into the chromatograph column.

2. Results and discussions

During electrochemical anodization of titanium foil, a film formed on its surface is formed from densely packed cylindrical NTs TiO_2. The images of the surface of the films separated from the titanium foil are shown in Figure 1. The upper part of the nanotubes is open (Fig. 1a). Closer to the bottom of the NT, the inner channel narrows up to complete closure (Fig. 1b). Each NT is fixed to each other by roots, which are clearly shown in Figure 1c, d. With an increase in the applied voltage during electrochemical anodizing between the titanium foil and the opposite electrode, the inner and outer diameters increased, while the wall thickness practically did not change and amounted to about 10–15 nm. According to the results of microscopic examination on the SEM, Table 1 was compiled, which shows the length, outer diameter, the number of NTs per unit surface and the specific surface area with the duration of the second stage of anodizing for 24 hours. It can be seen from the presented data that an increase in the anodizing voltage leads not only to a change in the outer diameter, but also to an increase in the growth rate of the NT. At an anodizing voltage of 20 V, the total length of the NT was 17.1 μm, and at a voltage of 60 V, 37 μm. On the basis of the SEM image, the number of NTs per 1 cm^2 was calculated.

.

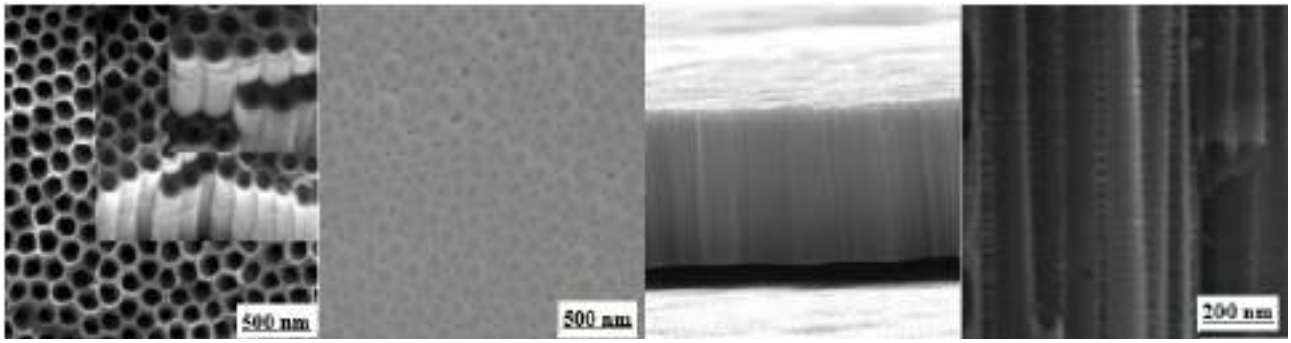

a) b) c) d)

Fig.1. SEM image of NTs TiO_2 separated from titanium foil

As can be seen from the tabular data, at a low voltage (20 V), the amount of NTs per unit area of the film was higher compared to the films obtained at high voltages. This circumstance leads to a change in the specific surface area of the films. Thus, for a film obtained at an anodizing voltage of 20 V, the value of the specific surface area is 72.4 ± 0.1 m^2/g, and for a film of 60 V it is 57.10 ± 0.4 m^2/g. The remaining samples are intermediate values.

Table 1. Characteristics of films formed by NTs TiO_2 obtained at different anodizing voltages

Anodizing voltage, B	L, μm	D_{cp}, nm	Number of nanotubes, 10^9pcs/cm^2	Specific surface area of nanotubes (BET), m^2/g
20	17.1	55	32.2	72.40±0.1
30	22.0	70	21.4	66.78±0.2
40	27.0	90	11.2	64.50±0.6
50	36.0	110	6.7	60.65±0.3
60	37.0	140	2.7	57.10±0.4

Figure 2 shows an X-ray diffraction pattern of a NTs TiO_2 film obtained at an anodizing voltage of 50 V. It was found that the anodizing voltage does not affect the phase. Diffraction peaks (101), (004), (200), (105), (211), (204), (116), (220), and (215) for NTs TiO_2 films correspond to the anatase tetragonal phase (JCPDS, no. 84–1286, a = b = 0.1949 nm and c = 0.1980 nm).

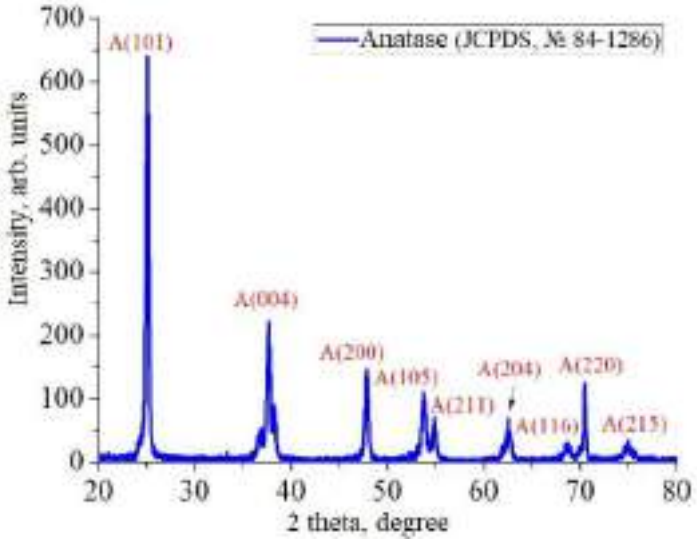

Fig.2. X-ray pattern of NTs TiO_2 obtained at a voltage of 50 V.

The photocatalytic activity of NTs TiO_2 was estimated from the response of the photocurrent when the surface was illuminated by a 1 cm^2 xenon lamp source with a 20-s intermittent on-off switch. Figure 3a shows the change in the photocurrent of all samples. The films exhibit sufficiently good stability. The photocurrent is zero in the absence of light and increases instantly when it is turned on. With an increase in the anodization voltage, the photocurrent density generated by the samples decreased. Thus, a film obtained at an anodization voltage of 20 V generates a high value of photocurrent in comparison with other samples and is about 112 μA/cm^2, while a film synthesized at an anodization voltage of 60 V generates 33 μA/cm^2.

The photocatalytic activity of NTs TiO_2 was also evaluated by the photodegradation of the methylene blue dye (MB). This dye is a model and serves as an example of any contaminant. The photodecomposition of the dye was determined at the wavelength of the maximum absorption of the dye, 662 nm. Irradiation with light leads to the generation of electron-hole (e^- – h^+) pairs in NTs TiO_2 due to photon absorption. Photogenerated electrons in the conduction band of TiO_2 interact with oxygen molecules adsorbed on TiO_2, during which superoxide radicals (O_2^-) are formed. In this case, holes in the TiO_2 valence band react with water molecules and contribute to the formation of hydroxyl radicals (OH^-). Highly reactive hydroxyl radicals (OH^-) and superoxide radicals (O_2) react with the dye molecule adsorbed on TiO_2 nanostructures and lead to its degradation. In the presence of NTs TiO_2 films in an aqueous solution of the dye, a much stronger decrease in the optical density of the dye is observed, which indicates that the molecules in the solution gradually decompose under the action of the light rays of a xenon lamp (Fig. 3b).

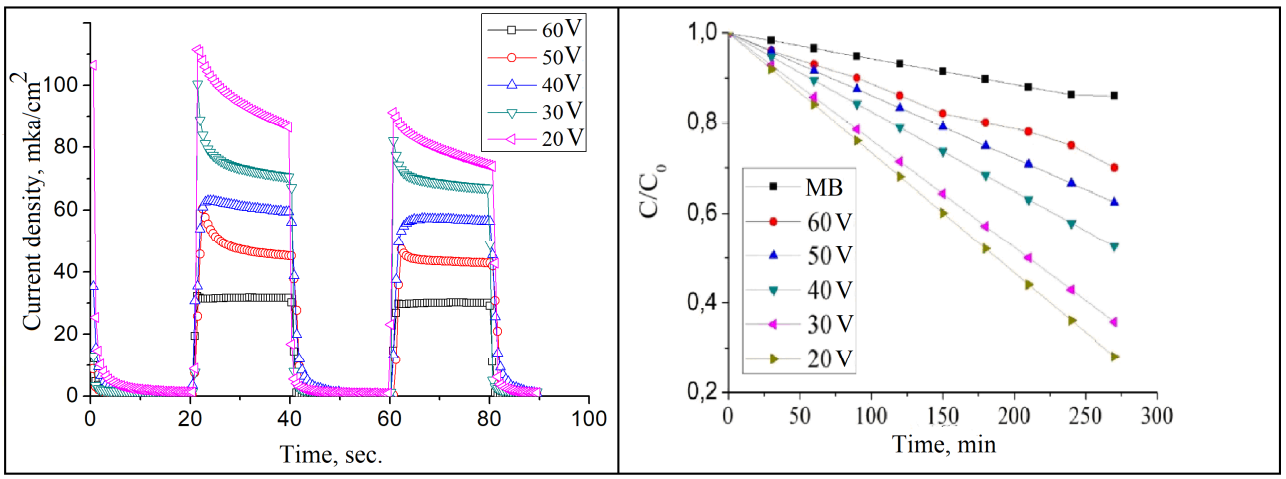

a) b)

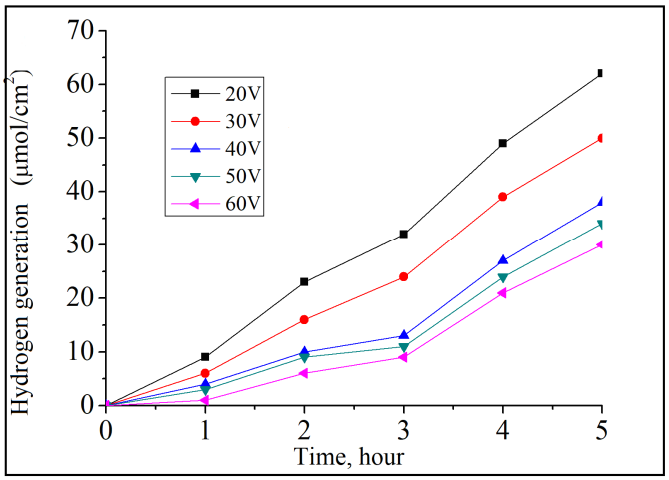

c)

Fig.3. Photocurrent (a), MB dye photodegradation curves (b) and hydrogen generation (c) for films formed by TiO_2 NTs obtained at different anodizing voltages

When the films formed by NTs TiO_2 were lowered into the solution, the optical density of the MB dye decreased, and over the same time interval, the changes were different for the films obtained at different voltages. The largest decrease is observed for the 20 V film, the smallest for the film obtained at 60 V. It can be assumed that the contribution to the photodegradation rate of the MB dye is mainly made by the value of the active surface area, since it is the highest for the film obtained at the anodizing voltage. The larger the area of the semiconductor/dye interface, the faster degradation will occur. Figure 3b shows the photodegradation curves of the MB dye. Before determining the degree of dye degradation, all samples of NTs TiO_2 films were kept in an aqueous solution of the dye for about 2 hours to eliminate the error associated with the adsorption of the dye on its surface. With the duration of irradiation of the dye solution without a photocatalyst, the degradation of the dye is insignificant and amounts to only 9% for 4.5 hours of irradiation. When the films formed by NTs TiO_2 were immersed in the dye solution, the rate of dye degradation increased significantly. Thus, in the presence of a film obtained at an anodizing voltage of 60 V for 4.5 hours of irradiation, the degradation of the dye was 30%, and for a film of 20 V for a similar time interval 91%. In the work of H. Li, et al. “Preparation of TiO2 nanotube arrays with efficient photocatalytic performance and super-hydrophilic properties utilizing anodized voltage method”, a similar research method was used, and it was found that at an oxidation voltage of 30 V, the photodegradation efficiency reaches 65% in six hours , and at 50 V for a similar time period it reaches 98%. At an oxidation voltage of 60 V, the photodegradation efficiency tends to decrease. The reason is that the efficiency of photodegradation is closely related to the wall thickness and diameter of TiO_2 nanotubes [15]. The data obtained indicate that the photocatalytic activity of the film obtained at a voltage of 20 V is higher compared to other samples.

The photocatalytic process of splitting water into hydrogen and oxygen with the participation of a photocatalyst and illuminating its surface with an electromagnetic wave resembles the method of artificial photosynthesis. First, the photocatalyst, absorbing a quantum of light, generates electron-hole pairs, that is, electrons pass from the valence band to the conduction band, while holes remain in the valence band. Further, charge separation and migration of photogenerated electron-hole pairs occur if there is no recombination. Further, the electrons participate in the reduction reaction and generate hydrogen, and the holes participate in the oxidation reaction with the formation of oxygen. Figure 3c shows the kinetics of hydrogen generation as a function of time. Almost all curves have a linear dependence, which indicates a sufficiently high stability of photocatalysts. From the presented data it can be seen that in 5 hours the film produced at 20V is capable of generating up to 62 μmol/cm^2 of hydrogen gas, while the film produced at 60 V generates 30 μmol/cm^2.

Conclusion

NTs TiO_2 were synthesized by electrochemical anodizing at various voltages on the surface of titanium foil. A change in the anodization voltage leads to a change in the geometric characteristics of NTs, which together affected the value of their specific surface area. Since with an increase in the area of the contact boundary of the semiconductor/dye or water, the faster the photocatalytic processes will get through. In photocurrent generation, dye degradation, and hydrogen generation, the film obtained at an anodizing voltage of 20 V demonstrates the best results. For the film obtained at an anodizing voltage of 20 V, the specific surface area is 71 m^2/g, and for the film obtained at 60 V, it is 61 m^2/g. These results can be useful in creating effective photocatalysts with a high specific surface area. For example, instead of the accepted voltages, when obtaining NTs TiO_2 (40–50 V), use a voltage of 20 V and then modify its surface in various ways.

Acknowledgments

This study was supported by the Ministry of Education and Science of the Republic of Kazakhstan (Project AP08052675).

REFERENCES

1 Wang J., Guo R.T., Bi Z.X., Chen X., et al A review on TiO_2-x-based materials for photocatalytic CO_2 reduction. *Nanoscale,* 2022, Vol. 32, pp. 11512–11528. doi: 10.1039/d2nr02527b

2 Kazuhiko M., Kazunari D. Photocatalytic water splitting: recent progress and future challenges. *Journal of physical chemistry letters,* 2010, Vol. 1, No. 18, pp. 2655–2661. doi: 10.1021/jz1007966

3 Yucheng L, Yalin L, Zhifeng R. Mini review on photocatalysis of titanium dioxide nanoparticles and their solar applications. *Nano energy*, 2013, Vol. 2, pp. 1031–1045. doi: 10.1016/J.NANOEN.2013.04.002

4 Serikov T.M. The effect of electric transport properties of titanium dioxide nanostructures on their photocatalytic activity. *Bulletin of Karaganda University. Physics,* 2020, Vol.99, No.3, pp.13–21. doi: 10.31489/2020Ph3/13-21

5 Ibrayev N.Kh., Serikov T.M., Gladkova V.K. Synthesis and investigation of the geometric characteristics of titanium dioxide nanotubes. *IOP Conf. Series: Materials science and engineering*, 2015, Vol. 81, pp. 1–6. doi: 10.1088/1757-899X/81/1/012121

6 Morozov R.S. *Properties and modification of the surface of microporous spherical TiO_2 and SiO_2-TiO_2 particles obtained by the peroxide method*. Diss. for the Candidate of chem. sciences degree, Chelyabinsk, 2018, 154 p. [in Russian]

7 Ge M.Z., Li Q.S., Cao C.Y., et al. One-dimensional TiO_2 Nanotube photocatalysts for solar water splitting. *Advanced science*, 2017, Vol. 4, No. 1, pp. 1600152. doi: 10.1002/advs.201600152

8 Sofiane S., Bilel M. Effect of specific surface area on photoelectrochemical properties of TiO_2 nanotubes, nanosheets and nanowires coated with TiC thin films. *Journal of photocmemistry and photobiology A-chemisrty*, 2016. Vol. 324, pp. 126–133. doi: 10.1016/j.jphotochem.2016.03.030

9 Valeeva A.A., Dorosheva I.B., Kozlova E.A., et al. Solar photocatalysts based on titanium dioxide nanotubes for hydrogen evolution from aqueous solutions of ethanol. *International Journal of hydrogen energy*, 2021, Vol. 46, No. 32, pp. 16917–16924. doi: 10.1016/j.ijhydene.2020.12.190

10 Yang W.T., Li M.X., Pan K., et al. Surface engineering of mesoporous anatase titanium dioxide nanotubes for rapid spatial charge separation on horizontal-vertical dimensions and efficient solar-driven photocatalytic hydrogen evolution. *Journal of colloid and interface science,* 2021, Vol. 586, pp. 75–83. doi: 10.1016/j.jcis.2020.10.071

11 Li Z., Liu H.M., Yao Z.X., et al. Preparation and characterization of titanium dioxide nanotube array/titanium pH electrode. *Chinese journal of analytical chemistry*, 2018.,Vol. 46, pp. 1961–1967. doi: 10.1016/j.ijleo.2019.163432

12 Rempel A.A., Valeeva A.A., Vokhmintsev A.S., Weinstein I.A. Titanium dioxide nanotubes: synthesis, structure, properties and applications. *Russian chemical reviews,* 2021, Vol. 90, pp. 1397. doi: 10.1070/RCR4991

13 Liang H.C., Li X.Z. Effects of structure of anodic TiO_2 nanotube arrays on photocatalytic activity for the degradation of 2,3-dichlorophenol in aqueous solution. *Journal of hazardous materials*, 2009, Vol. 162, pp. 1415–1422. doi: 10.1016/j.jhazmat.2008.06.033

14 Serikov T.M., Ibrayev N.K., Nuraje N., Savilov S.V., Lunin V.V. Influence of surface properties of the titanium dioxide porous films on the characteristics of solar cells. *Russian Chemical Bulletin*, 2017, Vol. 66, No. 4, pp. 614–621. doi: 10.1007/s11172-017-1781-0

15 Lia H., Wanga G., Niua J., Wanga E., Niub G., Xiea Ch. Preparation of TiO_2 nanotube arrays with efficient photocatalytic performance and super-hydrophilic properties utilizing anodized voltage method. *Results in Physics,* 2019, Vol. 14, No. 102499. doi: 10.1016/j.rinp.2019.102499

Article accepted for publication 05.12.2022

.

DOI 10.31489/2022No4/34-43

UDC 621.4

CARBON FOOTPRINT COMPARATIVE ANALYSIS FOR EXISTING AND PROMISING THERMAL POWER PLANTS

Rogalev N.D., Rogalev A.N., Kindra V.O., Zlyvko O.V., Bryzgunov P.A.*

National Research University "Moscow Power Engineering Institute", Moscow, Russian Federation,
BryzgunovPA@mpei.ru

The power production industry is the main greenhouse gas emitter that makes its contribution to global warming. The greenhouse gas emission takes place in fuel production, transportation, and combustion. A prospective method for emission mitigation is the transition to organic fuel-burning facilities with small emissions by capturing carbon dioxide. Power consumption on the carbon dioxide capture remarkably reduces the efficiency of these facilities, which leads to increasing of fuel consumption and greenhouse gas emission because of the larger fuel production and transportation. Based on the material balance method, taking into account system effect of changes in efficiency and amount of fuel consumed, the paper estimated the carbon footprint over a twenty-year lifecycle for following thermal power plants types: combined cycle and oxy-fuel combustion plants for both natural gas and coal with internal gasification. It is shown that the transition to oxygen-fuel plants can reduce the carbon footprint near 90% for natural gas and near 75% for coal. The study also demonstrates the positive effect of carbon capture and storage system implementation for reducing carbon footprint near 75% for natural gas and near 70% for coal.

Keywords: carbon footprint, thermal power plant, combined cycle facility, oxy-fuel cycle, organic fuel, coal gasification

Introduction

ESG (Environmental, Social, Corporate Governance) [1] is a business direction that provides the business social devotion combined with company contribution into the social development and environmental improvement. Since 2015 the world economy shows a distinct trend to the ESG management supported by the ESG investment of up to 30% [2]. The ESG investments since 2014 show a positive influence upon the investment portfolio profitability. The companies that changed to the ESG management may expect larger investments [2]. The main vector of the ESG management introduction for fuel and energy companies is the transition to environment harmless technology and the reduction of harmful emissions and first of all of greenhouse gas emissions [3]. The main greenhouse gases produced in the power production by fossil fuel combustion are the hydrocarbon combustion products, carbon dioxide [3], nitrogen monoxide, and methane as the under-burning product. In power distribution, the main greenhouse gas is the sulfur hexafluoride [4] that is used as an isolating fluid in transformers and high voltage switches. The total greenhouse influence upon the climate changes is assessed by the carbon footprint that is the total greenhouse emission including its global warming potential (GWP) [5] measured in the CO_2 equivalent tons (CO_{2e}).

Some states especially in the EU already have legal movers for the greenhouse emission mitigation that are introduced in the form of carbon dioxide emission quotas that are a subject of stock trade [6, 7]. By the 2022 beginning, these quotas mean the price is above 100 euro for CO_2 ton. Moreover, the EU states introduce a trans-border carbon tax for the products with high carbon footprint including electricity production, the tax will be in power since 2023. So nowadays for the fuel-energy complex, it is topical to reduce the carbon footprint of their products by the transition to renewable power sources and modernization of the existing traditional facilities. A reliable assessment of the new technology practicability requires an accurate analysis of the carbon dioxide footprint effect including the product life evaluation.

The carbon footprint analysis has to correspond to the international standard «ISO 14067:2018 Greenhouse gases. The carbon footprint of products. Requirements and guidelines for quantification». This standard fixes topics and requirements to the carbon footprint analysis, cadaster order, and reports on the product carbon footprint including the life cycle assessment according to the International Standards for the product life cycle analysis ISO 14040 and ISO 14044.

The ISO 14067:2018 standard makes a base for a few methods for the carbon footprint analysis and the issue of reports and cadaster on the greenhouse gas emission as the following:

- EIB Project Carbon Footprint Methodologies [8],
- IPCC manual for the carbon footprint analysis [9],
- PAS 2050 [10],
- GHG Protocol Product Standard [11].

PAS 2050 and GHG Protocol Product Standard are the only methods that involve the record regulations of all stages of product life. These methods are based on similar principles but have some minor distinctions, not leading to difference in calculation of total carbon footprint more than 5%. GHG Protocol Product Standard is the most usual method used by 90% of the S&P Fortune 500 companies, so this method is the main manual in this investigation.

Among the existing thermal power plant (TPP) types, the most environmentally friendly with the smallest greenhouse emission are the natural gas combines cycle plants (NGCC). These facilities have high efficiency above 60% and the resulting lower fuel consumption than Steam Turbine (ST) and Gas Turbine (GT) facilities [12]. The combined cycle power plant's main fuels are natural gas (in NGCC) or coal with the internal gasification cycle (in IGCC). In the internal gasification combined cycle coal is transformed into the syngas that is supplied to a combustor. This technology is a cleaner coal technology because it does not produce the fine-dispersed dust that is the most harmful product of direct coal combustion.

The Carbon Capture and Storage (CCS) systems are prospective technologies for the mitigation of carbon dioxide emissions. The CCS introduction promises an 89% reduction in CO_2 emission. The accumulated carbon dioxide in the future may be used for an increase in oil production rate in EOR-CO2 technology [13, 14]. An important CCS feature is the possibility to apply this technology both for the newly constructed TPP and the modernization of the existing ones. The CCS shortage is a remarkable TPP net efficiency due to the larger internal power consumption. This may reduce the CO_2 mitigation effect by the larger emission in fuel mining and transportation. The nitrogen oxides NOx has no greenhouse effect but their emission is the most environmentally harmful with a negative influence upon the health of people, animals, and plants. The most effective NOx mitigation technology is a selective catalytic recovery (SCR) [15]. The SCR technology recovers NO_x to N2 and water by the ammonia injection, its maximal efficiency may be 95%, and the net efficiency drop is minor and is below 0.5%

The prospective oxygen-fuel power facilities based on the Allam cycle [16, 17] are the nearest to carbon neutrality. In the Allam cycle facilities, natural gas burns in pure oxygen. The produced by combustion carbon dioxide operates as a working fluid, and then is dried and captured. The Allam cycle is closed which provides small carbon dioxide emissions. Now the carbon dioxide emissions of Allam cycle facilities [18, 19] are evaluated as 1% of the total amount of CO2 produced by combustion. This emission is mostly caused by leakages first of all from the facility rotating parts, compressors, and turbines. The oxygen-fuel facility shortage is its smaller net efficiency than the NGCC one due to the additional power consumption in air split and CCS blocks.

This paper compares existing and prospective gas and coal firing TPP. The facilities are compared on the total carbon footprint in all stages of the power production operation:

- NGCC and IGCC facilities to evaluate the existing TPP carbon footprint,
- NGCC and IGCC with CCS and the NOx mitigation system to evaluate the CCS technology efficiency and the prospects for existing TPP modernization,
- Oxygen-fuel Allam cycle facility to evaluate the prospective low emission TPP carbon footprint.

1. Fuel combustion and CO_2 generation in thermal and electrical power generation

The first TPP type reviewed here is the coal TPP with the coal gasification into syngas (fig.1a) and the CO2 capture. Gasification block 3 transforms coal into syngas. The air split facility (ASF) 1 produces oxygen from atmospheric air and compresses it in the oxygen compressor 2. Steam for the gasification process is taken from the steam turbine 14. Syngas in burned in the combustor 5. Compressor 4 compresses air and sends a part of it to the gas turbine cooling 6. The gas turbine 6 rotates the electric power generator 7. The turbine exhaust gas enters the heat recovery boiler and gives its heat to the steam turbine cycle through the heat exchanger surfaces. Block 21 captures the exit CO_2, the compressor 22 compresses it and sends it to the carbon dioxide storage.

In the steam turbine cycle, pump 19 sends the condenser 16 exit water to the heater 13. Upstream the heater the recirculation pump 20 sends a part of heated water to recirculation. The low-pressure feedwater sequentially passes the low-pressure vaporizer 12, the steam superheater 11, and the steam turbine mixer 14. In the mixer, steam is mixed with high-pressure steam [20].

The high-pressure feedwater is sent to the economizer 10, the high-pressure vaporizer 9, and the steam superheater 8 like in the low-pressure circuit. The high-pressure steam produces electricity in enters the steam turbine 14. The exhaust steam enters the condenser 16.

The second facility version (fig. 1b) is the IGCC without capturing. This version differs from fig. 1a by the absence of the elements 21 and 22. After the heat recovery boiler, the exhaust gas with the carbon dioxide content leaves the atmosphere.

The third version (fig. 1c) describes a coal firing TPP with oxygen fuel combustion. Coal gasification block 3 is supplied with coal, oxygen, and steam. The produced syngas is cooled in cooler 23 for a more efficient compression, then compressed in the fuel compressor 24 and sent to the combustor 5. The syngas is burning in the almost pure oxygen produced in ASU 1. The CO_2 heated flow goes to the multi-flow regenerator 25. Downstream the combustor 5 the working fluid enters the carbon dioxide turbine 26. The turbine 26 exhaust enters the multi-flow heat exchanger 25 where it gives its heat to the CO_2 flow, the turbine heat carrier 29 of CO_2 with O_2. The regenerator 25 exhaust enters the cooler-separator 30 where the working fluid water steam condenses. Then the CO_2 flow splits into two parts. The main part is compressed in compressor 28 and the remaining part is compressed in compressor 22 and stored.

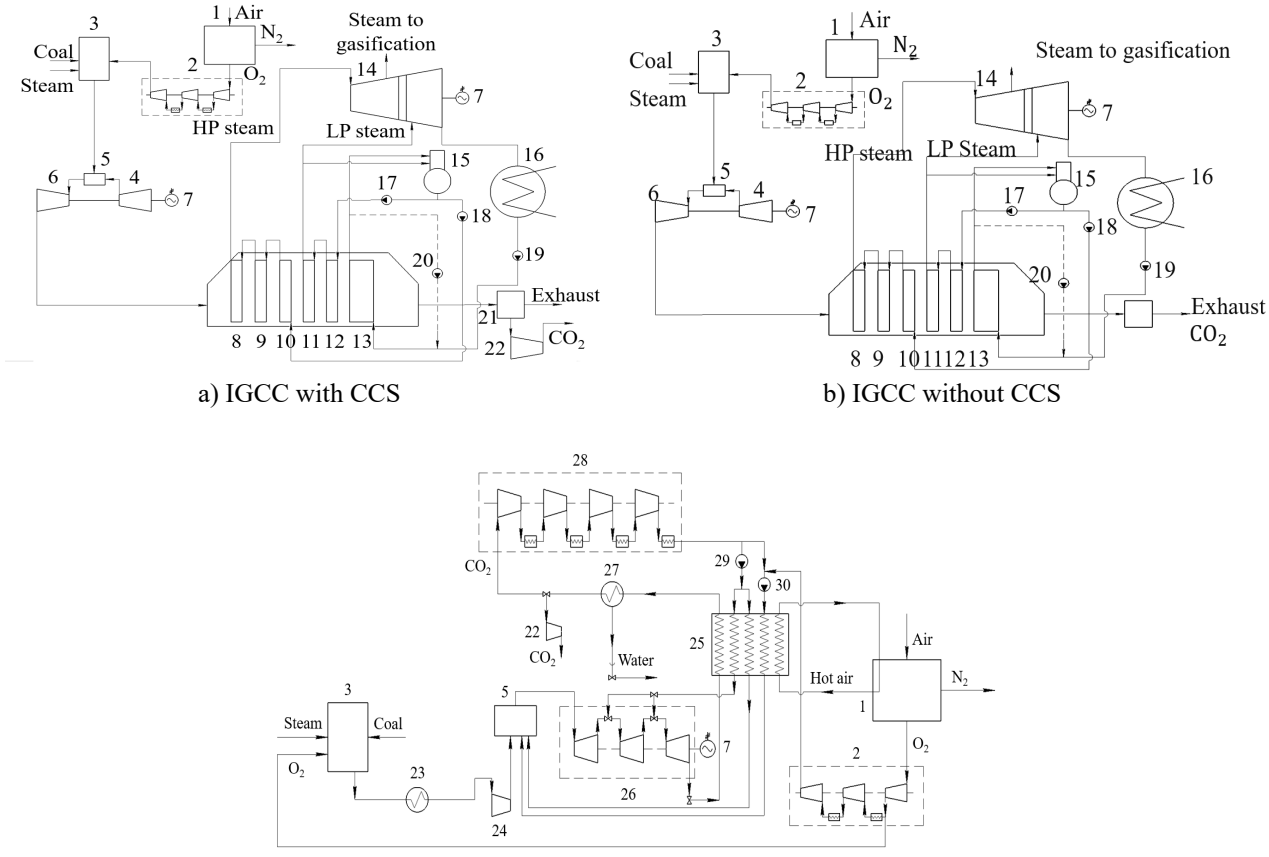

a) IGCC with CCS

b) IGCC without CCS

c) Oxy-fuel power plant with coal gasification

Fig.1. Heat flow charts of coal firing TPP with internal coal gasification

After the multi-stage compressor 28, the CO_2 flow is split into two equal parts. One part is mixed with oxygen. After the CO_2 compressor 29, its exit splits into two parts. The smaller part works as the turbine 26 heat carrier and it is heated in the regenerator 28. The regenerator heats the main CO_2 flow and the oxygen-CO_2 mixture. The oxygen-carbon dioxide compressor 30 compresses the mixture up to the maximal temperature acceptable for the regenerator temperature difference. The hot flows that enter combustor 5 from the regenerator 25 reduce the fuel flow needed for the operating fluid heating up.

The second type of facility reviewed in this paper is the natural gas firing facilities (fig. 2) [19]. The first type is the NGCC facility with CO_2 capture (fig. 2a). This facility differs from the IGCC type; it has no coal gasification elements 1-3. The second type (fig. 2b) is the NGCC without the CO_2 capture (21, 22).

The third type (fig. 2c) is the oxy-fuel natural gas firing facility that differs from the coal firing with coal gasification (fig. 1b) by the absence of coal gasification elements 1 – 3.

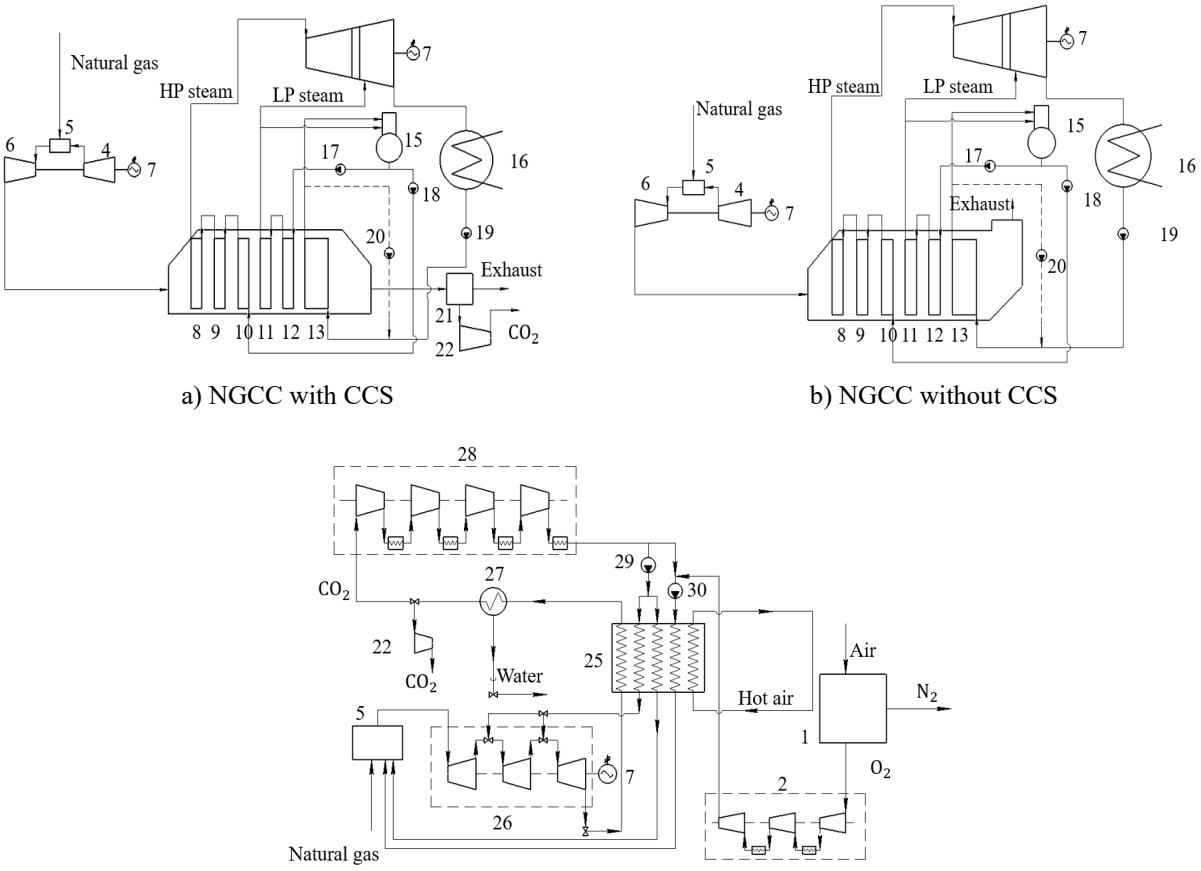

a) NGCC with CCS

b) NGCC without CCS

c) Oxy-fuel power plant

Fig.2. Heat flow charts of natural gas firing TPP

The review of scientific papers and technical reports [21, 22] is devoted to the evaluation of the combined cycle facilities' total carbon footprint. The most significant is the greenhouse gas emission during the facility operation. The mean greenhouse emission during equipment manufacturing, construction, and decommissioning is about 1% of the total emission. The Product Standard [23] method allows not to take into account the life cycle stages that make below 1% of carbon footprint separately and 5% in total. So, the system boundaries are assumed as the following:

- manufacturing and construction stages are not considered;
- the operation stage considered, the carbon footprint analysis includes not only fuel combustion but also fuel mining and shipment;
- the decommissioning and scrap stages are not considered.

2. Initial data

The life cycle carbon footprint analysis input data are given in table 1-3, the considered TPP types are summarized in table 1. Different TPP types are compared at equal net power values. This allows adequate comparison and the relation between the facility efficiency and emissions. The distances from coal or natural gas deposits to TPP are assumed equal to adequately analyze the influence of fuel type upon the TPP carbon footprint at the stages of fuel mining and shipment. Also, in the TPP with internal gasification the assumed fuel is not syngas but coal which is due to the assumed life cycle boundaries.

Table 2 shows the emission data for natural gas and syngas fuels combustion in gas turbine combustors. The emission analysis must take into account the type of fuel-burning equipment. For example, it is known that the natural gas combustion in steam turbine facilities produces lower emissions per kilogram of fuel, than the gas turbine one. Table 3 shows reference initial data for the carbon footprint analysis.

Table 1. TPP parameters

TPP type	Net power, MW	Net efficiency, %	Fuel	Distance from deposit, km	Life, years
NGCC	100	63.50% [20]	Natural gas	3000	20
NGCC with CO_2 and NO_x capture	100	57.10% [20]	Natural gas	3000	20
Oxy-fuel facility	100	46.70% [20]	Natural gas	3000	20
IGCC	100	53.50% [20]	Coal	3000	20
IGCC with CO_2 and NO_x capture	100	46.20% [20]	Coal	3000	20
Oxy-fuel facility	100	36.30% [20]	Coal	3000	20

Table 2. Harmful emissions produced by fuel combustion and Global Warming Potential (GWP)

Fuel	Harmful emission, kg/kg				
	CO_2	CH_4	N_2O	NO_x	SO_2
Natural gas	2.75	4.0E-04	1.39E-04	1.49E-02	7.0E-07
	[22, 24]	[22]	[21, 24]	[25]	[22]
Syngas	2.49	2.67E-04	2.7E-04	1.53E-03	2.14E-03
	[26]	[26]	[26]	[27]	[27]
GWP (AR6) [9]	1	82.5	273	0	0

Table 3. Reference input data for the carbon footprint analysis

Parameter	Value
CO_2 leakage in an oxy-fuel facility, %	1.0 [18]
TPP annual operation, hr/year	6000 [28]
Coal conversion with gasification, %	95 [29]
Natural gas calorific value, MJ/kg	49 [30]
Coal calorific value, MJ/kg	27 [31]
CO_2 capture efficiency in a NGCC and IGCC, %	89 [20]
SCR NO_x precipitation efficiency, %	95 [15]
Natural gas transportation leakages, %	0.036 [32]
Gas-main pipeline power efficiency, kg gas/ (mln. kg · km)	21.83 [32]
Greenhouse gas emission in coal transportation, kg CO_{2e}/(ton·km)	0.04 [33]
Greenhouse gas emission in coal mining, kg CO_{2e}/kg coal	0.3 [34]

3. Methodology

In this research, complex physical-chemical methods were used to estimate carbon footprint by methods according to GHG standard methodology [11], including stages of fuel mining, fuel transporting and power plant operation. In the operation stage considered fuel combustion only as a main process leading to greenhouse gas emissions during plant operating. To estimate carbon footprint of lifecycle stages material balance physical methods were used. To estimate specific emissions during fuel mining, fuel transporting and combustion were used following data:

1. Empirical and analysis estimated data for fuel mining and transporting according literary [18, 30-34];
2. Combination of empirical physical-chemical data and stoichiometric chemical analysis for combustion according to sources [20-30].

Calculations were provided by using MS Excel 2021. To validate model obtained were used initial data and results described in [21, 22].

Different natural gas and coal firing TPP with internal gasification produce the carbon footprint that may be calculated as the following:

$$E_{sum} = E_c + E_t + E_m, \quad (1)$$

where E_{sum} – total greenhouse gas emission following mining, shipment, and combustion during the power production facility operation, ton CO_{2e};

E_c – total greenhouse gas emission following the combustion during the power production facility operation, ton CO_{2e};

E_t – total greenhouse gas emission following the fuel transporting during the power production facility operation, ton CO_{2e};

E_m – total greenhouse gas emission caused by the fuel mining during the power production facility operation, ton CO_{2e}.

For gas and coal firing TPP with internal gasification E_c is calculated as the following:

$$E_c = \frac{M \cdot T \cdot \sum_{i=1}^{n} e_{gi} \cdot GWP_i \cdot (1 - \alpha_c)}{1000}, \quad (2)$$

where M – annual fuel consumption in TPP, kg·year; T – thermal power plant operation life, years;

e_g – specific harmful emission related to the burned fuel, kg/kg; GWP_i – potential global warming caused by the emissions, kg CO2e/kg; α_C – emission precipitation rate, %.

For gas fuel the annual consumption M is calculated by the following equation:

$$M = \frac{N \cdot \tau \cdot 3.6 \cdot 10^6}{\eta \cdot Q_H}, \quad ((3)$$

where N – thermal power plant net power,

For coal firing TPP with internal gasification it is necessary to take into account the gasification process efficiency so the coal annual consumption M MW; τ – estimated TPP annual operation, hr; η – net efficiency, %; Q_H – Fuel heating value kJ/kg.is calculated by the following equation:

$$M = \frac{N \cdot \tau \cdot 3.6 \cdot 10^6}{\eta \cdot \eta_g \cdot Q_H}, \quad (4)$$

where η_g – coal gasification conversion rate, %.

The components E_t and E_m in equation (1) are calculated by different equations for different fuels. Gas transportation in main pipelines is usually provided by gas turbine pumping facilities working on the natural gas fuel, so for the transportation stage, the pump driving carbon footprint is taken into account. Also, an important emission factor is the natural gas leakage through seals and control accessories. Usually, these leakages are as small as below 0.05% but methane has high GWP so this factor also should be involved. Besides this, the greenhouse gas emission in production also should include transportation gas consumption. So the natural gas transportation carbon footprint is calculated by the equations:

$$E_t = E_{ct} + E_{lt}, \quad (5)$$

where E_{ct} – total greenhouse gas emission caused by the fuel transporting, by fuel combustion in gas pumping stations during the power production facility operation, ton CO_{2e};

E_{lt} – total greenhouse gas emission caused by the fuel transporting, by fuel leakages during the power production facility operation, ton CO_{2e}.

$$E_{ct} = \frac{M_t \cdot T \cdot \sum_{i=1}^{n} e_{gi} \cdot GWP_i \cdot (1 - \alpha_c)}{1000}, \quad (6)$$

where M_t – amount of the natural gas consumed in the gas pumping facilities, kg/year.

$$M_t = \frac{M \cdot \omega \cdot l}{(1-\eta_l) \cdot 1000000}, \quad (7)$$

where ω – natural gas specific consumption in gas pumping plants, kg/(mln.kg·km);

l – distance from the fuel mining place to the TPP location, km;

η_l – natural gas leakages in pipelines, %.

$$E_{lt} = \eta_l \frac{(M + M_t) \cdot GWP_{CH4} \cdot T}{(1-\eta_l) \cdot 1000}. \quad (8)$$

The oxy-fuel power facilities operate a closed cycle with pure oxygen oxidation, so the parameter α_c for NO_x, SO_2, CH_4, and N_2O is assumed as 100% because the emission of these gases is minor and nearly zero. For CO_2 this parameter α_c is assumed 99% for the leakages in the moving device seals of 1% (table 4). The natural gas production carbon footprint is calculated with the equation:

$$E_m = \frac{(M+M_t) \cdot T \cdot \gamma_m}{(1-\eta_l) \cdot 1000}, \quad (9)$$

where γ_m – greenhouse gas specific emission caused by the natural gas mining, kg CO_{2e}/kg.

For coal fuel, E_t and E_m are calculated with statistical mean data on greenhouse emission in coal mining and transportation. The following equation is used for the coal mining carbon footprint:

$$E_m = \frac{M \cdot T \cdot \mu_m}{1000}, \quad (10)$$

where μ_m – greenhouse emission in coal mining, kg CO_2e/kg.

The coefficient μ_m reflects emission of the methane content in coal layers, the greenhouse gas emission by the coal mining machine engines, and the energy consumption by coalfield. The coal transportation carbon footprint is calculated by the following equation:

$$E_t = \frac{M \cdot T \cdot \sigma_t \cdot l}{1000000}, \quad (11)$$

where σ_t – greenhouse emission in coal transportation, kg CO_{2e} /(ton·km).

Here σ_t describes the greenhouse emission by the technology transport that moves coal in operation, for electric transport this coefficient corresponds to the mean emission in electricity production and distribution.

4. Results and discussion

Table 4 summarizes analysis results for the carbon footprint of natural gas firing TPP. Comparison analysis shows that among the considered types the oxy-fuel facility has the smallest greenhouse emission. Its carbon footprint is 49% smaller than the NGCC with CO_2 capture and storage system. This difference is due to the oxy-fuel facility closed cycle and the minimal CO_2 operation leakages. It is worth mentioning that the introduction of the CO_2 capture in NGCC reduces the carbon footprint by 4.6 times in spite of its smaller efficiency. This shows the high CCS potential for the existing TPP modernization.

Table 5 shows the contents of the greenhouse gas and harmful agent emissions. The emission analysis shows that 97.48% of NGCC without CCS emission with consideration of GWP is CO_2. The introduction of the CCS reduces the CO_2 contribution down to 80.99%. This shows that the CH_4 and N_2O emission mitigation may be the trend for the carbon footprint reduction in TPP after the TPP modernization with CCS systems.

Table 6 shows results of the carbon footprint calculation for the syngas firing TPP. It is worth mentioning that the internal gasification TPP overcome the natural gas firing TPP for 2 – 5 times in different TPP types. This is mostly due to the smaller coal energy capacity and the lower TPP efficiency.

Comparison of the coal firing facilities with internal gasification carbon footprint shows that the oxy-fuel facility has the smallest greenhouse emissions among the considered TPP types. The oxy-fuel facility's carbon

footprint is 28% smaller than that of the IGCC with CO_2 capture and storage. This is due to the closed cycle of the oxy-fuel facility and minimal CO_2 operational leakage. It is worth mentioning that implementation of the CO_2 capture and storage in an IGCC may 6 times reduce its carbon footprint in spite of the lower efficiency. This shows the high potential of the CCS technology for the TPP with internal gasification.

Table 4. Structure of natural gas firing TPP footprint

TPP type	Carbon footprint, ton CO_{2e}			
	Fuel mining	Fuel transporting	Combustion	Total
NGCC	2 921	297 180	3 915 132	4 215 234
NGCC with CO_2 and NO_x capture	3 248	330 490	576 490	910 228
Oxy-fuel facility	4 138	404 089	51 896	460 123

Table 5. Harmful emission contents by natural gas firing TPP

TPP type	Emission produced in combustion during the operation life, ton					
	CO_2	CH_4	N_2O	NO_x	SO_2	Total, ton CO_{2e}
NGCC	3 816 567	555	193	20635	1	3 915 132
NGCC with CO_2 and NO_x capture	466 878	617	215	1 147	1	576 490
Oxy-fuel facility	51 896	~0	~0	~0	~0	51 896

Table 6. Structure of carbon footprint for the TPP with internal gasification.

TPP type	TPP carbon footprint for 20 years operation, ton $CO_{2\,e}$			
	Fuel mining	Fuel transporting	Combustion	Total
IGCC	964 655	381 545	7 733 119	9 079 318
IGCC with CO_2 and NO_x capture	1 117 078	441 832	1 280 175	2 839 085
Oxy-fuel facility	1 421 736	562 331	109 753	2 093 820

Table 7 presents the greenhouse gas emission structure. In the basic IGCC version, CO_2 makes 96.3% of the carbon footprint with GWP but the CCS technology introduction reduces the CO_2 contribution down to 74.1%. This shows that the CH_4 and N_2O emission mitigation may be a further direction of the facilities' modernization after the CCS system introduction.

Table 7. Contents of harmful emissions from syngas combustion

TPP type	Emissions from fuel combustion for the operation life, ton					
	CO_2	CH_4	N_2O	NO_x	SO_2	Total combustion, ton $CO_{2\,e}$
IGCC	7446 766	799	807	4 577	6 414	7 733 119
IGCC with CO_2 and NO_x capture	948 576	925	935	265	7 428	1 280 175
Oxy-fuel facility	109 753	~ 0	~ 0	~ 0	~ 0	109 753

Conclusions

Comparison of the natural gas and TPP with internal gasification shows that the gas firing TPP has smaller greenhouse gas emissions; the basic IGCC facility produces a 114% higher carbon footprint than the NGCC ones. These differences are due to the low energy capacity of coal, low efficiency of syngas firing facilities, and the high emission of greenhouse gases during coal mining, first of all of CH4. The structure of the TPP

carbon footprint has a large part of coal mining. So, the greenhouse emission by mining has to be included in public reports of coal firing companies.

The oxy-fuel facilities have the smallest carbon footprint of gas firing facilities its total greenhouse emission is 49% smaller than in the NGCC with CO_2 capture which shows the oxy-fuel facility's high effectiveness for greenhouse emission mitigation. The NGCC with a CCS system has a 4.6 times smaller carbon footprint than the basic NGCC facility. This shows the high potential of the CCS system for the modernization of the existing power production facilities.

An analysis of TPP with internal coal gasification shows that the oxy-fuel facility has the smallest greenhouse gas emission of the considered gas firing TPP. Its difference with the CCS equipped IGCC is about 28% which demonstrates the smaller effect of the transition to the oxy-fuel facilities in coal fuel than in gas one. The CCS-equipped IGCC has a 6 times smaller carbon footprint than the basic facility which shows a remarkably larger positive effect of CCS introduction than the power production with gas.

The described effects allow the following recommendations:

- application of the oxy-fuel facilities makes minimal carbon footprint, the oxy-fuel introduction in gas firing facilities has higher priority than in the TPP with internal gasification ones;
- modernization of existing TPP by the CCS introduction has high priorities for both coal and gas firing power production, in the second case, positive influence upon the carbon footprint may be higher. Comparison analysis shows that among the considered types the oxy-fuel facility has the smallest greenhouse emission. Its carbon footprint is 49% smaller than the NGCC with CO_2 capture and storage system. This difference is due to the oxy-fuel facility closed cycle and the minimal CO_2 operation leakages. It is worth mentioning that the introduction of the CO_2 capture in NGCC reduces the carbon footprint by 4.6 times in spite of its smaller efficiency. This shows the high CCS potential for the existing TPP modernization.

Acknowledgments (or Funding)

This study conducted by Moscow Power Engineering Institute was financially supported by the Ministry of Science and Higher Education of the Russian Federation (project No. FSWF-2020-0020).

REFERENCES

1 Nakajima T., et al. *ESG Investment in the Global Economy.* Springer, Singapore, 2021, 107 p.

2 Cesarone F., Martino M.L., Carleo A. Does ESG Impact Really Enhance Portfolio Profitability? *Sustainability,* 2022, Vol. 14, No. 4, pp. 1–28.

3 Peters G. P., et al. Carbon dioxide emissions continue to grow amidst slowly emerging climate policies. *Nat. Clim. Chang.,* 2020, Vol. 10, No. 1, pp. 3–6.

4 Yu X.Y., et al. Evaluation of nitrous oxide as a substitute for sulfur hexafluoride to reduce global warming impacts of ANSI/HPS N13.1 gaseous uniformity testing. *Atmospheric Environment,* 2018, Vol. 176, pp. 40–46.

5 Rosa L. P., Schaeffer R. Global warming potentials. *Energy Policy*, 1995, Vol. 23, No. 2, pp. 149–158.

6 Friedlingstein P., O'Sullivan M., Jones M.W., Andrew R.M., Hauck J., Olsen A., Zaehle S. Global carbon budget 2020. *Earth Syst. Sci. Data*, 2020, Vol. 12, No. 4, pp. 3269–3340.

7 Nemtinova Yu.V., Nemtinov V. A. Managing Greenhouse Gas Emissions Quotas on the Way to Decarbonizing the Economy. *Èkol. prom. Ross.,* 2022, Vol. 26, No. 1, pp. 19–23.

8 *EIB Project Carbon Footprint Methodologies*. European Investment Bank, Luxembourg 2020. Available at: https://www.eib.org/attachments/publications/eib_project_carbon_footprint_methodologies_2022_en.pdf

9 Masson-Delmotte V. et al. *IPCC, 2021: Climate Change 2021: The Physical Science Basis.* Cambridge University Press, Cambridge, Great Britain, 2021, 112 p.

10 *Guide to PAS 2050: how to assess the carbon footprint of goods and services.* BSI, London, 2008, 101 p.

11 *Greenhouse gas protocol: product life cycle accounting and reporting standard.* World Resources Institute, Washington, DC, 2011, 116 p.

12 Zhang T. Methods of Improving the Efficiency of Thermal Power Plants. *J. Phys.: Conf. Ser.*, 2020, Vol. 1449, No. 1, p. 012001.

13 Raza A., Gholami R., Rezaee R., Rasouli V. and Rabiei M. Significant aspects of carbon capture and storage – A review. *Petroleum*, 2019, Vol. 5, No. 4, pp. 335–340.

14 Jia W., McPherson B., Dai Z., Irons T. and Xiao T. Evaluation of pressure management strategies and impact of simplifications for a post-EOR CO2 storage project. *Geomech. Geophys. Geo-energ. Geo-resou*r., 2017, Vol. 3, No. 3, pp. 281–292.

15 Schorr M. M. and Chalfin J. *Gas Turbine NOx Emissions Approaching Zero: Is it Worth the Price?* General Electric Company, Schenectady, USA, 1999, 12 p.

16 Rodríguez Hervás G. and Petrakopoulou F. Exergoeconomic Analysis of the Allam Cycle. *Energy Fuels*, 2019, Vol. 33, No. 8, pp. 7561–7568. . https://doi.org/10.1021/acs.energyfuels.9b01348

17 Rogalev, A., Komarov, I., Kindra, V., Zlyvko, O. Entrepreneurial assessment of sustainable development technologies for power energy sector. *Enterpreneurship and Sustainability Issues*. 2018, Vol. 6(1), pp. 429 – 445. http://doi.org/10.9770/jesi.2018.6.1(26)

18 Rogalev A., Rogalev N., Kindra V., Komarov I., and Zlyvko O. Research and Development of the Oxy-Fuel Combustion Power Cycles with CO_2 Recirculation. *Energies,* 2021, Vol.14, No.10, p.2927. doi: 10.3390/en14102927

19 Rogalev A., Grigoriev E., Kindra V. and Rogalev N. Thermodynamic optimization and equipment development for a high efficient fossil fuel power plant with zero emissions. *Journal of Cleaner Production*, 2019, Vol. 236, p. 117592.

20 Kindra V. O., Milukov I. A., Shevchenko I. V., Shabalova S. I. and Kovalev D. S. Thermodynamic analysis of cycle arrangements of the coal-fired thermal power plants with carbon capture. *Archives of Thermodynamics,* 2021, Vol.42, No. 4, pp. 103–121. doi:10.24425/ather.2021.139653

21 Spath P. L., Mann M. K. *Life Cycle Assessment of a Natural Gas Combined Cycle Power Generation System.* NREL, Denver, USA, 2000. Available at: Life Cycle Assessment of a Natural Gas Combined Cycle Power Generation System (nrel.gov)

22 James III R. E. *Skone T. J., Life Cycle Analysis: Natural Gas Combined Cycle (NGCC) Power Plant.* NETL, Pittsburghm, USA, 2012, 148 p.

23 *Product Life Cycle Accounting and Reporting Standard*. World Resource Institute, Washington DC, USA, 2013. Available at: https://ghgprotocol.org/sites/default/files/standards/Product-Life-Cycle-Accounting-Reporting-Standard_041613.pdf

24 Ferat Toscano C., et al. Life Cycle Assessment of a Combined-Cycle Gas Turbine with a Focus on the Chemicals Used in Water Conditioning. *Sustainability*, 2019, Vol. 11, No. 10, p. 2912. doi:10.3390/su11102912

25 Jung S., et al. Development of Low Emission Gas Turbine Combustors. *Proceedings of ASME Turbo Expo 2015: Turbine Technical Conference and Exposition,* 2015, Vol. 4, p. 01.

26 Steen M. *Greenhouse gas emissions from fossil fuel fired power generation systems.* European Commission, Brussels, 2001, 61 p.

27 Whitty K.J., Zhang H. R. and Eddings E. G. Emissions from Syngas Combustion. *Combustion Science and Technology*, 2008, Vol. 180, No. 6, pp. 1117–1136. doi: 10.1080/00102200801963326

28 Tripathi A.K. Falling capacity utilization of thermal power plants in India: Projection of future scenarios. *International Journal of Energy Production and Management*, 2020, Vol. 6, No. 1, pp. 94-104.

29 Harris D.J., Roberts D.G. *Coal gasification and conversion. The Coal Handbook: Towards Cleaner Production*. Woodhead Publishing, Philadelphia, USA, 2013, 576 p.

30 Liang F.-Y., Ryvak M., Sayeed S., Zhao N. The role of natural gas as a primary fuel in the near future, including comparisons of acquisition, transmission and waste handling costs of as with competitive alternatives. *Chemistry Central Journal,* 2012, Vol. 6, No. 1, pp. 4. doi:10.1186/1752-153X-6-S1-S4

31 Richards A. P., Haycock D., Frandsen J. and Fletcher T. H. A review of coal heating value correlations with application to coal char, tar, and other fuels. *Fuel*, 2021, Vol. 283, pp. 118942. doi: 10.1016/j.fuel.2020.118942

32 Xie Y., Ma X., Ning H., Yuan Z. and Xie T. Energy efficiency evaluation of a natural gas pipeline based on an analytic hierarchy process. *Advances in Mechanical Engineering*, 2017, Vol. 9, No. 7, pp. 1-12.

33 Yin L., Liao Y., Zhou L., Wang Z. and Ma X. Life cycle assessment of coal-fired power plants and sensitivity analysis of CO2 emissions from power generation side. *IOP Conf. Ser. Mater. Sci. Eng.*, 2017, Vol. 199, pp. 012055. doi:10.1177/1687814017711394

34 Miller B. G. *Clean Coal Engineering Technology.* EMS Energy Institute, State College, USA, 2017, 244 p.

Article accepted for publication 04.06.2022

DOI 10.31489/2022No4/44-50

UDC 621.472

TESTING OF DIFFERENT MATERIAL TYPE PHOTOELECTRIC BATTERY AND PHOTOTHERMAL BATTERIES COMPOSED

Tursunov M.N[1]., Sabirov X.[1], Abilfayziyev Sh.N.[2], Yuldoshov B.A.[2]

[1]Physical-Technical Institute of Academy of Sciences of the Republic of Uzbekistan, Tashkent, Uzbekistan
[2]Termez State University, Termez, Uzbekistan, abilfayziyev@inbox.ru

In the world, over the years, the use of hydrocarbon resources is decreasing, and their place is being replaced by ecologically clean alternative and renewable energy sources. Therefore, the world is paying a lot of attention to improved devices based on photoelectric batteries. Conducting targeted scientific research in this direction is one of the urgent issues of the present time. This article presents the results of comparing the electrical parameters of photovoltaic and photothermal batteries based on them in natural conditions. The experiments were carried out on three traditional photoelectric batteries with different materials and constructions, as well as photothermal batteries made on their basis. All batteries are installed in a mobile structure, and two planes (reflectors) that reflect sunlight are installed along the long side of the device connecting the batteries. In the same conditions, the intensity of solar radiation is increased with the help of reflectors that return light to photoelectric and photothermal batteries. On the front surface of the photovoltaic batteries, a vertical (90°) fall of the sun's rays is provided. As a result, their electrical parameters changed to different values depending on the type of material and construction. Compared to traditional photoelectric batteries, photothermal batteries produced 1.3-1.4 times more electricity depending on the type of material. In the results of the experiment, data were obtained on the open circuit voltage, short circuit current and power of photoelectric and photothermal batteries in hot climate conditions. According to results, the high indicators in terms of electrical parameters are monocrystalline photoelectric and photothermal batteries based on them.

Keywords: monocrystal, polycrystal, photothermal, mobile device, heat collector, cellular polycarbonate, open circuit voltage, short circuit current.

Introduction

While increasing demand to the electric energy the many producing photovoltaic (PV) companies for the deserving place in the world technologies market are rivaling. However, in each concrete PV types there are advantages and drawbacks, which in the real working test regime of external climate conditions are revealing. The factors of the solar radiation, temperature, humidity, dust and air speed are the suchlike samples. As results we shell have the possibility for revealing the suitable PV which can work effective in the regional conditions after testing PV in the open environmental conditions. Unlike of the countries producing the electric energy based on PV Uzbekistan has the continental climate features that are the south regions have the wide temperature ranges, there are many fogs in winter, increasing the summer temperature up to 50 ºC and the high dusting degree are such samples.

The different PV types have the different features to such climate conditions and that is influences to the working regime of the PV. In order to increase the efficiency of using conventional PV, several options of different types of heat collectors from different materials, black and colour metals, polymers [1-6], including cellular polycarbonate have been developed and studied [6]. The efficiency of eight PV in the Kuwait climate conditions in paper had been analyzed [7]. The selected PV in these experiments mono crystal (m-Si), poly crystal (p-Si), PV consisting thin mono crystal Si covered by thin amorphous Si layer (HIT), CdTe, copper indium gallium selenide (CIGS) and amorphous Si had been used. The collected data in period of 12 months had been observed systematically. As results showed that m-Si, p-Si and HIT batteries worked better than other ones in high radiation degrees at the same time, and at lower irradiance levels, it decreased rapidly. However, CIGS PV worked effectively in the low radiation degree. In order to select PV for the desert climate in Xelvan city of Egypt the parameters for mono, poly and amorphous PV in the different climate conditions in period of the several seasons had been measured and analyzed [8]. As experiments results showed, the amorphous Si PV has the maximal sensitivity in the visible part of the spectrum wave length (λ=522nm) and at the same time the maximal working range of the polycrystal Si PV corresponds to the infrared region (λ=922nm).

In the highest solar energy radiation of Europe country, Turkey (Düzce region) the experiments with PV had been carried out too [9]. There experiments in period of total year working regime of PV in the external climate conditions had been lasted. In these experiments monocrystal, polycrystal and amorphous Si had been used. As the experimental results showed the working efficiency for the amorphous, polycrystal and monocrystal Si PV were 4.79%, 11.36% and 13.26%, correspondingly.

The estimations of the working regime of the PV system connected to circuit having power 5.94 kilowatts on the roof of Safi practical sciences school of Morocco (NSASS) on the heat semi dry climate conditions had been carried out [10]. These investigations from June 2018 up to May 2019 had been carried out in which the yearly measuring data collected from batteries based on Si mono crystal, poly crystal and amorphous PV had been analyzed. As results showed that for this region the best battery is the based m-Si PV. The measurements with PV as polycrystal and monocrystal, Cu-In-Ga-Se, Cd-Te and Cu-In-Se batteries both in snow winter and heat summer days had been carried out [11]. It had been revealed in these experiments that the poly crystal PV has the best working regime, as the thinnest film PV was CIGS and CdTe PV has the stable effectiveness. In paper [12] the investigations with the heat and electric characteristics using PV and PVT in the Cameroun climate conditions had been carried out. In these experiments the mono crystal PV and PVT produced by "Trina Solar" and "Felicity Solar" companies had been compared between themselves. As the investigations results showed the PVT of "Trina Solar" company, having maximal power of 305W, produces the average daily energy to 42W (12.3%) more than ones usual battery. At the same time the "Felicity Solar" company PVT, having maximal power of 250W, has the average daily energy to 26.5W (11.1%) more than its usual variant. It should be noted that in climate conditions of Morocco PVT with power 200W constructed by "Solarex MSX-240" company using polycrystal Si collector that based on the water and usual PV electric parameters had been investigated and compared [13]. The heat and electric parameters of the module for six climate zones with the different climate conditions had been measured. In these zones in order to estimation working PVT, it with usual PV in the identical climate conditions the production of energy for month and year had been compared. As results showed that almost in all climate conditions PVT is able produce the energy for month more than PV. As to the reached year degrees of PVT energy, it varied from 15.5% up to 19% in dependence of the climate zones. In paper [14] results of studying PVT parameters when solar radiation intensity is controlling by attracting plates had been presented. It has been revealed there the electric energy production in the south regions is 1.5-1.6 times more than others and in winter period this battery is able obtain the heat water with temperature higher than 50 ^{o}C.

The investigations for the warm and humidity tropical climate zone in Ghana had been carried out [15] too. The main aim of these investigations was comparison of electric energy production with both PVT and usual PV in the open environment conditions. For this purpose the experimental equipment consisting the monocrystal PVT collector that water based and usual monocrystal PV had been installed to the roof of "Kvame Nkrumah" science and technology University of Kumasi in 2019. As results showed the temperature of the PVT having the active cooling system had been decreased essentially and the electrical efficiency of the PV had been increased to 9%. The electric efficiency of the usual PV in 11.00 o'clock was 15.8% and at the same time for the cooled PVT its value was 18%. The electrical energy growing for the total solar day with the active cooling system was 9%, at the same time the power for the without cooled module was 185W and for cooled one equaled to 211W.

As to our investigations in which unlike mentioned above equipment there are the several distinctions:

- the types and power of the selected PV for PVT;
- the collectors constructed on the parallel channel polycarbonate;
- the collector channels have a rectangle shape;
- there are attracting solar radiation plates on the frontal side;
- there are turning on two axes abutting construction;
- the device is mobile.

These factors of the PVT are providing the concrete advantages in comparison of mentioned above alternative batteries. In order to compare the devices parameters in the present paper we present the last measurement results obtained for the PV and PVT. The last years in collaboration with scientists of physical-technical institute by "Solar Physics" scientific production union in order to increase the PV efficiency in the warm climate conditions we have installed to the back side the heat collectors (HC) and attracting plates (reflectors) that is one has constructed the mobile photovoltaic device for testing PV. In the base structure of the device, six of the three types of PVs with a power of 50 W directed at the sun are installed at the same

angle. The positions of three PV and three PVT on the year seasons dependence to the optimal directing angle with concrete instruments can be controlled. To the sides of construction installed three usual PV and PVT we have fixed two modernized reflectors.

We have two main purposes from these experiments. The first, revealing PV type with 50W power and having high working efficiency in the warm climate conditions when the solar radiation intensity is growing by reflectors. The second, observation the different PV based PVT electric efficiency variations on the cooling process in the same conditions and comparison them with usual PV. In the experiments we have obtained the results for the electric parameters variations of the special processed polycrystal, monocrystal PV and PVT back side which has white and black colors.

1. Materials and methods

Scientific research was carried out using PVs with the help of a multifunctional mobile photoelectric device (MMPD) mounted on a two-axle trailer. The prop size is 1300x800 mm and able raise up to 700 kilograms. The number of each installed solar elements (SE) are 36, the power equals 50W, used Si differs on the type and color of the backside. Unlike from the earlier developed devices in our one there are two modernized reflectors attracting the solar light on the long side of connecting PV and PVT device. Value of the attracting coefficient for reflector surface $R \sim 0.5$ and the total area equals to PV total one. These reflectors except working time, that is, in night for protection of PV surface from dusts can be used (see, Figure 1). Movement of the MMPD from one place to other one manually or using mechanical adapter tractor can be realized. List of the consisting parts of the device on Table 1 has been presented. The adapted tractor construction allows us turn the PV around the horizontal or vertical axis manually too.

Fig.1. Measurement of PV and PVT parameters in the natural conditions.

Table 1. List of the consisting parts of the photovoltaic device

No.	Battery type	Quantity	Type	Mechanical parameters	Electric parameters
1	PV	1	Polycrystal Poly-Si: 50W	The protected glass has textured surface (3 mm)	2.99 A, 21.6 V
2	PV	1	Monocrystal Au-FSM-50Вт	The protected glass has textured surface (3 mm)	2.92 A, 21.8 V
3	PV	1	Monocrystal PMS50-Si: 50W	The protected glass has textured surface (3 mm)	3.01 A, 21.5 V
4	PVT	1	Polycrystal Poly-Si: 50W	The protected glass has textured surface (3 mm)	2.99 A, 21.6 V
5	PVT	1	Monocrystal Au-FSM-50Вт	The protected glass has textured surface (3 mm)	2.92 A, 21.8 V
6	PVT	1	Monocrystal PMS50-Si: 50W	The protected glass has textured surface (3 mm)	3.01 A, 21.5 V

The PV electric parameters in the Tashkent climate conditions have been measured. There is possibility directing the PV and PVT to solar manually any time of the day. In order to provide direction of the incident beam perpendicularly to the PV frontal area operator directs PV to solar on each 15-20 minutes.

2. Results and discussion

The research in daily period of 9.00 a.m. up to 16.00 p.m. according to the regimes mentioned above have been carried out. The installed to MMPD PV electric parameters on 14 and 15 April, 2022 by air temperature 19-27^{o}C and air speed 0.2-1.6 m/s have been measured. Figure 2 shows the intensity of solar radiation falling on the surface of PVs on this date depending on the time of day. The intensity of solar radiation was determined by measuring the short circuit current of the standard SE made on the basis of crystalline silicon.

The solar radiation intensity beginning from sunrise up to noon is growing and reaches its maximal value, after that up to sunset is decreasing. Dust and clouds in the atmosphere also cause a decrease in the intensity of light radiation. This situation influences to electric parameters of the PV. As we can see from Figure 2, at 11.00 a.m. the intensity is growing sharply because of the reflectors to an optimal angle have been installed. The dependence of solar radiation intensity on the time we divided to three parts. The first part begins from sunrise up to 11.00 a.m. in moment when the incident angle and intensity are increasing. The second part is the period when the solar radiation intensity on the PV area is growing sharply because of the reflectors to the optimal angles are installed. The finishing third part is the time when after noon the solar radiation intensity is decreasing. It should be noted in the measurements after reflectors to an optimal angle has been installed the solar radiation intensity has been increased for 1.3-1.5 times (see, Figure 2).

We studied the dependences of the open circuit voltage, solar radiation density, short circuit current and electric power on the time. The dependence of open circuit voltage on the time on Figure 3 has been presented. As we see from this Figure that in period from 9.00 a.m. up to 11.00 a.m. the open circuit voltage values have been decreased, namely for monocrystal to ~1.4V, polycrystal to ~1.8V, monocrystal with black color back surface ~2V. The differences of these values for PVT are higher than PV, namely for monocrystal ~1.65V, polycrystal ~2.4V, monocrystal with black color back surface ~2.65V. In this working regime we can see the PVT open circuit voltage is decreasing more than PV. This fact, in our opinion, can be explained that PVT is not able distribute collected heat directly to atmosphere because of to the PVT back surface collector is installed. This tendency up to water transferring via collectors is continuing. In the moments when reflectors begin working (from 11.00 a.m. up to 12.00 a.m.) the open circuit voltages values of usual PV for monocrystal to ~0.8V, polycrystal to ~0.85V, monocrystal with black color back surface ~0.9V are decreased accordingly. As to the PVT these values are for monocrystal to ~0.55V, polycrystal to ~0.9V, monocrystal with black color back surface ~1.1 V are decreased. This difference deals with the heating SE constructed with crystal Si, which is known with the even great differences of this parameter for having great power PV [8].

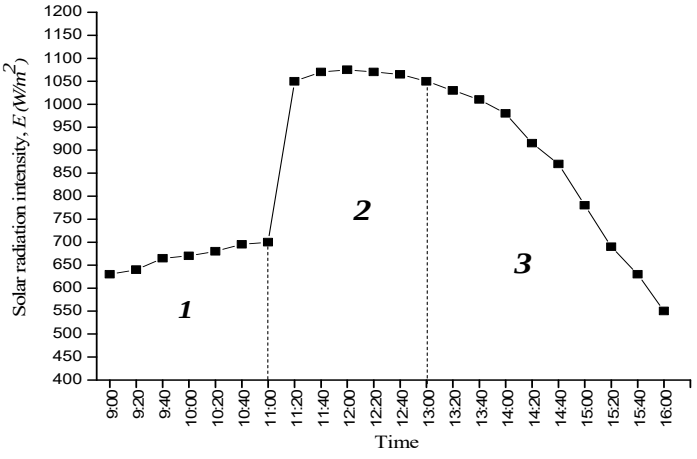

Fig.2. Time dependence of solar radiation intensity

In 12.00 o'clock, water with a temperature of 16-18°C was connected to the heat collector. Because of the temperature dropped on the back surface of PV the open circuit voltage on the PVT for monocrystal to ~2.55V, polycrystal to ~1.45 V, black color back surface monocrystal to ~2.45 V has been increased. In result this effect leads to growing the electric power. After that when solar noon (on 12.40 a.m.) finished the voltage

has been decreased because of the solar radiation intensity changed in range of 0.2-0.35 V on dependence of panel types.

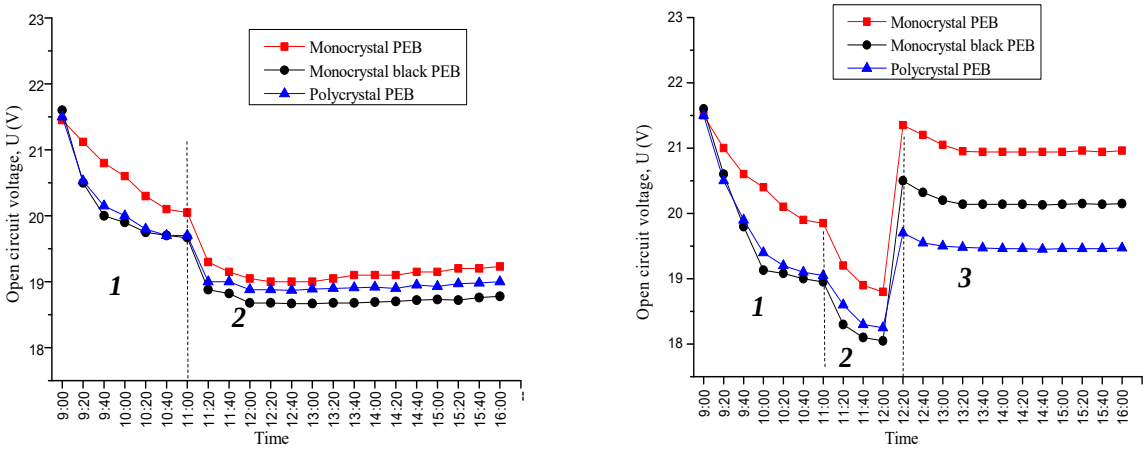

a) Simple PV b) Cooled PV (PVT)

Fig.3. Time dependence of open circuit voltage of PV and PVT during the day.

The dependence of short circuit current on the time on Figure 4 has been presented. As seen from the comparative analysis of results for PV and PVT the short circuit current depends on the solar radiation intensity and panels types. Therefore, after that water opened to the collector in order to cooling the PV back area the future changes of the dependence of short circuit current on the time is defining with environment and atmosphere states.

The PVT electric power according this representation is defined:

$$P = FF \cdot I_{sc} U_{oc}$$

Here I_{sc} is the short circuit current, U_{oc} is the open circuit voltage, FF is the PV fill factor.

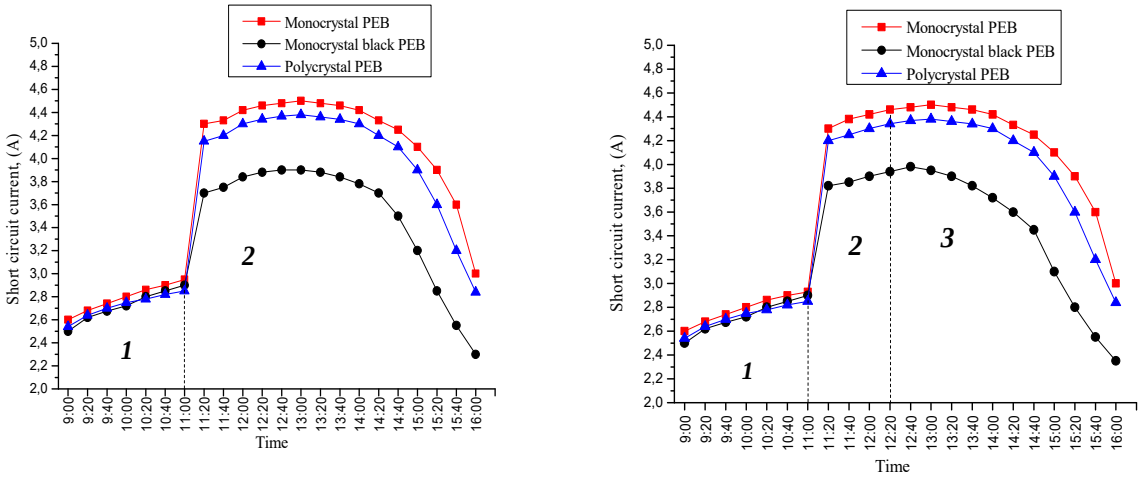

a) Simple PV b) Cooled PV (PVT)

Fig.4. The dependence of short circuit current of PV and PVT on the time.

In this case the PV fill factor is about 0.71-0.72. The dependence of the PV and PVT electric power on the time obtained using mentioned above data on Figure 5 has been presented. As Figures 2, 3 and 4 showed that the process of the dependence of electric power on the time deals with two factors, namely, the solar radiation intensity dropped to PV surface and open circuit voltage depend on the temperature. When PVT is working in second regime it leads to, the first, increasing electric power because of the forcing solar radiation and after, decreasing the open circuit voltage – a bit power stabilization.

When the sun passes noon then the power is decreasing on the solar radiation intensity. As we see from the Figure 5 the electric power maximal values in the usual PV regime equaled to: for monocrystal ~43 watts, polycrystal ~42 watts, black color back surface monocrystal ~36W, and PVT in the cooled regime for monocrystal ~48W, polycrystal ~43W, black color back surface monocrystal ~45W.

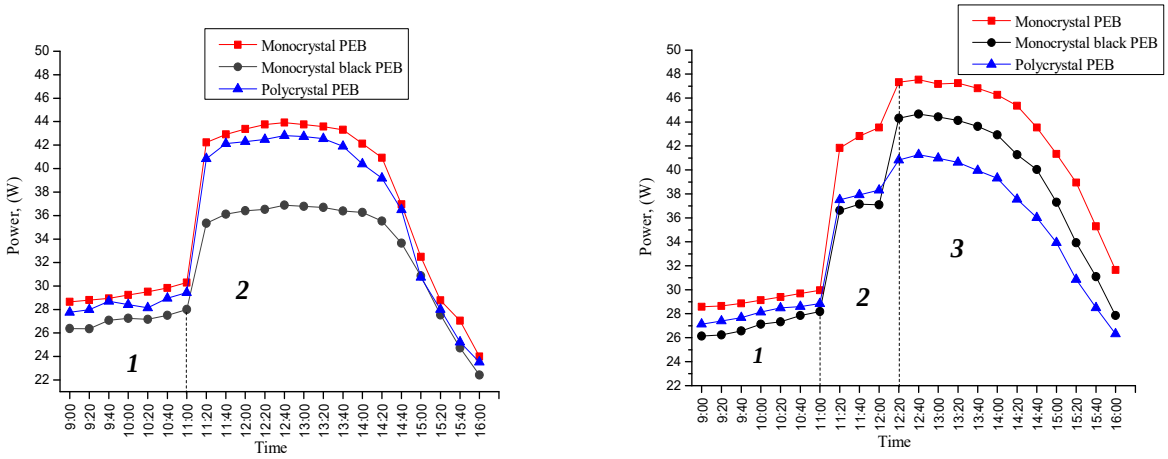

a) Simple PV b) Cooled PV (PVT)

Fig.5. The dependence of electrical power of PV and PVT.

Besides PVT produces additionally the heated water 6-10 litters/hour on temperature 55°C. The creation and use of a power plant based on PV is effective for areas with a shortage of centralized electricity supply and hot water.

Conclusion

Considering that different regions of the republic have unique climatic conditions the developed portable photoelectric device allows to determine in advance the efficiency of PVs planned to be used in this area before building large capacity photoelectric plants. Because of the MMPD is able to moving and controlling easily in small fields we can use one for revealing effective working regime of the different photovoltaic devices long away from the centralized energy sources of the different year seasons in our Republic. The proposing ourselves device can help for revealing energy losses in the different PV and decreasing possibility the losses after analyzing. The basic reasons of the energy losses are the temperature growing, atmosphere pollution and changing positions of PV relatively to sun. This device and developed test method helps us optimize these processes. In experiments we used the polycarbonate collector with new type parallel channel for cooling PV.

REFERENCES

1 Tursunov M.N., et al. Improving the efficiency of a photothermal conversion unit. *Solar engineering,* 2014, No. 4, pp. 84 – 86. [in Russian]

2 Tursunov M.N., et al. Photothermoelectric batteries based on silicon solar cells. *Geliotekhnika,* 2011, No. 1, pp. 72 – 75. [in Russian]

3 Akhatov J.S., et al. Experimental Investigations on PV-T collector under natural condition of Tashkent. *Energy Procedia*, 2013, No. 39, pp. 2327 – 2336.

4 Chow T.T. A review of photovoltaic/thermal hybrid solar technology. *Applied Energy*, 2010, Vol. 87, Issue 2, pp. 365 – 379. doi:10.1016/j.apenergy.2009.06.037

5 Sandnes B.A., et al. Photovoltaic/thermal (PV/T) collector with a polymer absorber plate: experimental study and analytic model. *Solar Energy*, 2002, No. 72. pp. 63 – 73. doi:10.1016/S0038-092X(01)00091-3.

6 Hallmark B., et al. The application of plastic micro capillary films for fast transient micro-heat exchange. *International Journal of Heat and Mass Transfer,* 2008, No. 51. pp. 5344 – 5358. doi:10.1016/j.ijheatmass transfer.2008.01.036

7 Mabrouk A., et al. Comparative performance evaluation of different photovoltaic modules technologies under Kuwait harsh climatic conditions. *Energy Reports,* 2020, Vol. 6, pp. 2689 – 2696. doi: 10.1016/j.egyr.2020.09.034

8 Mosalam M.A., et al. Determination of suitable types of solar cells for optimal outdoor performance in desert climate. *Renewable Energy*, 2000, Vol. 19, Issues 2, pp. 71–74. doi: 10.1016/S0960-1481(99)00018-X

9 Erdem E., et al. Outdoor performance analysis of different PV panel types. *Renewable and Sustainable Energy Reviews,* 2017, Vol. 67, pp. 651 – 661. doi: 10.1016/j.rser.2016.09.051

10 Omar I.N., et al. Outdoor performance analysis of different PV technologies under hot semi-arid climate. *Energy Report*s, 2020, Vol. 6, pp. 36 – 48. doi:10.1016/j.egyr.2020.08.023

11 Visa I., et al. Comparative analysis of the infield response of five types of photovoltaic modules. *Renewable Energy,* 2016, Vol. 95, pp. 178 – 190. doi: 10.1016/j.renene.2016.04.003

12 Lontsi K.A., et al. Experimental study on the electrical and thermal characteristics of a hybrid photovoltaic /thermal water solar collector model using photovoltaic solar modules of different brands. *Energy Conversion and Management,* 2022, Vol, 14, pp. 100198. doi: 10.1016/j.ecmx.2022.100198

13 Ben Z.S., et al. Hybridization of Taguchi method and genetic algorithm to optimize a PVT in different Moroccan climatic zones. *Energy,* 2022, Vol. 250, No. 123802. doi: org/10.1016/j.energy.2022.123802

14 Muminov R.A., et al. Study of the influence of temperature on the parameters of photothermal batteries in the southern regions of the republic. *Alternative energy and ecology*, 2021, No.25, pp. 40 – 47. [in Russian]. doi: 10.1551 8 /isjaee.2021.09.040-047

15 Saeed A.G., et al. Investigation of solar photovoltaic-thermal (PVT) and solar photovoltaic (PV) performance: A case study in Ghana. *Energies,* 2020, Vol. 13, pp. 2701. doi: 10.3390/en13112701

Article accepted for publication 19.10.2022

DOI 10.31489/2022No4/51-57

UDC 53.084.6

AUTOMATED MEASURING SYSTEM FOR INVESTIGATING TEMPERATURE DEPENDENCE OF LOW-FREQUENCY NOISE SPECTRA IN ELECTRONIC ELEMENTS AND STRUCTURES

Ermachikhin A.V., Litvinov V.G., Kholomina T.A., Maslov A.D., Trusov E.P.

Ryazan State Radio Engineering University, Ryazan, Russia, al.erm@mail.ru

In this paper a measuring analytical system for low-frequency noise spectroscopy is presented. The measuring system is adapted for the automated study of low-frequency noise spectra in electronic elements, components and semiconductor materials and structures. A distinctive feature of the proposed measuring system is an automated complex local and precise study of the dependence of the low-frequency noise spectra in the sample on electrical voltage and temperature. The frequency range is 0.001-10000 Hz, DC bias range is 0-50 V and the temperature range is 7-500 K. The measuring system is adapted for use with an atomic force microscope for local measurements of electronic materials and structures noise characteristics. The measuring system makes it possible to obtain a larger amount of experimental data, which makes it possible to draw comprehensive conclusions about the mechanisms and causes of noise generation in the test sample. The results of testing the operation of the measuring system are given as an example of the Schottky diode-like structure study.

Keywords: low-frequency noise spectroscopy; temperature measurements; automation of measurements; barrier structures; atomic force microscopy

Introduction

Commonly during measuring any physical value noise is a negative influencing factor. It adds an error to the results of measurement. Fluctuations of current and voltage in electronic devices determine the lower limit of their sensitivity. In the case of high level of such noise useful component of the signal could be unobtainable. Noises in electronic vacuum and solid-state devices limit the dynamic range of their characteristics. Noises depend on the minimal size of these devices and the chosen minimal value of supply voltage [1].

On the other side, current and voltage fluctuations contain valuable information about internal properties of electrical systems. Thus, an analyzing mechanisms of noise formation provides the necessary data about characteristics and parameters of these systems. In this case fluctuations are used to obtain such information about physical processes leading to noise [2]. Some types of electric noise do not contain useful information. For instance, the thermal noise is the intrinsic and irremovable property of conductive materials with non-zero electrical resistance [3]. The power spectral density (PSD) of the thermal noise depends only on temperature and resistance of noise source. Besides that, it practically contains no useful data. The noise spectrum or dependence of is one of the most significant characteristics of fluctuation process [4, 5].

Shot noise, studied by Schottky in 1918 [6], is generated by discreteness of the number of charge carriers moving from one environment to another. In solid state structures shot noise is associated with charge carrier injection through the depletion region of p-n junction. It looks like a sequence of short pulses which create electrical current. Spectral density of such signal is uniform in a wide frequency range. Therefore, in the first approximation shot noise is considered as a white according to the corresponding PSD. Shot noise is the same as thermal noise. It doesn't provide information about the energy spectrum of electronic states in semiconductors. The low frequency (LF) noise in the metals and semiconductors used to control the quality of electronic components. It's spectral density depends on frequency f as a function $1/f^{\gamma}$, where γ is in the range 0.6-2.5 [1, 7].

Modern computer techniques increased the level of experiments to investigate noises [8]. Special attention is focused on automation of data processing and obtaining to achieve real time calculations. Nowadays it is hard to find a general universal model of generating electrical noise in all semiconductor and metal devices and structures [1, 2]. There are some models of noise generation for some semiconductor devices and metal films [1] due to the large number of non-obvious factors affecting the formation of the

.

noise component of electrical signals. The temperature dependent noise is used to determine the electromigration activation energy, interconnect reliability, phase transitions, radiation damage, etc. [9-11].

To carry out precision studies of semiconductor barrier structures by LF noise spectroscopy the use of specialized equipment is required to measure the temperature dependence of the spectral density of noise power. On the other hand, local electrical measurements can be carried out using atomic force microscopy. Of interest is the joint use of atomic force microscopy to ensure local measurement and noise spectroscopy. A sensitive preamplifier is required to match the conductive probe of an atomic force microscope with a noise spectrometer.

As an amplifier of the noise signal for example Stanford Research Systems SR560 [12] or Ithaco 1211 [13] are used. Dynamic signal analyzers such as Stanford Research Systems SR785 [12] or SR780 [13], and other measuring devises as Agilent 5052A [14], for example, are applied. There are complete commercial systems for measuring noise such as NMS-NOYSYS 7 (Synergie Concept, French). Its advantage is easy to use and availability of software for managing and plotting noise spectra. However, such equipment provides several limitations. For example, papers [12-14] present spectra with bottom frequency limit 1 Hz, while the described in this paper system has the bottom range equals 0.001 Hz. NMS-NOYSYS 7 has lower sampling rates (250 kHz), bias voltage (till 10 V) and initial frequency (1 Hz). The complete software using leads to limitations about spectra processing and plotting.

1. Description of the measuring system

The influence of intrinsic noise of the amplifier on measurements was reduced by designing of the low noise amplifier with 10 parallel channels (Fig. 1). Application of N parallel amplifying channels allows decreasing the level of intrinsic noise in √N times. A disadvantage of the solution is increase of input capacitance in N times and decrease of input amplifier resistance in N times. The input level of amplifier noise is 3.9 nV/√Hz at 1 kHz (for comparison: input noise of amplifier SR560 is 10 nV/√Hz t 1 kHz). Changing resistance of R1, R2, R3, R4, provides the necessary gain factor.

During developing topology of amplifier, we wired the conductive paths in the way that power bus and signal bus were located as far as possible from each other. We used low-noise operational amplifiers AD795 that has normalized by the input voltage of the noise in the range of 0.1-10000 Hz.

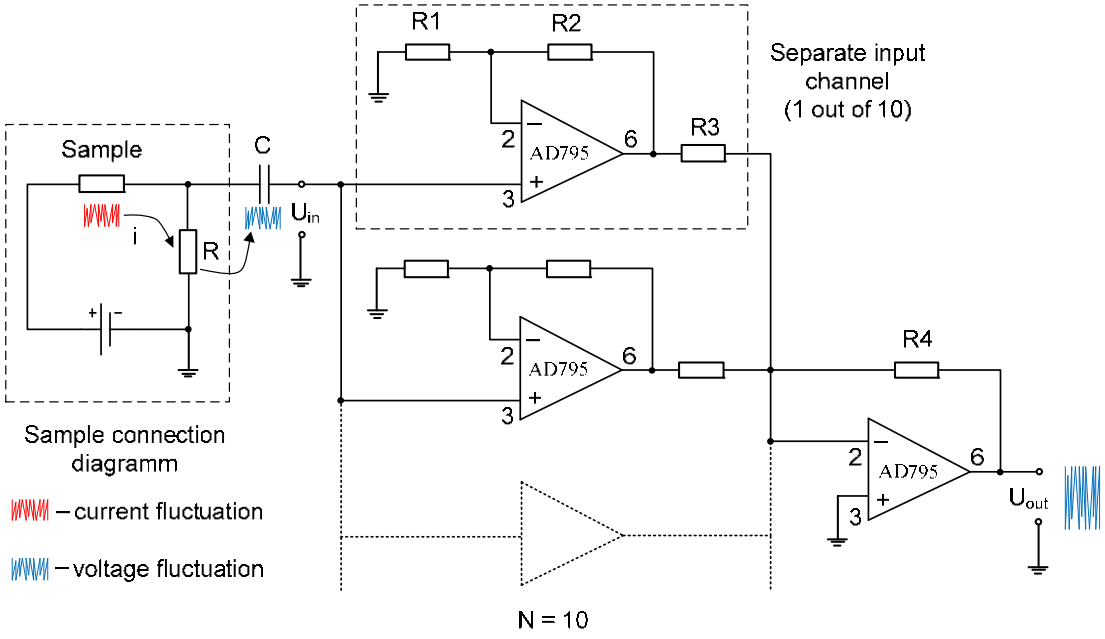

Fig.1. The scheme of the sample wiring with constant bias voltage source to the preamplifier

A constant voltage is applied to the sample from the bias circuit. The current fluctuation leads to appearance of voltage fluctuation on the reference resistor R. That fluctuation arrives the input of pre amplifier through the capacitor C blocking constant component. C is the high-quality film capacitor at the input of the amplifier. In our case R = 1-100 MΩ and C = 2 × 4.7 μF that provide RC = 9.4-940 s. The

capacitor helps to remove the constant component of voltage on the reference resistor and work with voltage noise component only. The choice of the resistor R value is determined by the internal resistance of the sample and the lower boundary frequency in the noise spectrum. The upper frequency limit of the preamplifier can be increased by changing the parameters of the frequency correction circuits. The frequency limit of 10 kHz is due to the fact that the setup was designed specifically for studying low-frequency noise.

For investigating temperature dependence of noise SPD closed cycle helium cryostat Janis CCS400/204N with thermocontroller Lakeshore 335 are included in the measuring system (Fig. 2). The cryostat and the thermocontroller provide a temperature range of 7-500 K and the accuracy of maintaining the temperature to 0.1 K. Galvanic elements that reduce influence of noises from electrical network are used to supply the amplifier and apply bias voltage to the sample. The signal through the data acquisition board NI PCIe-6361 and terminal block NI BNC-2120 goes to the PC, which records, processes and stores the received data. The constant bias voltage is applied to the sample by commutation of the galvanic elements from the PC through the terminal block NI BNC-2120 using reed relay with gold-plated contacts. Parameters of the measuring system are shown in the table 1. The sensitivity of the preamplifier allows it to be connected to a conductive probe of the atomic force microscope and to conduct local measurements of the noise spectrum.

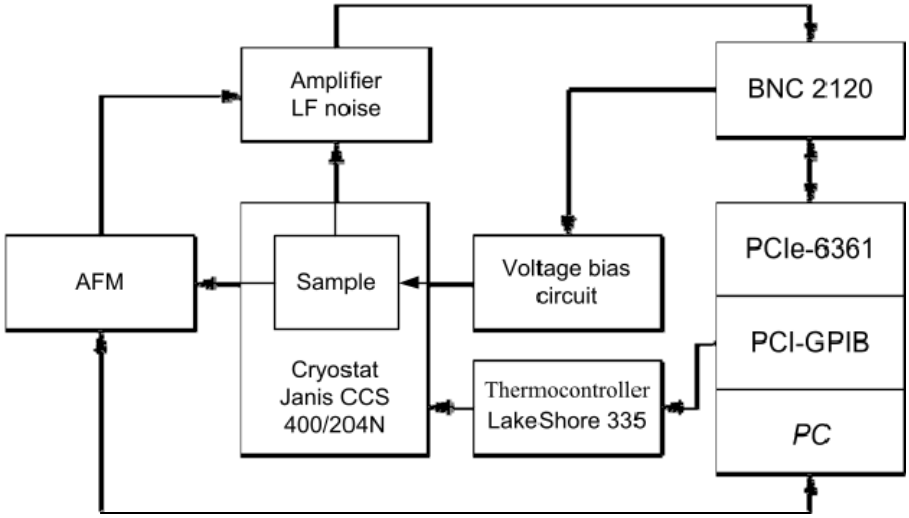

Fig. 2. The block diagram of the measuring system for low-frequency spectroscopy.

Table 1. Parameters of the LF noise spectroscopy measuring system

Parameter	**Range**	**Parameter change step**
Bias voltage	1.5-49.5 V	1.5 or 9 V
Frequency range	0.001 Hz – 10 kHz	0.001, 0.01, 0.1 and 1 Hz
Experiment duration	not limited	-
Temperature range	7-500 K	1-100 K
Gain factor	1-1000	A multiple of 10
Amplifier input impedance	1-200 MΩ	-
Sampling frequency	up to 2 MHz	-
ADC bit	16 bit	-

One can set bias voltage change step as 1.5 or 9.0 V depending on the switching galvanic element. Addition of voltage divider in the switching circuit provides lower steps. Time to receive one PSD spectrum depends on the chosen frequency range, i.e. minimum set frequency. In the case of minimum frequency equals 1 Hz frequency change step is also set as 1 Hz, that provides measuring duration equals at least 1s. In the case of minimum frequency 0.01 Hz the step value is 0.01 Hz and the duration is not less than 100 s. Resistance of the reference resistor is chosen as approximately equal to dynamic active resistance of the sample.

.

2. Automation of measurements

Commonly, noise parameters of electronic structures are measured at quasi-steady state condition, i.e. at constant current value and constant temperature. Therefore, algorithms controlling the equipment have to consider temporary pauses that are necessary for total relaxation of transient processes, caused by change of voltage or temperature. Increase of pause duration provides approximately steady state condition, however it increases duration of experiments. Thus, pause duration is chosen according to the time of establishing constant current and duration of measurements. Duration of pauses is estimated experimentally by series of preliminary experiments for different samples and depends on electrical resistance of these samples.

In practice, the higher resistance means higher pause and measurement durations, which defined by time constant of RC circuit, formed by resistance of the sample, the reference resistance and the input capacitor blocking constant component at the input of the pre-amplifier [6]. For automatic recording experimental data one can set a delay after changing of external factors. Another way is tracking the average voltage across the sample. According to the data one finds a valid range of values (Fig. 3). This way is preferable as it reduces the duration of the experiment.

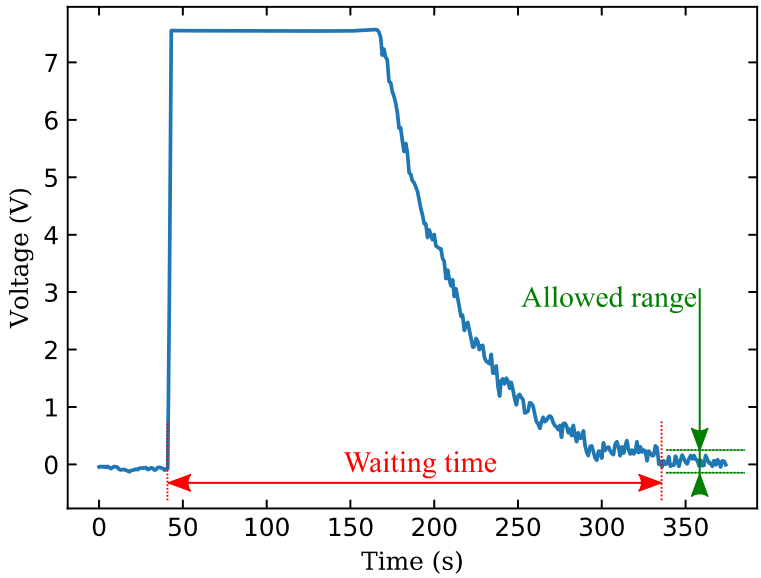

Fig. 3. Factors to start automated experimental measurements

The measuring system is controlled by the software written in LabVIEW [15, 16]. A bias voltage is applied by transferring a specific binary code to the digital block NI BNC-2120. The switching system after receiving this code includes the required number of galvanic elements in the circuit. The system could be simplified due to replacing the bias circuit containing galvanic cells by applying a bias voltage from a controlled source. Such approach helps to set a bias voltage with different steps. However it increases noise level from the electric network.

PSD is calculated using LabVIEW built-in libraries. For fast Fourier transform algorithm radix-2 [17] is used. Blackman-Harris window is used. That helps to display the obtained data in the form of time dependence of voltage and calculated noise spectrum in real time. This spectrum is found and shown for different voltage values with subtracted average trend. To get PSD data it is necessary to choose a weight function and frequency range before starting averaging and recording the data. As fluctuations are stochastic, so we average noise PSD over several measurements for reproducible result. We choose number of averages according to the case, that dispersion is slightly decreased with increase of number of averages.

As a results PC records only averaged noise PSD and shows all the data obtained at every measurement. Depending on the chosen value range, PSD can contain millions values due to the minimum frequency of the measuring system 0.001 Hz with step 0.001 Hz. Noise meters are usually designed for a lower operating frequency 1 Hz. The used sampling frequency is many times higher than the upper frequency of the studied signals 10 kHz. Artifacts associated with the influence of sampling frequency and digital filtering can fall into the high-frequency part of the spectrum.

3. Experiment

According to the physical model [18-20] LF noise PSD $S(\omega)$ as a steady state random process is described by superposition of the Lorentz function components:

$$S(\omega) = C\frac{\tau}{1+\omega^2\tau^2}, \tag{1}$$

where ω is the circular frequency ($\omega = 2\pi f$); C is the proportionality coefficient; τ is the relaxation time of an activation processes.

Characteristic points on the frequency axis f_b, corresponding to the change in the slope of the dependences are called as the break frequencies [1]. The characteristic frequencies correspond to the relaxation time τ of the process responsible for LF noise generation [21]:

$$\omega\tau = 1. \tag{2}$$

In semiconductor barrier structures the generation process is influenced by defects that create deep energy levels in a band gap. Determination of deep level ionization energy ΔE_t by LF noise spectroscopy is provided by a model function describing change in relaxation time of deep centers recharging $\tau(T)$, according to Boltzmann's law:

$$\tau = \tau_0 \cdot \exp\left(\frac{\Delta E_t}{k_B T}\right). \tag{3}$$

where k_B – Boltzmann constant, T – temperature, physical meaning of τ_0 is different and depends on a current physical model (for instance, τ could be relaxation time of crystal lattice oscillation) [22].

Relaxation time is defined from a break frequency of PSD dependence at constant temperature. A set of the measured relaxation times at different temperatures allows to construct Arrhenius plot. Analyzing its tilt angle gives the value of ionization energy ΔE_t. Arrhenius lines are plotted in semi-logarithmic scale versus reverse temperature:

$$ln(\tau) = ln(\tau_0) + \frac{\Delta E_t}{k_B T}. \tag{4}$$

Using the developed measuring system, we investigated test silicon Schottky diode with n-type base containing electrically active deep centers in the temperature range 90-290 K. The obtained LF noise PSD (Fig. 5) one can divide into three temperature sections with characteristic break frequencies: 100-140 K, 160-190 K and 270-290 K. Temperature investigations are measured in the frequency range 10^{-1}-10^4 Hz. In this case, there was no need to make noise measurements at frequencies below 0.1 Hz due to the characteristics of the sample. A feature of the silicon sample is the fact that defects with deep energy levels in the selected temperature range appear on the noise spectrum in the frequency range up to 10 kHz.

The attachment of Fig. 4 shows Arrhenius plot in logarithmic scale. The calculated ionization energies are presented in Table 2. We didn't detect deep centers in this test sample using DLTS [23] due to the limited sensitivity of this method in the range of relaxation times more than 0.1 s.

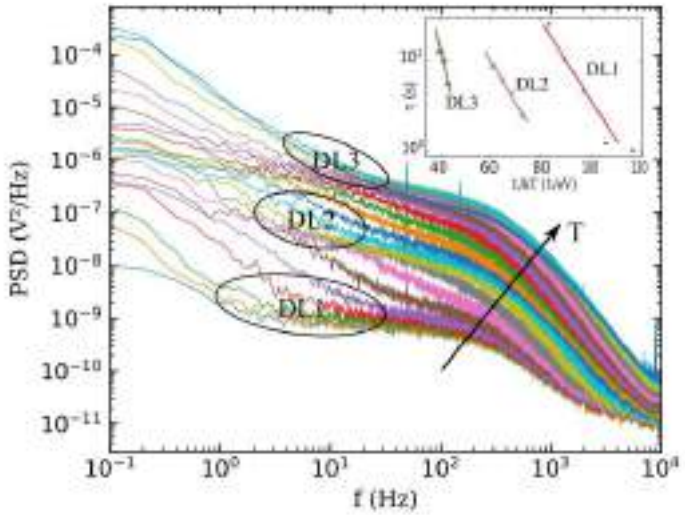

Fig. 4. LF noise PSD of the test Schottky diode at different temperatures

.

Table 2. Parameters of deep levels

Deep level	DL1	DL2	DL3
ΔW_t (meV)	101	107	279
τ_0 (s)	$1.86 \cdot 10^{-6}$	$2.63 \cdot 10^{-5}$	$1.76 \cdot 10^{-7}$

Noise spectroscopy allows to study influence of electric field on reduction of potential barrier for charge carrier emission from deep levels of their capturing by deep levels according to the Poole-Frenkel effect [21]:

$$\Delta E_t = k_B T \ln\left(\frac{1}{2\pi f_b \tau_0}\right) + \sqrt{\frac{q}{\pi\varepsilon\varepsilon_0}\sqrt{\frac{qN}{2\varepsilon\varepsilon_0}(U_k - U)}}\,, \tag{5}$$

where U_k – contact potential difference, q – electric charge, N – shallow dopant concentration, ε_0 – dielectric constant, ε – permittivity, f_b – break frequency.

Doping concentration and contact potential difference could be found from capacitance-voltage (C-V) method [24]. The high break frequency at room temperature equals 350 Hz. Using RLC-meter Agilent E4980A (measuring complex described in Ref.23) we measured C-V characteristics and found U_k = 0.4 V. Ionization energy of deep level DL4 is ΔE_t = 0.54 eV.

LF noise PSD measured at reverse bias voltage in the range 1.4-20.2 V (Fig. 5). Change in the break frequencies under increase of bias voltage (attachment of Fig. 5) gives the data for calculating dependence of potential barrier reduction for charge carriers involved in recharging of DL4 from electric field in the base of the test diode. Dependence, shown in Fig. 6, points on grow of DL4 ionization energy reduction with increase of applied electric field.

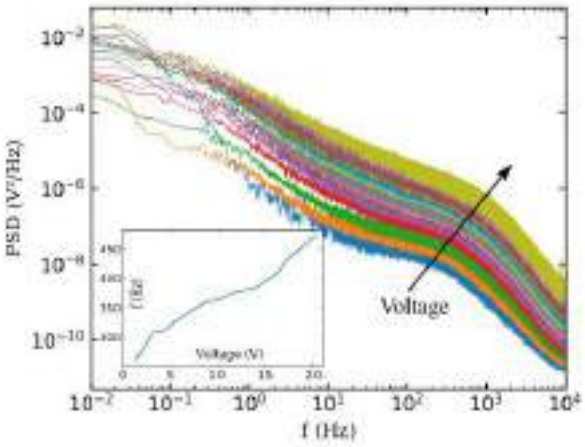

Fig. 5. LF noise PSD at different applied voltage

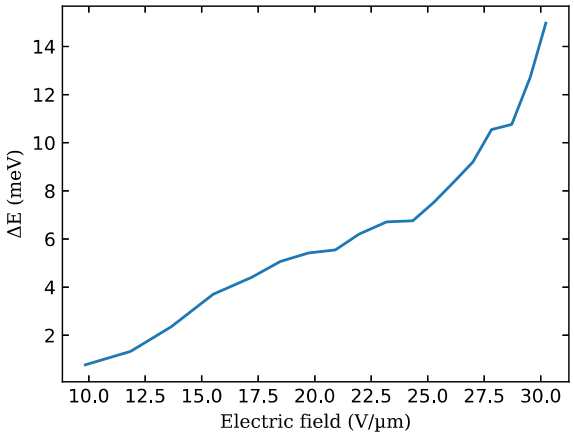

Fig. 6. Dependence presents reduction of ionization energy of deep level DL4 from electric field in the base of the Schottky diode

Conclusion

Using the proposed measuring system it was possible to demonstrate a precision measurement of the of the low frequency noise spectra temperature dependence and determine the parameters of defects with deep energy levels in a semiconductor barrier structure.

The system provides studying influence of electric field and temperature on noise spectra of electronics elements and structures. Application of modern approaches for measuring system automation makes LF noise spectroscopy powerful sensitive and informative tool for investigating of electronic energy levels in semiconductor barrier structures. The use of a conducting probe of an atomic force microscope in the measuring cell to form an electrical contact to the test sample makes it possible to perform a local study of the noise spectra.

Acknowledgements

This work was carried out with the financial support of Ministry of Science and Higher Education of the Russian Federation (FSSN-2020-0003) using the equipment of the Regional Center of Probe Microscopy for Collective Use at the Ryazan State Radio Engineering University named after V.F.Utkin.

References

1 Zhigalsky G.P. *Fluctuations and noise in electronic solid state devices*. Moscow, 2012, 512 p. [in Russian]

2 Razumenko D.V. Low-frequency noise of electronic components as a tool for diagnosing internal defects. *Components and technology*, 2008, No. 9, pp. 168-174. [in Russian]

3 Buckingham M.J. *Noise in electronic devices and systems*. New York: Ellis Horwood Ltd. 1983, 399 p.

4 Kogan Sh.M. Low-frequency current noise with 1/f spectrum in solids. *Soviet Physics Uspekhi,* 1985, Vol. 28, pp. 170-196. doi: 10.1070/PU1985v028n02ABEH003853

5 Bonani F., Ghione G. *Noise in Semiconductor Devices*. Springer-Verlag Berlin Heidelberg, 2001, Vol. 7, pp. 1-38. doi: 10.1007/978-3-662-04530-5_1

6 Schottky W. Über spontane stromschwankungen in verschiedenen elektrizitatsleitern. *Ann. der Phys.,* 1918, Vol.57, pp. 541-567. doi: 10.1002/andp.19183622304

7 Sikula J., Levinshtein M. *Advanced Experimental Methods for Noise Research in Nanoscale Electronic Devices*. Nato Science Series II: Springer Netherlands, 2004, 368 p. doi: 10.1007/1-4020-2170-4

8 Kostryukov S.A., Ermachikhin A.V., Litvinov V.G., Kholomina T.A., Rybin N.B. A measuring System for the Spectroscopy of the Low-Frequency Noise of Semiconductor Diode Structures. *Measurement Techniques*, 2013, Vol.56, Iss. 9, pp. 1066-1071. doi: 10.1007/s11018-013-0331-x

9 Liu G., Rumyantsev S., Bloodgood M.A., et al. Low-Frequency Electronic Noise in Quasi-1D TaSe3 van der Waals Nanowires. *Nano Letters,* 2017, Vol. 17, 1, pp. 377-383. doi: 10.1021/acs.nanolett.6b04334

10 Empante T.A., Martinez A., Wurch M., et al. Low Resistivity and High Breakdown Current Density of 10-nm Diameter van der Waals TaSe3Nanowiresby Chemical Vapor Deposition. *Nano Letters*, 2019, Vol. 19, no. 7, pp. 4355-4361. doi: 10.1021/acs.nanolett.9b00958

11 Geremew A., Qian C., Abelson A., Rumyantsev S., Kargar F., Lawbce M., Balandin A.A. Low-frequency electronic noise in superlattice and random-packed thin films of colloidal quantum dots. *Nanoscale*, 2019, Vol. 11, No.42, pp. 20171-20178. doi: 10.1039/C9NR06899F

12 Kumar A., Heilmann M., Latzel M., Kapoor R., Sharma I., Göbelt M., Christiansen S.H., Kumar V., Singh R. Barrier inhomogeneities limited current and 1/f noise transport in GaN based nanoscale Schottky barrier diodes. *Scientific Reports*, 2016, Vol. 6, 27553. doi: 10.1038/srep27553

13 Song Y., Jeong H., Chung S., et al. Origin of multi-level switching and telegraphic noise in organic nanocomposite memory devices. *Scientific Reports*, 2016, Vol. 6, 33967. doi: 10.1038/srep33967

14 Luan X., Huang Y., Li Y., McMillan J.F., Zheng J., Huang S.-W., Hsieh P.-C., Gu T., Wang Di, Hati A., Howe D.A, Wen G., Yu M., Lo G., Kwong D.-L., Wong C.W. An integrated low phase noise radiation-pressure-driven optomechanical oscillator chipset. *Scientific Reports,* 2014, Vol. 4, 6842. doi: 10.1038/srep06842

15 Essick J. *Hands-On Introduction to LabVIEW for Scientists and Engineers*. Oxford Univ. Press, 2012, 624p.

16 Zhao M., Huang J.X., Wong M.H., et al. Versatile computer-controlled system for characterization of gas sensing materials. *Review of Scientific Instruments*, 2011, Vol. 82, Iss. 10, 105001. doi: 10.1063/1.3648132

17 Das A.D., Mahapatra K.K. Real-Time Implementation of Fast Fourier Transform (FFT) and Finding the Power Spectrum Using LabVIEW and Compact RIO. *Proceeding of the International Conference on Communication Systems and Network Technologies*, 2013, pp. 169-173. doi: 10.1109/CSNT.2013.45

18 Zhigal'skii G.P. 1/fnoise and nonlinear effects in thin metal films. *Physics-Uspekhi,* 1997, Vol. 40, pp. 599-622. DOI: 10.1070/PU1997v040n06ABEH000246

19 Scholz F., Hwang J.M., Schroder D.K. Low frequency noise and DLTS as semiconductor device characterization tools. *Solid-State Electron*, 1988, Vol. 31, No. 2, pp. 205-218. doi: 10.1016/0038-1101(88)90129-3

20 Yau L.D., Sah C.T. Theory and experiments of low-frequency generation-recombination noise in MOS-transistors. *IEEE Trans. Electron. Devices*, 1969, Vol. ED-16, No. 2, pp. 170-177. doi: 10.1109/T-ED.1969.16586

21 Kholomina T.A. Peculiarities of LF Noise Generation Processes in Semiconductor Barrier Structures. *Bulletin of RGRTU*, 2012, No. 39-2, pp. 117-121. [in Russian]

22 Zhigal'skii G.P., Kholomina T.A. Excess noise and deep levels in GaAs detectors of nuclear particles and ionizing radiation. *J. Commun. Technol. Electron*., 2015, Vol. 60 (6), pp. 517–542. doi: 10.1134/S1064226915060200

23 Ermachikhin A.V., Litvinov V.G. An Automated Measuring System for Current Deep-Level Transient Spectroscopy. *Instruments and Experimental Techniques*, 2018, Vol. 61, Iss. 2, pp. 277-282. doi: 10.1063/1.1663719

24 Sze S.M., Ng Kwok.K. *Physics of Semiconductor Devices*. Hoboken: Wiley, 2006, 815 p. doi: 10.1002/0470068329

Article accepted for publication 20.07.2022

.

DOI 10.31489/2022No4/58-66

UDC 629.7.05; 629.783

DEVELOPMENT OF ONBOARD CONTROL SYSTEM ARCHITECTURE FOR NANOSATELLITES

Alipbayev K.[1], Sarsenbayev Y.[2], Mussina A.[2]*, Nurgizat Y.[1]

[1] Institute of Telecommunications and Space Engineering, Almaty University of Power Energy and Telecommunications named after G.Daukeev, Almaty, Kazakhstan
[2] Ghalam Limited Liability Partnership, Astana, Kazakhstan, a.mussina@ghalam.kz

This article presents development of the architecture of the onboard control system. In particular, the hardware and circuit solutions in the development of the module are presented. Technical solutions, the concept of the mechanical layout of the onboard control system and block diagrams of the presented modules of the onboard complex are also discussed. Main functions of the on-board software are described in details, which will help in design and development of ultra-small artificial satellites. This article serves as a new approach for how to effectively configure and operate the on-board control system.

Keywords: onboard computer, cube sat, software defined radio, Field-Programmable Gate Array.

Introduction

Nowadays satellite technologies and components allow designing very small sized satellites (nanosatellites) to reduce overall cost of the space systems. The nanosatellites belong to the class of small satellites weighing less than 10 kg and this type of small satellite is used in most Low Earth Orbit (LEO) missions with different payloads. Most of them uses CUBESAT class standard and their numbers in orbit is rapidly grows [1]. In this frame the development multifunctional control systems for nanosatellites in compact form factor is getting relevant meet the growing demand in small space systems.

Currently accepted, a OBCS is a set of modules and software designed to control attitude and orbit of the satellites and operations of on-board equipment. The classic OBCS plays central role in the operation of a spacecraft and its functions are:

- Attitude and orbit control (AOCS units, OBC);
- Executing realtime & time-tag telecommands (OBC);
- Telemetry data management (OBC);
- Platform & Payload housekeeping (OBC);
- On-board time synchronization (GPS receiver);
- Failure detection, isolation and recovery (OBC);
- Reception, validation, decoding and distribution commands to other subsystem in Emergency modes (TT&C subsystem);
- Collection, processing and analysis of control and diagnostic information;
- Telecommand uploading and execution, telemetry downlinking to Ground Control station.

The aim of considered development is to provide integrated solution for small/nano satellite systems which effectively implements abovementioned OBCS functions in a single on-board module and furthermore covers functions of other subsystems in a satellite platform:

- Payload computer function with flexible interface for the most payload;
- High-speed data transceivers up to 6 GHz based on SDR technology.

This article presents development of architecture of On-Board Control System (OBCS) with a unified payload interface for nanosatellites implemented using software-defined FPGAs. The technological approach reduces weight, power consumption, size and cost of the satellite. The design is suitable as to CubeSAT and nano/micro satellite design in terms of mechanical and electrical compatibility. The development is patented with patent for Spacecraft onboard control system utility model #6912 in Republic of Kazakhstan. [2]

The concept of building OBCS were developed based on the requirements of a systematic approach to the design of on-board controls and the actual practice of flight control of spacecraft (S/C) of various classes and purposes.

1. Development of the architecture of the OBCS hardware

The section describes the main components of the OBCS, the corresponding modules and computational functions. Figure 1 shows a generalized architecture and a diagram of the use of OBCS. The considered onboard control system consists of 3 functional modules physically presented in the form of printed circuit boards:

– Processor module - the main component of the OBCS, in which computing functions are concentrated, as well as memory modules for storage housekeeping data, data from the payloads are located in dedicated memory (NAND);

– RF module - a board for converting the high frequency (HF) signal into digital form for subsequent processing, as well as the generated digital signal into analog form in the corresponding HF range. Filters are used in the path to select the desired working band. Through high-frequency connectors and HF cables, signals are sent / received to the HF path unit, where amplification occurs to the required level;

– Interface board - a board for connecting external interfaces to the OBCS (except HF).

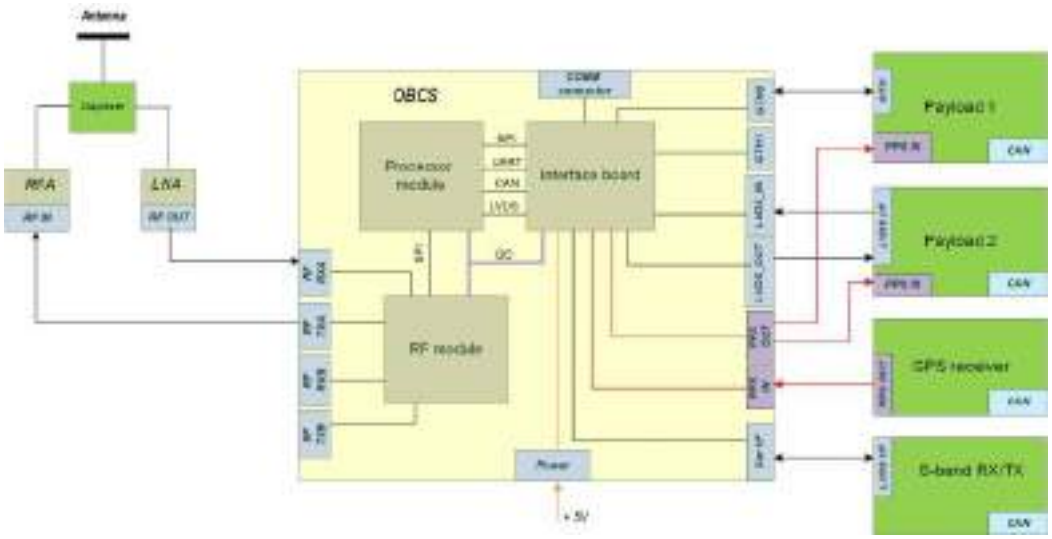

Fig. 1. OBCS usage diagram.

During interfaces definition, the usage of OBCS was taken into account to solve a wide class of tasks in such missions as remote sensing of Earth, radar and scientific ones. Table 1 provides a list of the main interfaces that can be used for most nanosatellite platforms and CUBSAT projects.

Table 1. Definition of OBCS interfaces.

Interface	Type of signals	Protocol	Quantity	Transfer rate per 1 interface
LVDS I/O	LVDS33	Serial+Clock	32	622 Mbit/s
GTH transceiver	LVDS33	Serial+Clock	4	6 Gbit/s
CAN I/O	LVCMOS33	CAN SU2	2	500 Kbit/s
UART	LVCMOS33	Own	4	115.2 Kbit/s
I2C	LVCMOS33	I2C	2	400 Kbit/s
SPI	LVCMOS33	SPI	2	25 Mbit/s
PPS I/O	LVDS33	-	4	1 Hz

.

The concept of mechanical design is presented in Figure 2 and based on a ”sandwich” layout, as in CUBESAT, when the boards form in a multi-tiered structure, but unlike standard connectors, using highly reliable inter-board connectors of the Razor Beam type, which were used in the previous model of the on-board computer in the KazSTSat project [3].

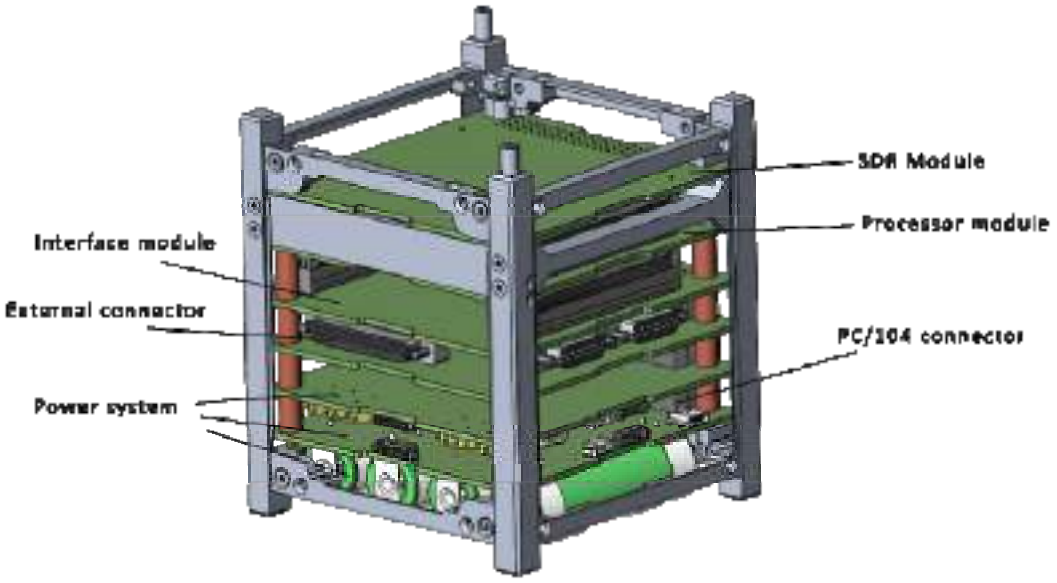

Fig. 2. The concept of the mechanical layout of the OBCS.

2. OBCS Software Architecture

In frame of development process of the architecture of the On-Board Software (OBSW), options for implementing architectural solutions of several satellite manufacturers were studied, as well as information from scientific sources in the field of S/C design and OBSW development were analyzed.

The traditional architecture of the S/C OBSW includes three main levels: the low or basic software level, the service level and the application level [4]. The low-level layer consists of a Real-Time Operating System (RTOS) and interface device drivers. The service layer is a layer of data handling and memory services. The application layer includes system management, subsystem management, and payload applications.

The research takes advantage of using orbit and design data from two different missions KazEOSat-1 and KazSTSat [5] for the analysis. The architecture of the onboard software of the KazEOSat-1 [6] and KazSTSAT [3] remote sensing SC has a basic structure corresponding to the traditional static architecture of the OBSW, considered in [7] and [8].

Widely used in the design and development of OBSW ultra-small Earth satellites flight software commercial frameworks consist of three main layers. At the same time, in order to maintain flexibility and applicability both to the tasks of various S/C and to various platforms, the layers differ from the traditional OS architecture: the service level includes additional blocks of system components and libraries for compatibility with the Platform Support Package level (PSP). [9]

Applying the results of the analysis of the OBSW design solutions, as well as the experience in the software development of the universal on-board computer OBCARM, the technological payload of the space system for scientific and technological purposes KazSTSAT, the architecture of the OBSW was developed (Figure 3), taking into account the OBCS hardware. The presented architecture consists of three main levels: the level of hardware and basic software, the level of services and the application level.

The application layer performs the main modes of the SC and mission control, monitoring of the technical condition of the SC, management of subsystems and the system level FDIR (Failure Detection, Isolation and Recovery). In order to support the platform and payload operations, On-Board Control Procedures (OBCP) [8] provide the capability to interact with the OBSW by executing script files previously uploaded on board by operators of the ground station [7].

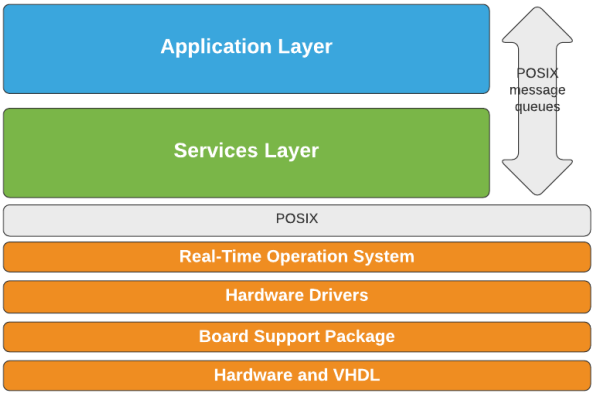

Fig. 3. On-board software architecture.

The service layer contains general-purpose data processing services, as well as services of the centralized Package Usage Standard (PUS) [10]. In addition, this layer includes hardware controllers offering interfaces to the input/output (I/O) boards of the OBCS and communication buses, such as CAN [11], and serial channels. Server-level software objects (CAN server, serial data transfer server, etc.) implement communication protocols, provide interfaces to the CAN bus, serial ports, etc.

The low-level software layer includes a real-time operating system (RTOS) and the on-board computer hardware drivers that provide access to dual-redundant central processing unit, peripherals and I/O boards. The core of the real-time operating system and the Board Support Package (BSP) provides the main services for the on-board computer software (scheduling, message sending, task manager, etc.), and also provides support for interfaces for various hardware modules.

BSP is a set of software used to initialize hardware devices on a board with a Zynq UltraScale+ processor module and implement procedures related to this board that can be used by the kernel and the device drivers.

The OBSW function blocks located on top of the RTOS use POSIX message queues for inter-process communication. The architecture of the service levels, services and applications allows to expand the system.

The main on-board software of the OBCS runs on the Zynq UltraScale+ SoC processor module located on the application processor board and performs the main functional tasks of the on-board computer/payload module. The main function of the OBSW is to provide management, control and data processing to support the operation of the S/C using the various space communications protocols, as well as performing the following main functions:

- data management and ground control and control support;
- S/C modes management;
- orientation and orbit control;
- platform management;
- payload monitoring.

The processes for performing these functions are mainly implemented at the services and applications level. The architecture of the OBSW with an expanded structure of the application and services layers is shown in Figure 4, where CTRL is the control vector, St_V is the status vector, AOCS_TLM is the AOCS telemetry vector, AOCS_CTRL is the AOCS control vector, PL_CTRL is the Payload control vector, PL_TLM is the Payload telemetry vector, Sat_CTRL is the SC subsystems control vector, MP_St_V is the SC subsystems telemetry vector.

Processes in the system are grouped according to functional blocks based on data input/output paths, data processing/formatting, protocol stacks and algorithmic elements. OBSW uses an event-driven architecture in real-time for I/O processes using the preemption mechanisms present in the operating system, while applications and services operate in round-robin scheduling slots within their priority group. OBSW communicates with SC devices (star tracker, GPS receiver, transponders, transmitters, payload instruments, etc.) via data bus and serial channels (LVDS interface, CAN, I2C interface, PPS, UART and SPI interfaces). Exchange of telemetry and telecommands with the ground segment based on the PUS (Package Utilization Standard) standard [10].

.

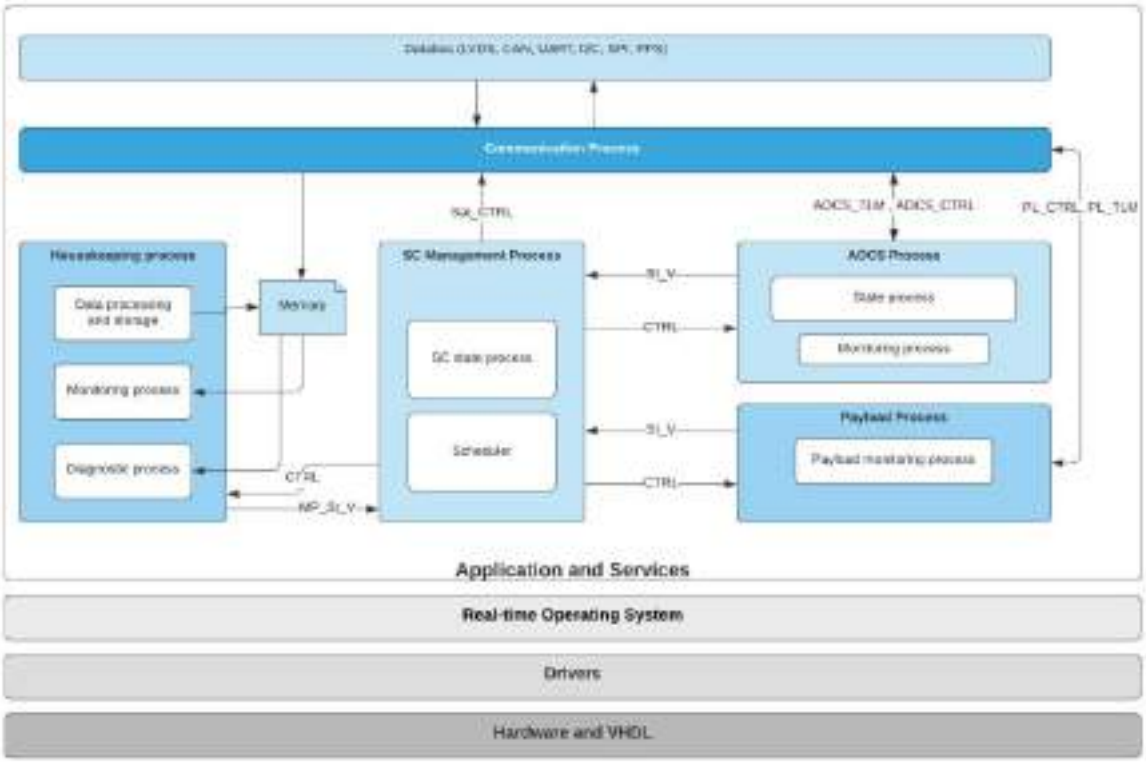

Fig. 4. OBSW architecture. Application and Services level.

In Figure 5 working algorithm of the Satellite management process is shown, which is the key software component mastering other software components in OBSW. Satellite management process functions include telemetry file recording, registration, data compression, automatic file cleanup, processing of S/C operating modes and task scheduling. The task scheduler is an execution unit which function is to issue an ordered list of telecommands.

The telecommands list is generated from SKED (schedule) files and varies depending on the S/C operating mode.

Satellite management process supports up to 6 operating modes:

1. Initialization (INITIALIZATION);
2. Test mode (TEST);
3. Launch and Early Orbit Procedure mode (LEOP);
4. Nominal mode (NOM);
5. FDIR mode;
6. Safe Mode.

First steps, the algorithm go through to initialization of the process and configure satellite parameters. Depending on AIT strap status (removed before flight), the algorithm ether to Test mode or flight one. Test mode is supposed to perform all functional tests within AIT campaign. In case AIT strap removed, the algorithm enters to LEOP mode in which all necessary deployment and configuration activities are performed according to LEOP SKED file. After successful LEOP ending indicated by LEOP flag, the algorithm goes to Nominal Mode where Scheduler executes either telecommands coming from Ground station or command lines which are extracted form NOM SKED file. If an error occurred during command execution or coming telemetry shows fault status of hardware the algorithm goes to FDIR (Fault Detection, Isolation, Recovery) mode which handles and mitigates occurred anomaly in spacecraft. If the algorithm doesn't find appropriate FDIR mode by condition, the last point is to go to Safe mode, which uses minimum hardware to keep satellite in live condition. Result of the satellite management process execution is telecommand packets generation to control satellite regarding on satellite current mode and hardware status. Input and output data format for the process are framed in standard forms, which are defined in [10].

Matrix of possible transitions from mode to mode is shown in Table 2, where CMD means transition by the command and CND – by condition.

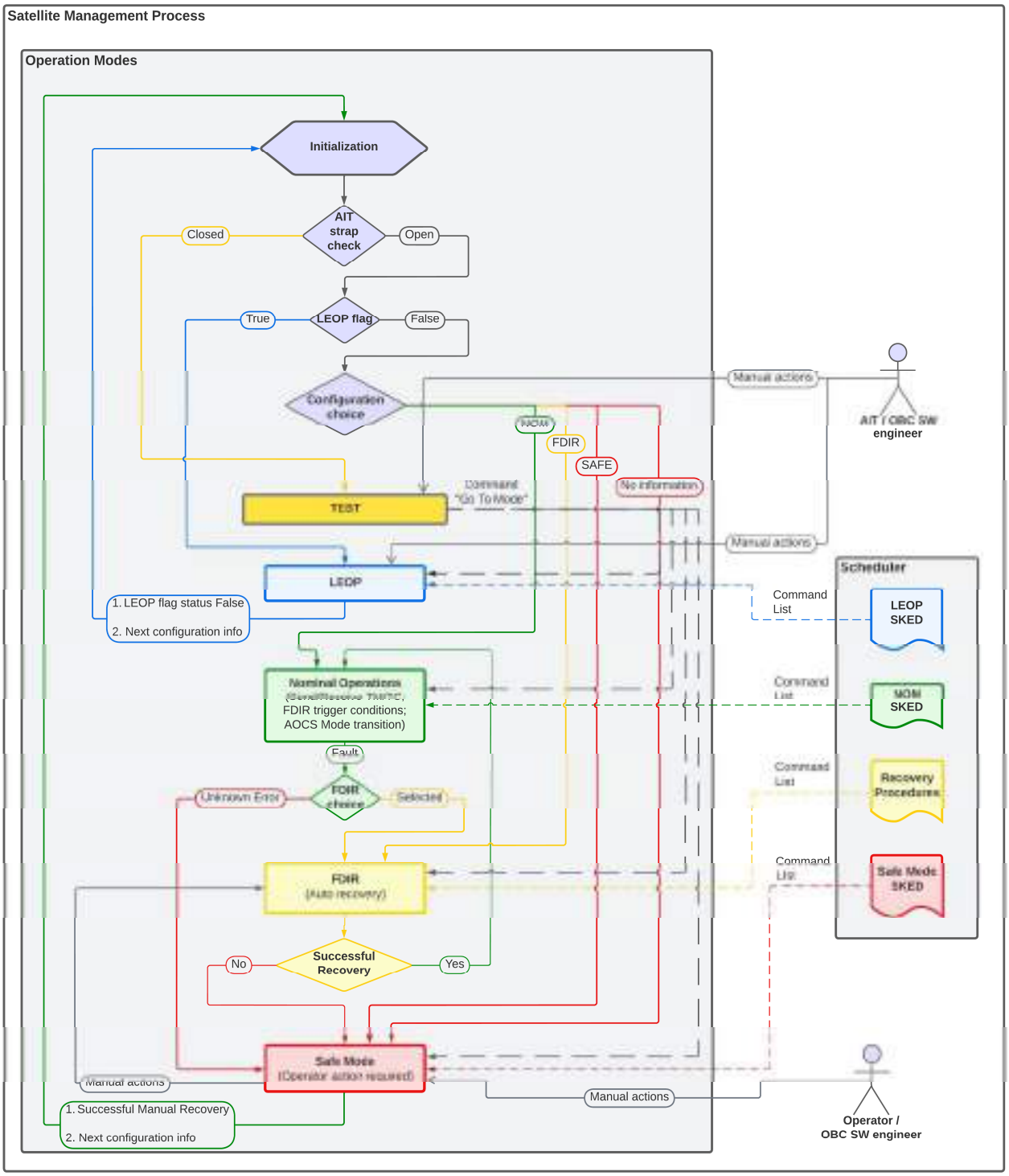

Fig. 5 Algorithm of satellite management process.

Table 2. Modes Transition Variations

From mode	To mode					
	INIT	**TEST**	**LEOP**	**NOM**	**FDIR**	**SAFE**
INIT		CND	CND	CND	CND	CND
TEST			CMD	CMD	CMD	CMD
LEOP	CND/CMD			CND/CMD		CND/CMD
NOM					CND/CMD	CND/CMD
FDIR	CMD			CND		CND /CMD
SAFE	CND CMD			CMD		

3. Circuit design solutions for the development of on-board control system modules

In frame of the development, work was carried out on the formation of circuit solutions at the level of functional blocks and components. As it was shown in the previous sections, the OBCS consists of 3 functional modules physically presented in the form of printed circuit boards:

- Processor module;
- SDR module;
- Interface board.

The enlarged schematic diagram of the processor module is shown in Figure 6. The main component of the processor module is the Zynq ZU9EG chipset - system-on-a-chip from Xilinx.

The Zynq EG series have a quad-core ARM® Cortex-A53 processor with a frequency of up to 1.5 GHz. Combined with the Cortex-R5 dual-core real-time processor, the Mali-400 MP2 GPU and 16 nm FinFET+ programmable logic, the EG devices have an architecture focused on applications in 5G wireless networks, cloud computing, as well as aerospace and defense applications. All the peripherals of the processor module are connected to it, such as: QSPI, DDR4, NAND memory chips, reference generators and an oscillator, as well as voltage converters. An I2C node based on the MSP430 microcontroller is used to monitor the processor module.

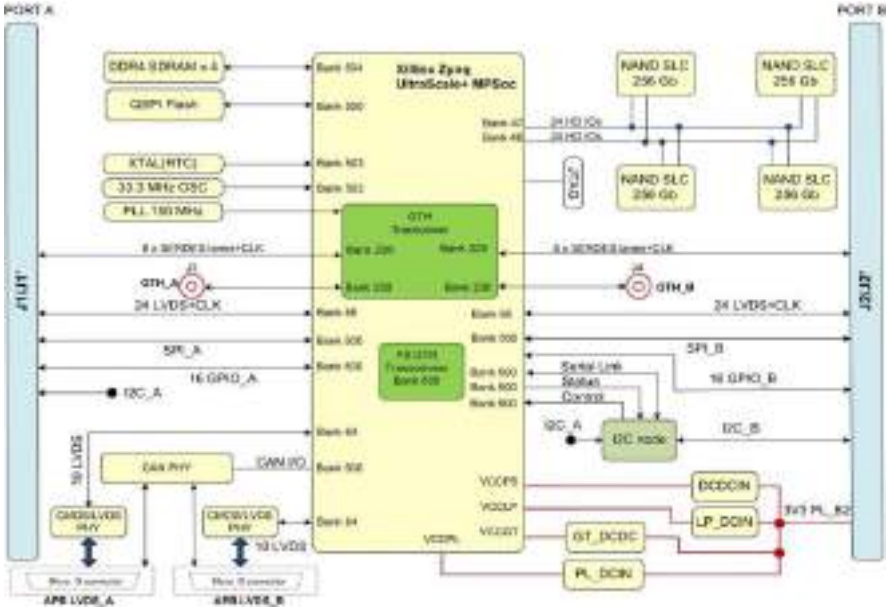

Fig. 6. Block diagram of the OBCS processor module.

Its tasks include collecting telemetry of the state of the processor module, as well as, if problems are detected in the operation of the Zynq system-on-chip, performing module reconfiguration both in automatic mode and in direct command execution mode. One of the features of the OBCS being developed is the availability of a high-speed data transmission channel to the ground station based on SDR. At the same time,

Zynq resources are used for demodulation, mixer functions and signal filtering, which significantly unloads the hardware design of the OBCS as a whole, and only direct conversion to analog form and back to digital is performed on the SDR module. The functional schematic diagram of the SDR module is shown in Figure 7.

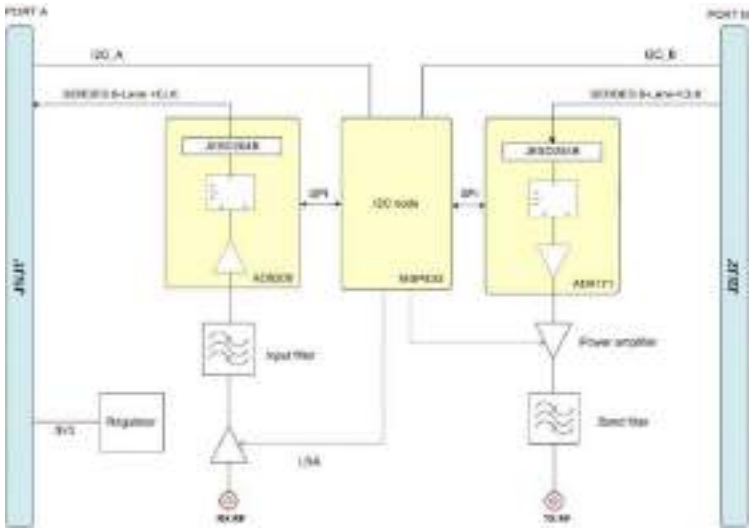

Fig.7. Block diagram of the SDR module of the OBCS.

The board uses high-performance analog-to-digital and digital-to-analog converter chips providing up 6 GSPS sampling rate. For receive path a signal is pre-amplified along the receiving path to the desired signal level and fed to the input filter to allocate the operating frequency bands, then the signal is fed directly to the analog-to-digital converter, which converts to a digital stream via 8 LVDS lines. For the transmitting part, conversions are performed in reverse order. The design feature of the considered OBCS is its application both on the CUBESAT platform and on a small satellite platform for mostly used configurations. Figure 8 shows an enlarged schematic diagram of the interface board, which provides this capability. The external connectors may not be soldered with the CUBESAT configuration, and the interface with the rest of the modules is provided via the PC/104 pad.

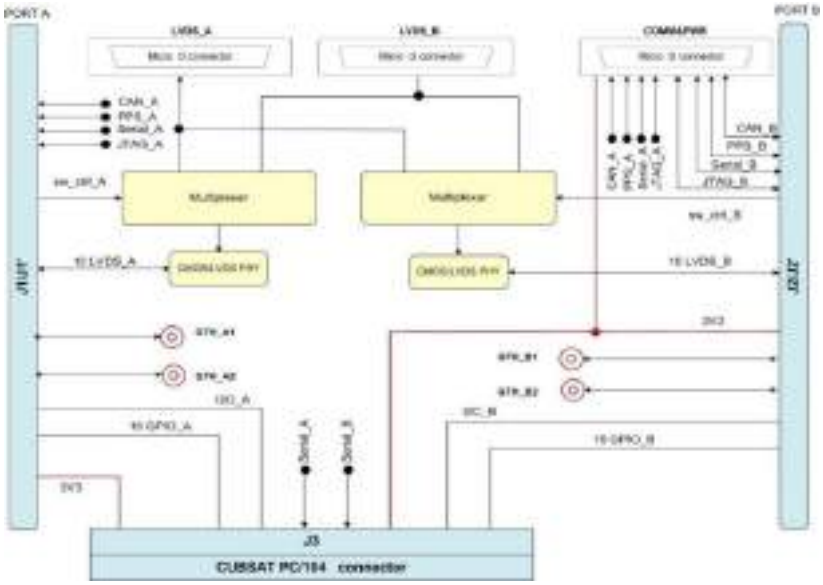

Fig. 8. Block diagram of the OBCS interface board.

.

Conclusion

This development will dramatically simplify designing a nanosatellite architecture by using modular flexible structure and integrated solution which effectively implements several functions based on modern technologies (SoC, SDR) allowing in short terms and low prices to build small satellite systems.

As part of the research work, an analysis was carried out in the field of the OBCS design methodology, the characteristics of existing models of OBCS for nanosatellites and CUBESAT platforms were considered. The variety of models available on the markets indicates the trend of rapid growth of this segment against the background of great interest in projects based on nanosatellites and their prospects for application in most missions. As a result of the analysis, it can be concluded that the proposed development is relevant. The key difference from similar OBCS will be multifunctionality, adaptive integrability with various payload and the use of SDR technology for high-speed data transmission.

Work has also been carried out on the development of OBCS electronics circuitry in the form of block circuit diagrams, which are the basis for further development of detailed design of printed circuit boards.

Acknowledgments (or Funding)

This research is funded by the Aerospace Committee of the Ministry of Digital Development, Innovations and Aerospace Industry of the Republic of Kazakhstan (BR109018/0221) "Development and testing of domestic key technologies for the creation and control of spacecraft".

REFERENCES

1 Arseno D., Edwar E., Harfian A.R., Salsabila J.N. Characterization of On Board Data Handling (OBDH) Subsystem. *Proceeding of the IEEE 13th Intern. Conf. on Telecommunication Systems, Services, and Applications (TSSA)*, 2019. doi: 10.1109/TSSA48701.2019.8985466

2 Sarsenbayev Y., Mussina A., Ismailov U., Bychkov A. Spacecraft onboard control system. *Detailed information: Utility model № 6912*. 2022, p.1. Available at: gosreestr.kazpatent.kz/Utilitymodel/Details?docNumber=351783.

3 ESA KazSTSAT (Kazakh Science and Technology Satellite), 2022. Available at: www.eoportal.org/satellite-missions/kazstsat#list-of-payloads-on-the-spaceflight-sso-a-rideshare-mission.

4 Omran E.A., Murtada W.A., Serageldin A. Spacecraft on-board real time software architecture for fault detection and identification. *Proceeding of the 12th Intern. Conf. on Computer Engineering and Systems (ICCES)*, 2017. doi:10.1109/ICCES.2017.8275379

5 Ten V., Oralmagambetov B., Murushkin S., Bekembayev A. Absolute passive mode pecularities and applications for LEO missions. *Proceeding of the 67th I Intern. Astronautical Congress*, 2016. doi: IAC-16.D1.IP.5.x35477. Available at: www.iafastro.directory/iac/archive/browse/IAC-16/D1/IP/35477/

6 Verdict Media Limited. *KazEOSat-1 Earth Observation Satellite.* 2022. Available at: www.aerospace-technology.com/projects/kazeosat-1-earth-observation-satellite.

7 Wenker R., Legendre C., Ferragutoz M. On-board software architecture in MTG satellite. *Proceeding of the IEEE Intern.Workshop on Metrology for AeroSpac*e, 2017. doi:10.1109/MetroAeroSpace.2017.7999588

8 Tipaldi M., Ferraguto M., Ogando T., Camatto G., Wittrock T., Bruenjes B., Glielmo L. Spacecraft autonomy and reliability in MTG satellite via On-board Control Procedures. *Proceeding of the IEEE Intern. Workshop on* Metrology for Aerospace, 2015, pp. 155 – 159. doi:10.1109/MetroAeroSpace.2015.7180645

9 Miranda DJF, Ferreira M, Kucinskis F, McComas D. A Comparative Survey on Flight Software Frameworks for 'New Space' Nanosatellite Missions. *J Aerosp Technol Manag*, 2019, V.11: e4619. Available at www.doi.org/10.5028/jatm.v11.1081

10 European Cooperation for Space Standardization Ground systems and operations - telemetry and tele-command packet utilization. Euro pean Cooperation for Space Standardization. Available at: ecss.nl/standard/ecss-e-st-70-41c-space-engineering-telemetry-and-telecommand-packet-utilization-15-april-016/. ECSS-E-70-41C, 2016.

11 ISO. Road vehicles - Controller area network (CAN). Part 3: Low-speed, fault-tolerant, medium-dependent interface. Available at: www.iso.org/standard/36055.html. ISO 11898-3, 2006.

Article accepted for publication 31.10.2022

DOI 10.31489/2022No4/67-72
UDC 531; 517.96

INVESTIGATION OF THE STRESS STATE OF MINE WORKINGS USING METHODS OF DEFORMABLE SOLID MECHANICS

Shaikhova G.S.[1], Belomestny D.V.[2], Kopbalina K.B.[1]*

[1] A. Saginov Karaganda Technical University, Karaganda, Kazakhstan, kopbalina82@mail.ru
[2] University Duisburg-Essen, Germany, denis.belomestny@uni-due.de

The assessment of the reliability of a mining and technological scheme, taking into account the stress state of mine workings, depends on a combination of mining and geological, technical and technological factors. The article demonstrates the creation of a model of a rock mass and a scheme for calculating the stress state based on modern methods of mechanics of a deformable solid body.The object of study is a single mine working of great length, passed through the rock parallel to the strike of the coal seam (field drift) and located in the zone of influence of the support pressure. Due to the fact that the field drift is laid in the soil of the formation, which is a layered stratum in the zone of influence of clearing operations, the predominant load is the bearing pressure on the formation. The areas of application of the methods of complex potentials of integral equations and their combinations in solving applied problems are determined. The data of mine (field) measurements and observations, laboratory experiments and their generalizations are taken into account both when setting tasks and assigning boundary conditions, and when checking the results obtained. The mixed problem of the theory of elasticity about the contact stress on half-strips with varying along the longitudinal axis was solved; moving away from the ends, deformative properties, when these half-strips are clamped with friction between the layered half-planes.

Keywords: *massif, stresses, model, coal seam, integration nodes, method of boundary integral equations, pressure.*

Introduction

The aim of our study is: the selection of adequate models of such media in the form of a layered half-plane, anisotropic plane and half-strips between compressing heterogeneous half-planes, solving problems of the theory of elasticity for a layered half-plane with a hole and an anisotropic plane with two mutually affecting openings under given boundary conditions in the stresses; determination of contact stresses for half strips between clamped layered half-planes; establishing areas for the effective application of the methods of complex potentials of integral equations and their combinations in solving the applied problems. The following tasks are specifically set:

- to justify the reduction of the problem of the tensity of the field drift in the zone of influence of coal seam mining by long columns in the fall to the first main plane problem of the theory of elasticity for a layered half-plane with a hole and a biconnected anisotropic plane;
- to determine the tensity of the layered half-plane near the free circular hole with unbalanced loads at the upper boundary;
- to assess the distribution of contact tension on half-strips, divorced along the longitudinal axis and compressed by layered half-planes;
- to find the stress state of the anisotropic plane near a free hole of arbitrary shape at given voltages at infinity and on the contour of an elongated oblong hole;
-to perform multivariate calculations, analyze them and formulate practical recommendations.

The research methodology provides for the mandatory use of data from mine (full-scale) measurements and observations, laboratory experiments and their generalizations both in the formulation of tasks and the assignment of boundary conditions, and in verifying the results obtained during the solution. When solving boundary-value problems, both analytical and numerical methods of mechanics of a deformable solid are involved.

.

1. Research methodology

The correct choice of the method of maintaining the operational drifts located near the coal seam in working condition cannot be achieved without knowledge of the intense rock mass. A method for calculating stresses in the vicinity of a field preparatory drift based on the method of boundary integral equations for the theory of elasticity of an anisotropic body, taking into account the specifics of coal seam mining, is proposed. A diagram of the mutual arrangement of the grading and field drift is shown in Fig. 1. The rock mass is represented by an elastic homogeneous transversely isotropic body. The plane of isotropy of the body coincides with the bedding plane of the rocks, which makes an angle φ with the horizontal plane. We believe that in the vertical plane across the strike of the isotropy plane Oxy, the condition of plane deformation is fulfilled. The stresses in the pristine mass are homogeneous ($\sigma_x^0 = const,\ \sigma_y^0 = const, \tau_{xy}^0 = const$). The drift has a circular (R-radius) cross-section, the treatment output is rectangular (h-height, L - length).

Consider mining a coal seam by dip. Line KK' models the face moving along the formation. In this case, point K advances as coal are extracted from point A in a straight line DAE to the left (see Fig. 1). In real conditions, as the face moves in the vicinity of the mine working site, inelastic deformations develop, the roof settles down until it collapses completely [1-3]. So, in fig. 2 shows the pressure zone according to S.G. Avershin. It can be assumed that, over time, the destroyed and completely subsided rock masses establish stresses that coincide with the field of natural stresses of the rock mass (region $AA'B'B$, Fig. 2b). In the area $BB'C'C$ of voltage in the settled rocks have not been established, the area corresponds to the bottom hole zone, where coal is broken, people and mechanisms work.

The complexity of mathematical modeling of the coal seam mining process, even in the two-dimensional case, is due, first of all, to the presence of gaps of developing inelastic deformations. Direct consideration of these zones in the formulation of the problems of mechanics of a deformable solid leads to difficulties that are currently resolved only in some cases. Therefore, for simplicity of calculations, it makes sense to consider the problem in an elastic setting, taking into account the zones of destroyed rocks with the help of additional forces that act along the boundary of the mine. Based on the foregoing, the problem of determining the stress state of a rock mass can be described as a flat problem of the theory of elasticity of an anisotropic body. At the same time, we believe that, starting from a certain distance from the bottom (points C and C'), the forces increasing according to the linear law (on the lines CB and $C'B'$, see Figure 1) act on the boundary of the mine working. The forces increase until they reach a value characterizing the stresses in the untouched massif and then remain unchanged (on the lines $BA, AA', A'B'$). The type of external forces characterizing the stresses in the untouched array is chosen from the following considerations. For simplicity, let us consider a single hole in an anisotropic plane loaded at “infinity” (Figure 3).

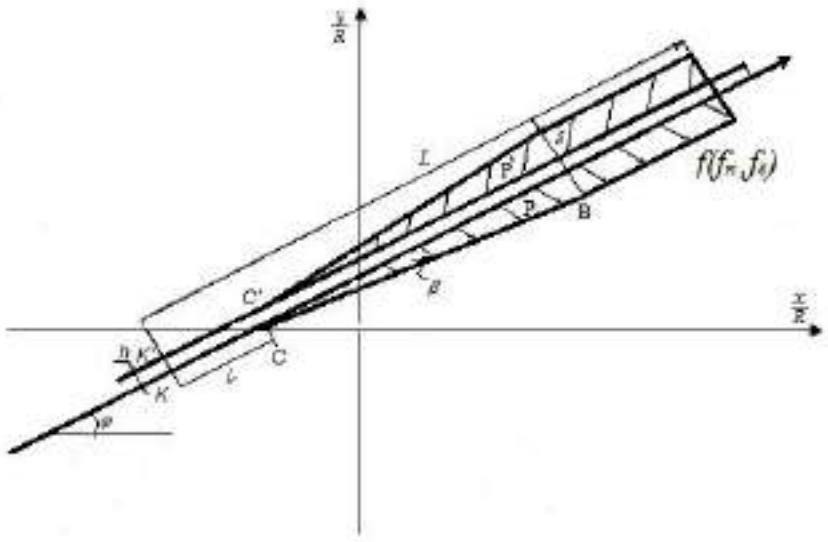

Fig.1. Scheme of the relative location of the treatment plant and drift.

The stress state of a plane is determined by the boundary element method [4,12]. In this case, we approximate the counter holes by a closed polygonal line consisting of line segments (elements). The resolving system of relative constant for each element of fictitious loads for the first main task of the theory of elasticity has the form.

$$\left.\begin{aligned}\sum_{j=1}^{K}\left(a_{nij}g_{nj}+a_{lij}g_{lj}\right)&=-\sigma_{ni}^{0}-f_{ni},\\ \sum_{j=1}^{K}\left(b_{nij}g_{nj}+b_{lij}g_{lj}\right)&=-\tau_{nli}^{0}-f_{li}\end{aligned}\right\},\quad (i=1,2,...,K) \tag{1}$$

here g_{nj} and g_{lj} are the intensities of the friction loads; $a_{nij}, a_{lij}, b_{nij}, b_{lij}$ - system coefficients – are determined according to well- known formulas [5-7,11]; and σ_{ni}^{0}, and τ_{nli}^{0} voltage in a plane without a hole, converted accordingly for the i - element; f_{ni} and f_{li} respectively, the normal and tangential forces acting on the i - element; K - the number of approximating elements $(ij=1,2,...,K)$.

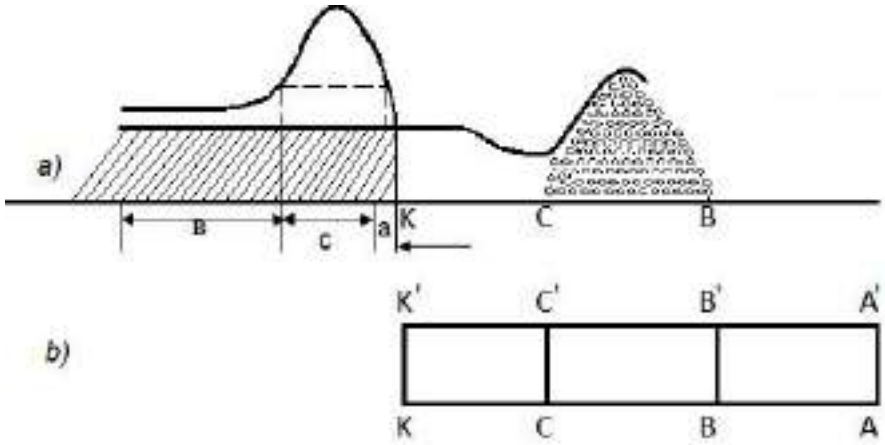

ig. 2. Characteristic areas in the worked – out space and their schematization.

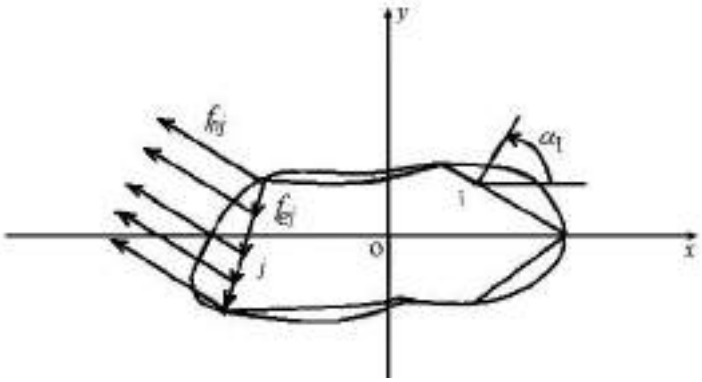

Fig. 3. Circuit approximation by broken lines, global and local coordinate systems.

Obviously, it is always possible to choose the intensity of efforts f_{ni} and f_{li} so that the vector of free terms, of system (1) will be zero. In this case $g_{nj}=g_{kj}=0,(j=1,2,...,K)$, the stresses in the plane with the hole will note differ from the stresses in the flatness without a hole. For example, the voltage at some point in the plane is

$$\sigma_x=\sigma_x^0+\sum_{j=1}^{K}\left(c_{xj}g_{nj}+d_{xj}g_{lj}\right)=\sigma_x^0 \tag{2}$$

.

Thus, making efforts

$$\left.\begin{aligned} f_{ni} &= -\sigma_{ni}^{0} = -\frac{\sigma_x^0+\sigma_y^0}{2} - \frac{\sigma_x^0-\sigma_y^0}{2}\cos 2\alpha_i - \tau_{xy}^0 \sin 2\alpha_i, \\ f_{li} &= -\tau_{nli}^{0} = \frac{\sigma_x^0-\sigma_y^0}{2}\sin 2\alpha_i - \tau_{xy}^0 \cos 2\alpha_i \end{aligned}\right\}, (i=1,2,...,K) \qquad (3)$$

Along the contour of the hole (see Figure 3), we achieve that the stresses in the plane loaded with "infinity" with the loaded hole do not differ from the stresses in the loaded plane without the hole. As you can see, the intensity and direction of external forces depends on the stresses in the plane without a hole and the orientation of the element (α_i - is the angle between the normal to the element directed to the region of the elastic body and the axis OX) [8-10].

Based on these considerations, we believe that the external forces acting on formulas (3) act on the elements making up the lines $BA, AA', A'B'$. On the lines CB and $C'B'$ the forces vary linearly, increasing from the nucleon (at points C and C') to the quantities characterizing the loads on the lines BA and $A'B'$. Note that expressions (3) are simplified for the hydrostatic distribution in an untouched massif $\left(\sigma_x^0=\sigma_y^0, \tau_{xy}^0=0\right)$. In this case $f_{li}=0, (i=1,2,...,K)$, and external forces are determined only by the normal pressure equal σ_y^0 to the lines $BA, Aa', A'B'$, and linearly changing on the lines CB and $C'B'$.

Numerical results were obtained for three different lengths of the treatment plant ($L=12R$, $L=24R$, $L=36R$). As a source for transversely isotropic sandy shale [11-13]. The angle of inclination of the plane of isotropy is $\varphi=30^0$. The hydrostatic stress distribution in the pristine massif is accepted. The sizes $l=6R$, $h=R$, as well as the coordinates of the point A $(X_0 = 20.8R; Y_0 = 15R)$ for all options are constant. A linear increase in external forces was carried out on the segments $CB=C'B'=20R$, while it was set $tg\beta = 0.05$ (see figure 1). For $L=12R$ and $L=24R$ external forces do not reach their upper limit, but increase up to the points A and A', which coincide in these cases with the points B and B'. When $l=6R$ and $tg\beta = 0.05$ for $L=12R$ on the line Aa', these efforts are equal $0.3\sigma_y^0$, but for $L=24R$, equal $0.9\sigma_y^0$. In figure 1 shows the locations of the feces for different $L: KK'$ for $L=36R$, SS' for $L=24R, PP'$ for $L=12R$.

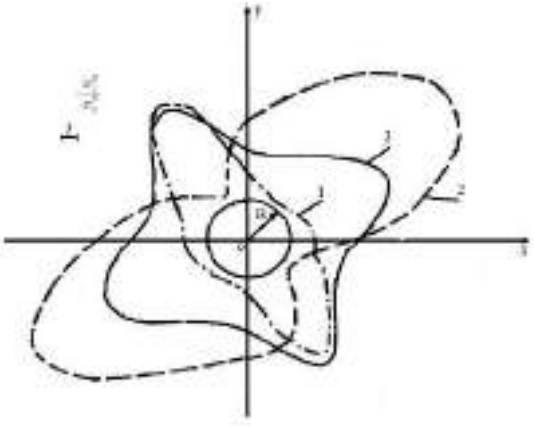

Fig.4. Plots of normal stresses on the contour of a field preparatory drift.

At $L=12R$ (curve 1), the stresses on the circuit practically with the stresses for a single circular output, i.e. the effect of treatment work on the field drift remains insignificant. Because the face is still far enough away. The stress diagram changes significantly with $L=24R$ (curve 2): the asymmetry of the stress distribution is visible and increase in the maximum stresses is noticeable. When $L=36R$ (curve 3), the

maximum stresses decrease compared with the previous case and their maxima rotate approximately 90° relative to point 0.

2. Results and discussion

The calculation results indicate a significant effect of the net generation on stresses in the vicinity of the drift, the nature of the stress distribution varies depending on the distance and position of the bottom hole production, relative to the field drift, the maximum stresses on the drift circuit are achieved when the working face is located above the field drift, (at $L = 24R$).

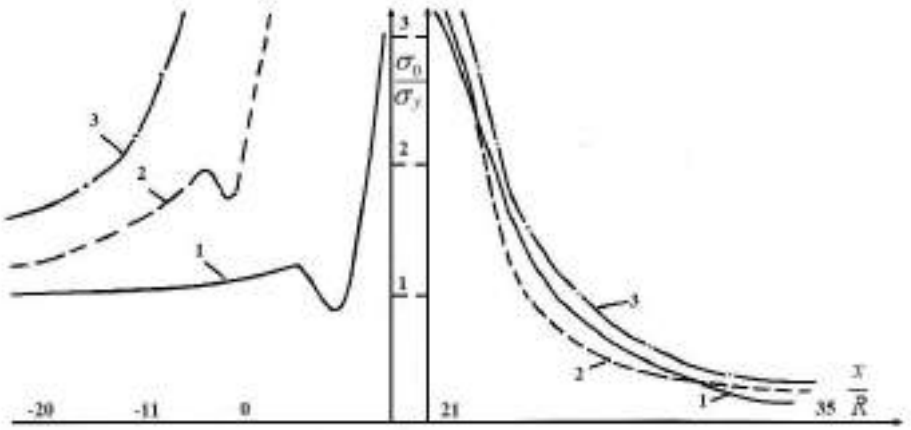

Fig. 5. Distribution of normal stresses on the lines

Figure 5 shows plots of normal voltages $\sigma_n \frac{\sigma_0}{\sigma_y}$ on the lines AE and AD for various calculation options. As we see, near the drift on the straight line AE for $L = 12R$ (curve 1) and $L = 24R$ (curve 2), the nature of the stress distribution differs from that of the straight line for $L = 36R$ (curve 3).

Conclusion

The obtained data indicate the influence of the drift on the mechanism of transfer of the support pressure before the bottom hole to the formation soil. The scheme for calculating the stress state of this mine in the dynamics of the manifestation of the support pressure on the seam takes into account the presence of heterogeneous layered soil of the coal seam, where the field drift is laid.

It contains the results of a study of the correct formulation of the problem of support pressure on an inclined-buried buried coal seam near the treatment space. It is advisable to use these methods, and it is necessary to link them with a specific system for developing coal seams and methods for preparing the mine field. Some conclusions on the choice of the location of field drifts and their content from the point of view of the "stress state" factor are recommended for implementation in mines.

Thus, the developed model of a drift embedded in a layered medium, in the zone of influence of the processing space, allows us to fully study the picture of the stress-strain state of rocks around the drift up to the processing output.

REFERENCES

1 Aitaliev Sh.M., Kayupov M.A. The method of boundary elements in plane problems of the concentration of elastic stresses in an anisotropic body. *In mechanics of tectonic processes,* 1983, p. 133-143. [in Russian]

2 Aitaliev Sh.M., Adilbekov N.A., Kayupov M.A. The investigation by the GIU method of the stressed state of a field drift during an underwork. *Izv. KazSSR, a series of physical. Math.,* 1983, No. 5, p. 78. [in Russian]

3 Aitaliev Sh.M., Adilbekov N.A. The solution of the elastic problem for a doubly connected anisotropic plane by the GNU method and calculation of the influence of the mine working on the field drift. *Differential equation and their applications,* 1994, pp. 96 – 105. [in Russian]

4 Adilbekov N.A., Shaikhova G.S., Zhurov V.V., Shegebayeva G.E. The numerical solution of one system of Fredgolm integral equations of the third kind in the problem of support pressure near the mine. *Science News of Kazakhstan*, 2019, No. 3, pp. 98 – 105.

.

5 Issagulov A.Z , Belomestny D., Shaiкhova G.S., et al. Functions of atoms radial distribution and pair potential of some semiconductors melts. *The Bulletin of the National Academy of Sciences of the Republic of Kazakhstan, 2019,* Vol. 4, No.380, pp.6-14. doi:10.32014/2019.2518-1467.86

6 Kavlakan M.V., Mikhailov A. M. On the distribution of pressure on the formation when the horizontal development. *Physical and technical problems of mineral development*, *Kazakhstan,* 1977, No. 5, pp. 48-53.

7 Kavlakan M.V. About one method of solving spatial problems about the reference pressure. *Physical and technical problems of mining*, 1981, No. 6, p. 17-27.

8 Shaikhova G.S. Explanation of the Cluster Structures Melting Mechanism And their influence on the molten state's physical and chemical nature. *Complex Use of Mineral Resources*, 2021, No.1(313), pp. 62 – 68. doi:10.31643/2021/6445.08

9 Suleimenov N.V, Shapalov Sh.K, Khodzhaev R.R, Shaikhova G.S. Computerized Analytical System for Assessing Fire and Environmental Safety of Mines in the Karaganda Coal Basin. *Intern. Journal of Engineering Research and Technology*, 2020, Vol.13, No. 6, pp. 1133-1136.

10 Akhmetov K.M., Shaikhova G.S, Zhurov V.V., et al Mathematical model of coal self-heating in a stack. *Complex Use of Mineral Resources,* 2021, No.3 (313), pp. 90 - 96. https://doi.org/10.31643 /2021/6445.32

11 Kazhikenova S.Sh., Shaltakov S.N., Belomestny D., Shaikhova G.S. Finite difference method implementation for Numerical integration hydrodynamic equations melts. *Eurasian Physical Technical Journal*, 2020, Vol. 17, No.1(33), pp. 50 – 56. doi: 10.31489/2020No1/145-150

12 Bayer C., Belomestny D., Redmann M., Riedel S., Schoenmakers J. Solving linear parabolic rough partial differential equations. *Journal of Mathematical Analysis and Applicatio*ns, 2020, No. 490(1), pp. 124236. doi:10.48550/arXiv.1803.09488

13 Belomestny D., Schoenmakers J. *Multilevel Methods.* Palgrave Macmillan, London, 2018, Vol. 19, No.1(31), pp. 55-75.

Article accepted for publication 04.11.2022

DOI 10.31489/2022No4/73-77

UDC 535.3

TRANSIENT ABSORPTION OF GOLD NANOPARTICLES OF VARIOUS DIAMETERS

Ibrayev N.Kh., Seliverstova E.V., Kanapina A.E.

Institute of Molecular Nanophotonics, Buketov Karaganda University, Karaganda, Kazakhstan, niazibrayev@mail.ru

The transient absorption of gold nanoparticles with an average diameter of 13±5 and 48±16 nm upon photoexcitation by nanosecond laser pulses has been studied. It was shown that the maximum of stationary absorption exhibits as a wide structureless band with a maximum at about 520–540 nm. The transient absorption band of gold nanoparticles with a maximum at about 430 nm has a fine structure with a frequency of maxima of 6–8 nm and it does not depend on the size of the nanoparticles. The absorption duration decreases with a decrease in the average size of nanoparticles. The lifetime of transient absorption is equal to 23±2 and 19.5±2 ns for large and small particles, respectively. The nanosecond lifetime of the transient absorption of Au nanoparticles is the result of a prolonged relaxation process in the "interface of Au nanoparticle–solvent molecule" system as a manifestation of hindered heat exchange with the environment.

Keywords: gold nanoparticles, plasmon, size, transient absorption, optical properties.

Introduction

The phenomenon of localized plasmon resonance is the attractive research topic in the last few decades due to the possibilities of its practical application. Plasmon nanoparticles of noble metal increase the efficiency of various optical and optoelectronic phenomena, including Raman scattering and photocatalysis, and also improve the performance of organic light emitting diodes and photovoltaic devices [1–5].

Methods of flash photolysis are used to study the dynamics of electronic excitation in plasmon nanoparticles (NPs) of metals. This method is very sensitive, it allows detecting the single NPs and studying the dynamics of fast processes.

In this method a perturbation of the electron density of metal NPs, leading to the appearance of a plasmon resonance (PR), occurs upon simultaneous photoexcitation by laser pulses and probing beam. The PR lifetime is determined by the electron dephasing process with a typical time constant of 10–100 fs. This process is the first stage in the complex dynamics of electron relaxation in metal NPs [6, 7]. In the time range from 100 fs to 1 ps, the process of electron-electron scattering occurs, which leads to the equalization of the electron temperature inside the metal NPs. Further, in the range of 1–10 ps, electron-phonon scattering occurs, which stabilizes the temperature of the electrons and the surrounding lattice. The electron-phonon relaxation decay time depends on the growth in the electron temperature, which is related to the excitation pulse power and increases linearly with the pump energy [7]. This mechanism can be used for nanoscale heat transfer from metal NPs to biological objects for photothermal therapy, biomedical imaging, etc. [8]. Phonon-phonon scattering (>100 ps) releases heat into the environment and it is the slowest process.

However, there are practically no works devoted to the study of the transient absorption of Au NPs upon nanosecond photoexcitation. The exception is the work of [9], where the transient absorption of Ag NPs of various sizes was studied during photoexcitation by nanosecond laser pulses. The dependence of the intensity and lifetime of transient absorption on the average size of the NPs, their concentration and pump energy was investigated. It has been shown that in a delayed heterophase heat exchange at the boundary of the "particle-medium" interface, the kinetics is "prolonged" up to times of the order of several tens of nanoseconds.

In this work, the transient absorption of gold NPs of various diameters in ethanol solutions was investigated. Gold NPs, due to the position of the plasmon resonance band in the green region, are more attractive for usage in biophysical and biomedical applications, for example in photodynamic and photothermal therapy [10-12], singlet oxygen generation [13, 14], etc.

1. Experiment

Gold NPs were obtained in solution by ablation of a 30 nm thick gold film. 99.999% gold was deposited on the surface of the glass substrate by magnetron sputtering method with Q150RES (Quorum Technologies Ltd.). Ablation was performed by Nd:YAG laser with λ_{gen}=532 nm, pulse duration of τ=8 ns according to the method, described in [15]. To change the average diameter of the received NPs, the laser radiation energy was varied from 9.5 to 13.5 mJ. During ablation, the laser beam was focused on a target immersed in ethanol using a collecting lens. The diameter of the laser spot on the target was equal to 0.1 cm. The volume of ethanol in a glass with Au film was equal to 3 mL. The ablation time was equal to 15 minutes.

The absorption spectra of Au NPs in ethanol were measured with Cary–300 spectrophotometer (Agilent). The spectra and kinetics of transient absorption were studied by pulsed photolysis method using the LP-980 spectrometer (Edinburgh Instr.) upon excitation with the second harmonic of Nd:YAG laser (LQ215, SolarLS) with λ_{gen}=532 nm and pulse duration of τ=7 ns. To measure the kinetics of transient absorption, the solution was placed in a quartz cell with an optical path length of 10 mm. The kinetics of transient absorption was recorded in the time range up to 4 μs. The plotting of the transient absorption spectra was performed by automatically scanning the kinetics with a step of $\Delta\lambda$=2 nm in the required wavelength range, followed by data slicing using L900-software (Edinburgh Instr.). The processing of individual absorption kinetics was also carried out using this software.

2. Results and discussions

Dynamic light scattering measurements (Zetasizer S90, Malvern) showed that the average diameter of the obtained Au NPs was equal to 13±5 and 48±16 nm (Fig. 1). The concentration of Ag NPs in the resulting solution was equal to $C_{Au}=6\cdot10^{-10}$ and $2\cdot10^{-10}$ mol/L, respectively. For further measurements, solutions of Au NPs with the same concentration were prepared. Images, registered in transmission mode with Mira 3LMU (Tescan) microscope have shown that the prepared NPs are spherical.

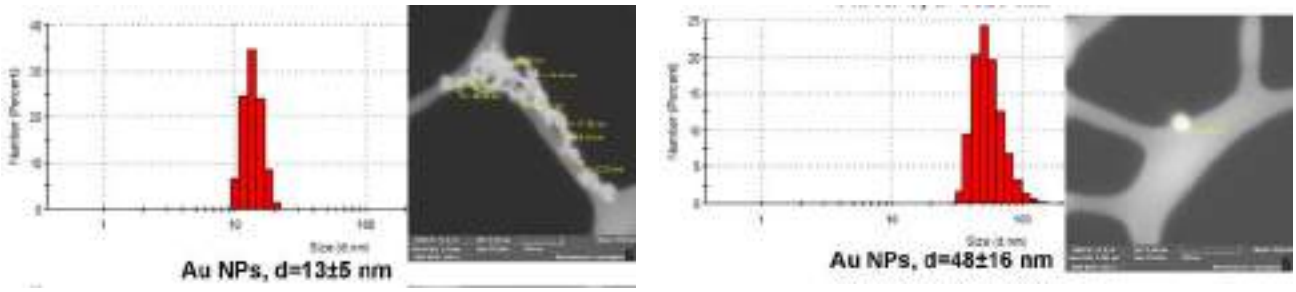

a) b)

Fig.1. Size distribution and TEM images of Au NPs with various diameter.

The measured stationary absorption spectra of gold NPs in ethanol are shown in Fig. 2. It can be seen that for both types of NPs the spectrum exhibits as a wide structureless band in the region from 450 to 800 nm with a maximum at about 530 nm. Also in the spectrum appears an absorption band at about 350 nm, which refers to the absorption of d-electrons of Au [6]. The spectra of both small and large NPs do not change their shape. However, with an increase in the average diameter of Au NPs, a bathochromic shift of the absorption band maximum from 526 to 540 nm was observed. The broadening of the 48±16 nm absorption band of Au NPs is also noticeable, which is associated with a greater dispersity in size of the prepared NPs.

The observed bathochromic shift of the absorption band of larger Au NPs is the result of the displacement of the boundary electrons relative to the positive ionic lattice during the transmission of the incident light through the metal NPs [16]. This results in a net charge difference at the "NP – environment" interface. In turn, this generates a Coulomb restoring force that tends to bring the system to its equilibrium state and leads to the appearance of the surface plasmon oscillations [17].

It was shown in the Mie theory [18] that when the particle size is much smaller than the wavelength of the incident light ($d<<\lambda$), then the α polarizability of a metal NP is determined by the Clausius-Mossotti relation [16]:

$$\alpha = 3\varepsilon_0 V\left(\frac{\varepsilon-\varepsilon_m}{\varepsilon+2\varepsilon_m}\right) \quad ,$$

where ε is the permittivity of vacuum, ε_m is the dielectric constant of surrounding medium, ε is the dielectric function of the metallic NPs, V is the volume of spherical NP.

Thus, it can be seen that the NP polarizability of NP is directly depends on the size of NPs and on its permittivity. The imaginary part of the permittivity, in turn, determines the absorption of light in a metal NPs [19].

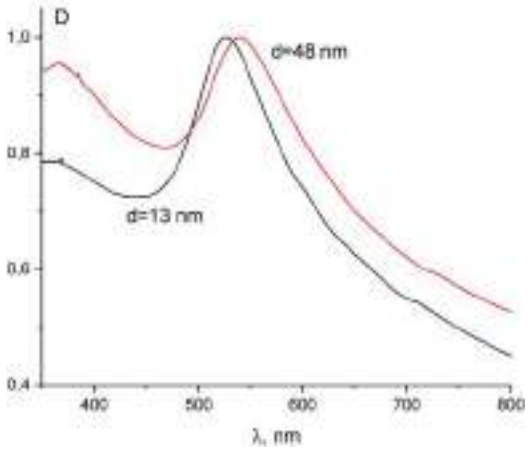

Fig.2. Stationary absorption spectra of Au NPs of various diameters.

The long-wavelength shift of the NP absorption band is associated with the dependence of the contribution of free electrons to the permittivity. The damping of the electromagnetic field, which occurs as a result of the depolarization of the light field on the surface of the particle, leads to a weakening of the Coulomb restoring force on the electron cloud. Therefore, the frequency required to excite surface plasmon oscillations will be decreased [16].

The transient absorption spectra of Au NPs with d=48±16 nm are recorded in the region of 370–570 nm (Fig. 3). In this case, the positive part of the spectrum is located in the region of 370–500 nm with a maximum at about 420–450 nm for Au NPs. The spectrum exhibits optical density oscillations both in the positive and negative parts of the absorption curve. The frequency of the maxima is 6–8 nm. The band in the negative part of the spectrum with a maximum at about 520–530 nm coincides with the main absorption band and it is the result of a change in the population of the ground state. The measurements showed that with an increase in the delay of recording time, the structure of the transient absorption spectrum of Au NPs is retained and it practically was not changed.

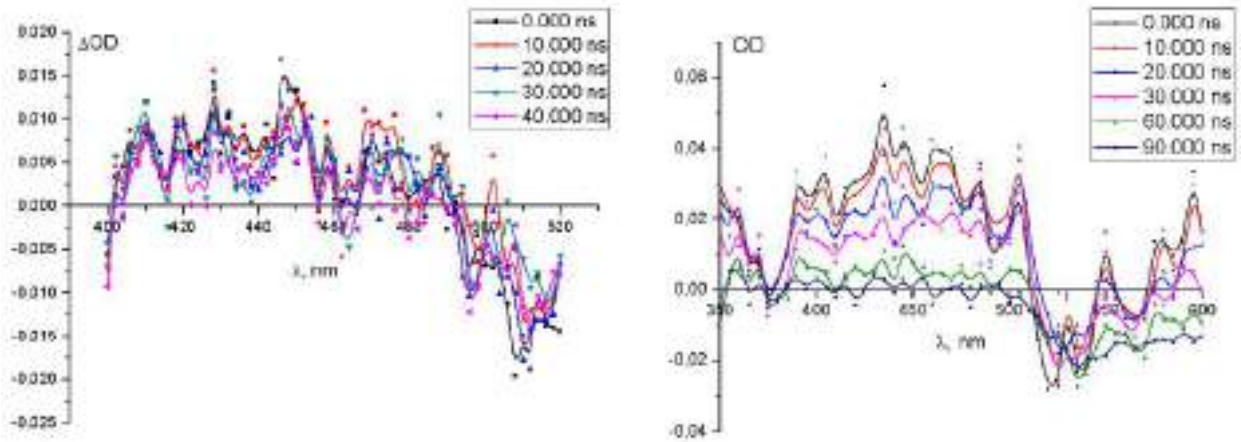

Au NPs, d=13±5 nm

Au NPs, d=48±16 nm

Fig.3. Transient absorption spectra of Au NPs with various diameter at different times of registration, λ_{exc}=532 nm, Δ=2 nm.

The intensity of the transient absorption of NPs of larger diameter is higher. A decrease in the particle diameter does not change the shape of the transient absorption band, while the fine structure of the spectrum is also retained. At a recording time of more than 60 ns, the absorption signal is almost completely decayed. The transient absorption kinetics of 48±16 nm Au NPs recorded at different wavelengths are shown in Fig. 4.

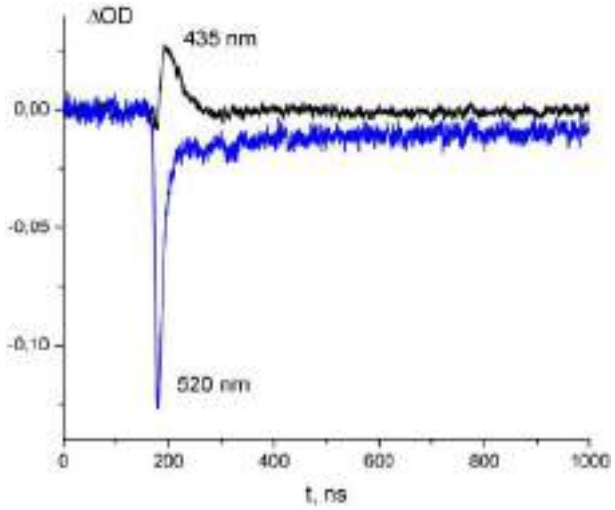

Fig.4. Decay kinetics of the transient absorption of Au NPs (d=48±16 nm), λ_{exc}=532 nm, registered at 435 and 520 nm.

As can be seen from the figure, the absorption kinetics of Au NPs at 435 and 520 nm are different. The kinetics at 435 nm can be described by a monoexponential equation. The estimated decay lifetime was equal to 23±2 ns. The kinetics at 520 nm is better approximated by the bi-exponential decay law. The estimated lifetimes were equal to 21±2 ns and 1.25±0.2 μs. The duration of transient absorption of Au NPs of smaller diameter was equal to 19.5±2 ns for λ_{reg}=435 nm. For 520 nm, the duration of absorption was equal to 5.5±2 ns.

Thus, it can be seen that a decrease in the average diameter of Au NPs leads to a decrease in the duration of transient absorption. Nevertheless, the lifetime of transient absorption of Au NPs lies in the nanosecond range, which is uncharacteristic for this process.

It is known that the duration of the transient absorption kinetics is determined by the relaxation time of an ensemble of excited electrons formed under the action of a laser pulse [6]. The relaxation of excited electrons is a complex process that occurs in several stages. It was shown in [9] that nanosecond times are the result of interface phonon energy exchange, which is extended in time up to nanoseconds and more. This does not allow the electrons of a metal NP heated by a laser pulse to quickly cool down rapidly. The surface of a NP conserves the energy of local heating, acting as an adiabatic shell. So, the electrons in a metallic NP remain hot for a very long time due to the relatively low thermal diffusivity of the medium and the hindered energy exchange of the gas of quasiparticles and molecules at the interface.

Conclusion

The transient absorption of gold NPs of various diameters has been studied. For this purpose, the method of pulsed photolysis with photoexcitation by nanosecond laser pulses was used. It has been established that the transient absorption bands for both small and large Au NPs have a maximum at about 430–440 nm and exhibit a fine structure of the spectrum. The decay kinetics of the transient absorption at 435 nm has a monoexponential form. The duration of the absorption decreases with a decrease in the average size of NPs. The nanosecond duration of the transient absorption of Au NPs is the result of a prolonged relaxation process in the “interface of gold NP–solvent molecule” system as a manifestation of hindered heat exchange with the environment.

The results obtained will be useful for the prediction of the dynamics of “hot” electrons in plasmonic NPs of metal. It was shown that under the action of nanosecond pulses, the lifetime of excited electrons in Au NPs is tens and hundreds of nanoseconds. It can be used for heat transfer from metal NPs to biological objects in photothermal therapy, biomedical imaging, activation of photocatalytic reactions and in photovoltaics for additional injection of electrons into a semiconductor layer, etc. [6, 10, 12, 20, 21].

Acknowledgments (or Funding)

The work was carried out within the framework of the research project AP14870117 funded by the Ministry of Science and Higher Education of the Republic of Kazakhstan

REFERENCES

1 Dzhanabekova R., Ibrayev N. SERS substrates based on silver nanoparticles and graphene oxide. *Bull. Univ. Karaganda-Phys.*, 2020, Vol. 97, No. 1, pp. 18–25.

2 Ibrayev N.K., Zhumabekov A.Z., Seliverstova E.V. Photoelectric properties of TiO_2-GO+Ag ternary nanocomposite material. *Eurasian J. Phys. Funct. Mater.*, 2020, Vol. 4 No. 3, pp. 261-267.

3 Ibrayev N., Afanasyev D., Omarova G. Features of stimulated emission of a merocyanine dye in the pores of anodized aluminium. *Eurasian Phys. Tech. J.*, 2021, Vol. 18 No. 2, pp. 29-34.

4 Siavash Moakhar R., Gholipour S., Masudy□Panah S., et al. Recent advances in plasmonic perovskite solar cells. *Adv. Sci.,* 2020, Vol. 7, pp. 1902448(1-19).

5 Seliverstova E., Ibrayev N., Omarova G., et al. Competitive influence of the plasmon effect and energy transfer between chromophores and Ag nanoparticles on the fluorescent properties of indopolycarbocyanine dyes. *J. Lumin.*, 2021, Vol. 235, p. 118000(1-8).

6 Gaál A., Bugár I., Capek I., et al. Femtosecond multicolor transient absorption spectroscopy of colloidal silver nanoparticles. *Laser Phys*., 2009, Vol. 5, pp. 961–968.

7 Hartland G.V. Ultrafast studies of single semiconductor and metal nanostructures through transient absorption microscopy. *Chem. Sci*, 2010, No. 1, pp. 303–309.

8 Kedawat G., Sharma I., Nagpal K., et al. Studies of ultrafast transient absorption spectroscopy of gold nanorods in an aqueous solution. *ACS Omega,* 2019, Vol. 4, pp. 12626–12631.

9 Ibrayev N., Seliverstova E., Kucherenko M. Features of nanosecond transient absorption of Ag nanoparticles with manifestations of electron gas degeneracy. *J. Lumin*., 2022, Vol. 245, pp. 118760(1-8).

10 García Calavia P., Bruce G., Pérez-García L., Russell D. A. Photosensitiser-gold nanoparticle conjugates for photodynamic therapy of cancer. *Photochem. Photobiol. Sci*., 2018, Vol. 17, pp. 1534-1552.

11 Kim H., Lee D. Near-infrared-Responsive cancer photothermal and photodynamic therapy using gold nanoparticles. *Polymers*, 2018, Vol. 10(9), pp. 961(1-14).

12 Vines J.B., Yoon J.-H., Ryu N.-E., et al. Gold nanoparticles for photothermal cancer therapy. *Front. Chem.*, 2019, Vol. 7, pp. 167(1-16).

13 Mendoza C., Désert A., Chateau D., et al. Au nanobipyramids@mSiO2 core–shell nanoparticles for plasmon-enhanced singlet oxygen photooxygenations in segmented flow microreactors. *Nanoscale Adv*., 2020, Vol. 11, pp. 5280–5287.

14 Farooq S., de Araujo R.E. Identifying high performance gold nanoshells for singlet oxygen generation enhancement. *Photodiagn. Photodyn. Ther*., 2021, Vol. 35, pp. 102466(1-8).

15 Seliverstova E., Ibrayev N., Alikhaidarova E. The effect of laser energy density on the properties of graphene dots. *Eurasian Phys. Tech. J.,* 2022. Vol. 19, No. 2(40), pp. 30-34.

16 Shafiqa A.R., Aziz A.A., Mehrdel B. Nanoparticle optical properties: size dependence of a single gold spherical nanoparticles. *J. Phys.: Conf. Ser.*, 2018, Vol. 1083, pp. 012040(1-5).

17 Huang X., El-Sayed M.A., Gold nanoparticles: Optical properties and implementations in cancer diagnosis and photothermal therapy. *J. Adv. Res*., 2010, Vol. 1, pp. 13–28.

18 Hergert W., Wriedt T. *The Mie Theory Basics and Application*. Springer-Verlag, Berlin Heidelberg, 2012, 259 p.

19 Klimov V.V. *Nanoplasmonics*. Fizmatlit, Moscow, 2009, 480 p.

20 Tang H., Chen Ch.-J., Zhulin Huang Zh., et al. Plasmonic hot electrons for sensing, photodetection, and solar energy applications: A perspective. *J. Chem. Phys*., 2020. Vol 152, pp. doi:10.1063/5.0005334

21 Reddy H., Shalaev V.M. Plasmonic hot-carriers and their applications: opinion. *Opt. Mater. Express*, 2021, Vol. 11, No. 11, pp. 3827-3832.

Article accepted for publication 17.11.2022

DOI 10.31489/2022No4/78-87

UDC 539.1

THE EFFECT OF TOPOLOGICAL DEFECT ON THE MASS SPECTRA OF HEAVY AND HEAVY-LIGHT QUARKONIA

Inyang E.P.[1]*, Obisung E.O.[2], Amajama J.[2], Bassey D E.[2], William E.S.[3], Okon I.B.[4]

[1] Department of Physics, National Open University of Nigeria, Jabi, Abuja, Nigeria, etidophysics@gmail.com, einyang@noun.edu.ng

[2]Department of Physics, University of Calabar, Calabar, Nigeria

[3]Theoretical Physics Group, Department of Physics, University of Calabar, Calabar, Nigeria

[4]Theoretical Physics Group, Department of Physics, University of UYO, Nigeria

In this present study, the effect of Topological Defect on the mass spectra of heavy and heavy-light mesons such as charmonium, bottomonium, and charm-strange $(c\bar{s})$ *,bottom-charm* $(b\bar{c})$ *respectively are studied with the Hulthen plus Yukawa potential. The Schrödinger equation is solved analytically using the Nikiforov-Uvarov method. The approximate solutions of the energy spectrum and un-normalized wave function were obtained. We applied the present results to predict the mass spectra of heavy and heavy-light mesons in the presence and absence of a topological defect for different quantum states. We noticed that when the topological defect increases the mass spectra are shifted and move closer to the experimental data. However, when compared to the work of other researchers, the results established an improvement.*

Keywords: Schrödinger equation; Nikiforov-Uvarov method; Hulthen-Yukawa Potential; Mass Spectra; Topological Defect

Introduction

The existence of heavy quark-bound states was discovered independently at the Stanford Linear Accelerator Center (SLAC) [1] and Brookhaven National Laboratory (BNL) [2] in 1974. Since then, the study of the quarkonia system has been investigated both experimentally and theoretically by particle physicists [3,4]. Studies on heavy quark systems are crucial because they provide knowledge on interaction potential, confinement, quantum chromodynamics (QCD) coupling constant, and various other inputs to the standard model [5]. The solutions of the Schrodinger equation (SE) with potential models are used in describing the energy spectra of diatomic molecules, theoretical measures, and mass spectra (MS) of the heavy and heavy-light mesons [6-8]. In the study of mass spectra of the heavy and heavy-light mesons, confining-type potentials are generally used. The widely used potential is the Cornell potential (CP) which contains a Coulomb interaction term and a linear confinement term [9]. Analytically, different methods have been proposed and employed in solving the SE with a chosen potential model of interest, such as, the Asymptotic iteration method AIM [10], the Nikiforov-Uvarov (NU) method [11,12], the NU Functional Analysis (NUFA) method [13,14], the series expansion method (SEM) [15], WKB approximation method [16], exact quantization rule [17], and so on. The analytical study of heavy quark with CP has gained remarkable attention from scholars [18,19]. For instance, Vega and Flores, [20] obtained the analytical solutions of the SE with CP using the vibrational method (VM) and super symmetric quantum mechanics. The eigenvalues were used to calculate the MS of the mesons. Also, Kumar et al. [21] used the NUFA method to solved the SE with generalized CP. The result was used to determine the MS of the heavy quarks. Furthermore, Hassanabadi, et al. [22], used the VM to solve the SE with CP. The mesonic wave function was computed using the eigenvalues. To examine the MS of mesons, researchers have recently modeled exponential-type potentials to study the MS of quarkonia [23]. The prediction of the MS of the heavy mesons (HMs), potential models such as Varshni [24], Hulthen plus Hellmann potential [25], and others have been used. For instance, Purohit et al. [26] used the solutions of the Klein-Gordon equation potential (KGE) to predict the HMs by combining linear plus modified Yukawa potentials.

Hulthen potential [27] and Yukawa potential [28] are used in different branches of physics, including nuclear and particle physics, among others. It has been noted that more experimental data tends to fit a mixture of at least two potential models than a single potential [27]. The Hulthen plus Yukawa potential

(HYP) was proposed by Li and Chang [29] to investigate the nonlinear optical characteristics of the GaAs/AlnGa1-n as quantum dots system. The HYP takes the form [29],

$$V(r) = -\frac{R_0 e^{-\vartheta r}}{1-e^{-\vartheta r}} - \frac{b e^{-\vartheta r}}{r} \ , \tag{1}$$

where R_0, and b are the strength of the potential, ϑ is the screening parameter and r is inter-nuclear distance.

Scholars have found the impact of a topological defect (TD) with a single particle in a particular potential to be an intriguing topic [30]. Its genesis is thought to have taken place during a phase transition in the early universe. Researchers have recently become interested in how TD affects the dynamics of both relativistic and non-relativistic systems, including screw dislocation [31], bound electron eigenstates, and holes to a declination. Furtado et al. [32] examined the Landau levels in the presence of a TD in light of these. Additionally, Hassanabadi and Hosseinpour [33] looked into how TD affected hydrogen atoms in curve-space time. Topological defects have long been a hot topic in domains like condensed matter and gravitational Physics [34]. They play a significant role in altering the physical characteristics of many quantum systems. A linear defect in an elastic medium, such as a dislocation or desperation, causes a change in the topology of the medium, which has an effect on the medium's physical characteristics [34]. Ahmed [35] investigated how TD and external fields affected diatomic molecules. It was demonstrated that the TD and external fields cause the energy levels to change. No researchers are yet to report the impact of TD on the mass spectra of heavy and heavy-light mesons in light of these observations. Therefore, the purpose of this study is to use the NU approach to solve SE with HYP in order to examine the effect of TD on the mass spectra of heavy and heavy-light mesons. For convenience, we have assumed that our mesons are spinless particles [36].

Equation 1 is modeled to include the Coulomb and confinement terms using a series of powers up to order three to expand the exponential terms, and we get

$$V(r) = -\frac{B}{r} + Ar + Dr^2 + \mathrm{E} \ , \tag{2}$$

where

$$\left.\begin{aligned} B &= \frac{R_0}{\vartheta} + 2b, \ \mathrm{A} = -\frac{\vartheta R_0}{12} - \frac{b\vartheta^2}{2} \\ D &= \frac{b\vartheta^2}{6}, \ \mathrm{E} = \frac{R_0}{2} + b\vartheta \end{aligned}\right\} \tag{3}$$

2. Formalism

The line element that explains spacetime with a point-like global monopole (PGM) takes the form: [30]

$$ds^2 = -c^2dt^2 + \frac{dr^2}{\alpha^2} + r^2d\theta^2 + r^2\sin^2\theta d\varphi^2 \tag{4}$$

where $0 \prec \alpha = 1 - 8\pi G\eta_0^2 \prec 1$ is the parameter related to the PGM which depends on the energy scale η_0. Furthermore, Eq. (4) portrays a space time with scalar curvature

$$R = R_\mu^\mu = \frac{2\left(1-\alpha^2\right)}{r^2} \tag{5}$$

In this way, the SE takes the form

$$-\frac{\hbar^2}{2\mu}\nabla_{LB}^2\psi(\vec{r},t) + V(r,t)\psi(\vec{r},t) = i\hbar\frac{\partial\psi(\vec{r},t)}{\partial t} \tag{6}$$

where μ is the particle's mass, $\nabla_{LB}^2 = \frac{1}{\sqrt{g}}\partial_i\left(\sqrt{g}g^{ij}\partial_j\right)$ with $g = \det(g_{ij})$, is the Laplace-Beltrami operator and $V(r,t) = V(r)$ is GMP(1).Thereby, the SE for the GMP in a medium with the presence of the PGM(1) is

$$-\frac{\hbar^2}{2\mu r^2}\left[\begin{array}{l}\alpha^2\dfrac{\partial}{\partial r}\left(r^2\dfrac{\partial}{\partial r}\right)+\dfrac{1}{\sin\theta}\dfrac{\partial}{\partial\theta}\left(\sin\theta\dfrac{\partial}{\partial\theta}\right)\\ +\dfrac{1}{\sin^2\theta}\dfrac{\partial^2}{\partial\varphi^2}\end{array}\right]\psi(r,\theta,\varphi,t)+V\psi(r,\theta,\varphi,t)=i\hbar\frac{\partial\psi(r,\theta,\varphi,t)}{\partial t} \tag{7}$$

Here, let us consider a particular solution to Eq.(5) given in terms of the eigenvalues of the angular momentum operator $\hat{L}^2$ as

$$\psi(r,\theta,\varphi,t)=e^{-\frac{E_{nl}t}{\hbar}}\frac{U(r)}{r}Y_{l,m}(\theta,\varphi) \tag{8}$$

where $Y_{l,m}(\theta,\varphi)$ are spherical harmonics and $R(r)$ is the radial wave function.

3.The solutions of the Schrödinger equation with Hulthen-Yukawa Potential11

The NU technique is used in this investigation. The details are provided in Ref. [11]. Then, we substitute Eq. (2) into Eq.(7), the radial wave equation is obtain as

$$\frac{d^2R(r)}{dr^2}+\left[\frac{2\mu E_{nl}}{\alpha^2\hbar^2}+\frac{2\mu B}{\alpha^2\hbar^2 r}-\frac{2\mu Ar}{\alpha^2\hbar^2}-\frac{2\mu Dr^2}{\alpha^2\hbar^2}-\frac{2\mu E}{\alpha^2\hbar^2}-\frac{l(l+1)}{\alpha^2r^2}\right]R(r)=0 \tag{9}$$

Let,

$$x=\frac{1}{r} \tag{10}$$

Putting Eq. (10) into Eq. (9), gives

$$\frac{d^2R(\mathrm{x})}{dx^2}+\frac{2x}{x^2}\frac{dR}{dx}+\frac{1}{x^4}\left[\frac{2\mu E_{nl}}{\alpha^2\hbar^2}+\frac{2\mu Bx}{\alpha^2\hbar^2}-\frac{2\mu A}{\alpha^2\hbar^2x}-\frac{2\mu D}{\alpha^2\hbar^2x^2}-\frac{2\mu E}{\alpha^2\hbar^2}-\frac{l(l+1)x^2}{\alpha^2}\right]R(\mathrm{x})=0 \tag{11}$$

The approximation scheme (AS) on the terms $\frac{A}{x}$ and $\frac{D}{x^2}$ is introduced by assuming that there is a characteristic radius r_0 of the meson. The AS is achieved by the expansion in a power series around r_0 ; i.e. around $\delta\equiv\frac{1}{r_0}$, up to the second order [24]. By setting $y=x-\delta$ and around $y=0$ we have;

$$\frac{A}{x}=\frac{\alpha_1}{y+\delta}=\frac{\alpha_1}{\delta\left(1+\frac{y}{\delta}\right)}=\frac{\alpha_1}{\delta}\left(1+\frac{y}{\delta}\right)^{-1} \tag{12}$$

Equation (12) yields

$$\frac{A}{x}=A\left(\frac{3}{\delta}-\frac{3x}{\delta^2}+\frac{x^2}{\delta^3}\right), \tag{13}$$

Similarly,

$$\frac{D}{x^2}=D\left(\frac{6}{\delta^2}-\frac{8x}{\delta^3}+\frac{3x^2}{\delta^4}\right) \tag{14}$$

Equations (13) and (14) are Plugged into Eq. (11) and yields,

$$\frac{d^2R(x)}{dx^2}+\frac{2x}{x^2}\frac{dR(x)}{dx}+\frac{1}{x^4}\left[-\varepsilon+\beta_1x-\beta_2x^2\right]R(x)=0 \tag{15}$$

,

where

$$\left.\begin{array}{l}-\varepsilon=\left(\dfrac{2\mu E_{nl}}{\alpha^2\hbar^2}-\dfrac{6\mu A}{\alpha^2\hbar^2\delta}-\dfrac{12\mu D}{\alpha^2\hbar^2\delta^2}-\dfrac{6\mu E}{\alpha^2\hbar^2}\right),\ \beta_1=\left(\dfrac{2\mu B}{\alpha^2\hbar^2}+\dfrac{6\mu A}{\alpha^2\hbar^2\delta^2}+\dfrac{16\mu D}{\alpha^2\hbar^2\delta^3}\right)\\ \beta_2=\left(\dfrac{2\mu A}{\alpha^2\hbar^2\delta^3}+\dfrac{6\mu D}{\alpha^2\hbar^2\delta^4}+\dfrac{l(l+1)}{\alpha^2}\right)\end{array}\right\} \tag{16}$$

Linking Eq.(15) and Eq. (1) of Ref. [11], we obtain

$$\left.\begin{aligned}\tilde{\tau}(x)&=2x,\ \sigma(x)=x^2\\ \tilde{\sigma}(x)&=-\varepsilon+\beta_1 x-\beta_2 x^2\\ \sigma'(x)&=2x,\ \sigma''(x)=2\end{aligned}\right\} \tag{17}$$

Equation (17) is substituted into Ref. [11]'s Eq. (11) to produce

$$\pi(x)=\pm\sqrt{\varepsilon-\beta_1 x+(\beta_2+k)x^2} \tag{18}$$

The value of k is obtained by taking the discriminant of the function under the square root.

$$k=\frac{\beta_1^2-4\beta_2\varepsilon}{4\varepsilon} \tag{19}$$

Plugging Eq. (19) into Eq. (18) gives

$$\pi(x)=\pm\left(\frac{\beta_1 x}{2\sqrt{\varepsilon}}-\frac{\varepsilon}{\sqrt{\varepsilon}}\right) \tag{20}$$

From Eq. (20), we have

$$\pi'_{-}(x)=-\frac{\beta_1}{2\sqrt{\varepsilon}} \tag{21}$$

Putting Eqs. (17) and (20) into Eq.(6) of Ref. [11] gives

$$\tau(x)=2x-\frac{\beta_1 x}{\sqrt{\varepsilon}}+\frac{2\varepsilon}{\sqrt{\varepsilon}} \tag{22}$$

From Eq. (22) we get

$$\tau'(x)=2-\frac{\beta_1}{\sqrt{\varepsilon}} \tag{23}$$

Using Eqs. (10) and (13) from Ref. [11], we have the following,

$$\lambda=\frac{\beta_1^2-4\beta_2\varepsilon}{4\varepsilon}-\frac{\beta_1}{2\sqrt{\varepsilon}} \tag{24}$$

$$\lambda_n=\frac{n\beta_1}{\sqrt{\varepsilon}}-n^2-n \tag{25}$$

Equating Eqs. (24) and (25), followed by substitution of Eqs. (3) and (16) yield the energy spectrum of the HYP

$$E_{nl}=\frac{a}{2}+b\vartheta-\frac{3}{2\delta}\left(\frac{a\vartheta}{6}+b\vartheta^2\right)+\frac{b\vartheta^2}{\delta^2}-\frac{\alpha^2\hbar^2}{8\mu}\left[\frac{\frac{2\mu}{\alpha^2\hbar^2}\left(b+\frac{a}{\vartheta}\right)-\frac{3\mu}{\alpha^2\hbar^2\delta^2}\left(\frac{a\vartheta}{6}+b\vartheta^2\right)+\frac{8\mu b\vartheta^2}{3\alpha^2\hbar^2\delta^3}}{n+\frac{1}{2}+\sqrt{\frac{1}{4}-\frac{\mu W_1}{\alpha^2\hbar^2\delta^3}\left(\frac{a\vartheta}{6}+b\vartheta^2\right)+\frac{\mu b\vartheta^2}{\alpha^2\hbar^2\delta^4}+\frac{l(l+1)}{\alpha^2}}}\right]^2 \tag{26}$$

In terms of related Laguerre polynomials, the un-normalized wave function is given as

$$\psi(z)=N_{nl}\,z^{-\frac{\alpha}{2\sqrt{\varepsilon}}}e^{-\frac{\varepsilon}{z\sqrt{\varepsilon}}}L_n^{\frac{\alpha}{\sqrt{\varepsilon}}}\left(\frac{2\varepsilon}{z\sqrt{\varepsilon}}\right) \tag{27}$$

where N_{nl} is normalization constant, which can be obtained from

$$\int_0^\infty |\psi_{nl}(r)|^2 dr=1 \tag{28}$$

4. Results and discussion

Using the following equation [37], the MS of the heavy and heavy-light mesons are predicted

$$\mathrm{M}=m_x+m_{\bar{x}}+E_{nl} \tag{29}$$

where m_x is quarkonia mass and E_n is eigenvalues.

Substituting Eq. (26) into Eq. (29) we have,

$$\mathrm{M} = m_x + m_{\bar{x}} + \frac{a}{2} + b\vartheta - \frac{3}{2\delta}\left(\frac{a\vartheta}{6} + b\vartheta^2\right) + \frac{b\vartheta^2}{\delta^2} - \frac{\alpha^2\hbar^2}{8\mu}\left[\frac{\frac{2\mu}{\alpha^2\hbar^2}\left(b + \frac{a}{\vartheta}\right) - \frac{3\mu}{\alpha^2\hbar^2\delta^2}\left(\frac{a\vartheta}{6} + b\vartheta^2\right) + \frac{8\mu b\vartheta^2}{3\alpha^2\hbar^2\delta^3}}{n + \frac{1}{2} + \sqrt{\frac{1}{4} - \frac{\mu}{\alpha^2\hbar^2\delta^3}\left(\frac{a\vartheta}{6} + b\vartheta^2\right) + \frac{\mu b\vartheta^2}{\alpha^2\hbar^2\delta^4} + \frac{l(l+1)}{\alpha^2}}}\right]^2 \quad (30)$$

where μ is the reduced mass and α is the TD.

The numerical values of the heavy and heavy-light meson masses are taken from [38]. The potential parameters were fitted with experimental data (ED). Experimental data are taken from [39, 40].

The MS of the heavy and heavy-light mesons were predicted in the absence and presence of TD for different quantum states. Absence and presence corresponds to when α=1 and $\alpha = 2 = 3$ respectively. The mass spectra of charmonium in the presence of TD is seen to be exactly as the ED for 1S and 2S quantum state, but in other states we noticed that they predicted results are close to the ED. As the TD was introduced by setting TD = 2 and 3, the values of the predicted masses were seen to be approaching the ED and was seen to be improved from works reported by [15,37] as shown in Table 1.

Table 1: Mass spectra of charmonium in (GeV)

(m_c =1.209 GeV,μ= 0.6045 GeV,α=1.0 ,a = -3.5647 GeV, b = 352.7375 GeV,δ= 1.65 GeV, θ=0.01,$\hbar$= 1)

(m_c =1.209 GeV,μ= 0.6045 GeV,α=2.0 ,a = -3.64024 GeV, b = 356.5334 GeV,δ= 1.65 GeV, θ=0.01,$\hbar$= 1)

(m_c =1.209 GeV,μ= 0.6045 GeV,α=3.0 ,a = -3.7153 GeV, b = 360.2911 GeV,δ= 1.65 GeV, θ=0.01,$\hbar$= 1)

State	α	Our Result	AIM[37]	SEM[15]	Experiment [39]
1S	1.0	3.096000024	3.096	3.095922	3.096
	2.0	3.095999987	3.096	3.095922	3.096
	3.0	3.096000033	3.096	3.095922	3.096
2S	1.0	3.686000010	3.686	3.685893	3.686
	2.0	3.685999995	3.686	3.685893	3.686
	3.0	3.686000014	3.686	3.685893	3.686
3S	1.0	4.012881463	4.275	4.322881	4.040
	2.0	4.022871465	4.275	4.322881	4.040
	3.0	4.039981463	4.275	4.322881	4.040
4S	1.0	4.133343194	4.865	4.989406	4.263
	2.0	4.163343195	4.865	4.989406	4.263
	3.0	4.196335319	4.865	4.989406	4.263
1P	1.0	3.23224764	3.214	-	3.525
	2.0	3.399250489	3.214	-	3.525
	3.0	3.511700284	3.214	-	3.525
2P	1.0	3.568719439	3.773	3.756506	3.773
	2.0	.763087336	3.773	3.756506	3.773
	3.0	3.771820015	3.773	3.756506	3.773
1D	1.0	3.454603197	3.412	-	3.770
	2.0	3.624976340	3.412	-	3.770
	3.0	3.892528368	3.412	-	3.770
2D	1.0	3.802639037	-	-	4.159
	2.0	3.867334734	-	-	4.159
	3.0	3.987992543	-	-	4.159

For bottomonium, the mass spectra for 1S and 2S states are seen to be equal to ED. But when the TD was introduced the mass spectra increases and tends to approach the ED and was improved in comparison to the report by [15,37] as shown in Table 2. In the case of bottom-charm ($b\bar{c}$) ,when TD was absence, the

values of the calculated masses for 1S and 2S agreed with the ED as well as the when the TD was set to 2 and 3.

We noticed that 3S, 1P and 2P do not have ED for comparison. The predicted values for 3S,1P and 2P increase as the TD is increased and was seen to be improved from the works reported by [41,43,44] as shown in Table 3. The prediction of the mass spectra of charm-strange $(c\bar{s})$ meson shows that when TD = 1,1S and 2S states agreed with ED. Also, when TD = 2 = 3,1S and 2S also agreed with the ED. We noticed that as the TD increases the values of the calculated values increases and approaches the ED and was seen to be improved from the works reported by [41,42] as shown in Table 4.

The mass spectra of heavy and heavy-light mesons are plotted against the principal quantum number (n) as shown in Figs.1-4. In Fig.1, the MS of charmonium is plotted against n, it is observed that as TD increases from 1 to 3, the MS increases. In Fig.2, the MS of bottomonium is plotted against n.

Table 2: Mass spectra of bottomonium in (GeV)

$(m_b = 4.823\ GeV, \mu = 2.4115\ GeV,\ a = -1.6952\ GeV,\ b = 167.7012\ GeV, \theta = 0.01, \delta = 1.65\ GeV, \hbar = 1, \alpha = 1)$

$(m_b = 4.823\ GeV, \mu = 2.4115\ GeV,\ a = -1.73281\ GeV,\ b = 169.61855\ GeV, \theta = 0.01, \delta = 1.65\ GeV, \hbar = 1, \alpha = 2)$

$(m_b = 4.823\ GeV, \mu = 2.4115\ GeV,\ a = -1.7696\ GeV,\ b = 171.4677\ GeV, \theta = 0.01, \delta = 1.65\ GeV, \hbar = 1, \alpha = 3)$

State	α	Our Result	AIM[37]	SEM[15]	Experiment[39]
1S	1.0	9.460000022	9.460	9.515194	9.460
	2.0	9.459999989	9.460	9.515194	9.460
	3.0	9.460000048	9.460	9.515194	9.460
2S	1.0	10.02300001	10.023	10.01801	10.023
	2.0	10.02299999	10.023	10.01801	10.023
	3.0	10.02300003	10.023	10.01801	10.023
3S	1.0	10.30289537	10.585	10.44142	10.355
	2.0	10.31001127	10.585	10.44142	10.355
	3.0	10.34493277	10.585	10.44142	10.355
4S	1.0	10.38099212	11.148	10.85777	10.580
	2.0	10.47097214	11.148	10.85777	10.580
	3.0	10.56709741	11.148	10.85777	10.580
1P	1.0	9.626090124	9.492	-	9.899
	2.0	9.799443695	9.492	-	9.899
	3.0	10.02340701	9.492	-	9.899
2P	1.0	10.22006701	10.038	10.09446	10.260
	2.0	10.24115658	10.038	10.09446	10.260
	3.0	10.25907436	10.038	10.09446	10.260
1D	1.0	9.802224210	9.551	-	10.164
	2.0	9.964826266	9.551	-	10.164
	3.0	10.22010124	9.551	-	10.164

Table 3: Mass spectra of b$\bar{c}$ meson in (GeV)

$(m_t = 1.209\ GeV, m_b = 4.823\ GeV, \mu = 0.967\ GeV,\ a = -2.7002\ GeV,\ b = 267.0454\ GeV, \theta = 0.01, \delta = 1.6\ GeV, \hbar = 1, \alpha = 1.0)$

$(m_t = 1.209\ GeV, m_b = 4.823\ GeV, \mu = 0.967\ GeV,\ a = -2.7604\ GeV,\ b = 270.0844\ GeV, \theta = 0.01, \delta = 1.6\ GeV, \hbar = 1, \alpha = 2.0)$

$(m_t = 1.209\ GeV, m_b = 4.823\ GeV, \mu = 0.967\ GeV,\ a = -2.8202\ GeV,\ b = 273.0768\ GeV, \theta = 0.01, \delta = 1.6\ GeV, \hbar = 1, \alpha = 3.0)$

State	α	Our Result	[43]	[44]	[41]	Experiment [40]
1S	1.0	6.273999877	6.349	6.264	6.268	6.274
	2.0	6.273999987	6.349	6.264	6.268	6.274
	3.0	6.273999990	6.349	6.264	6.268	6.274
2S	1.0	6.870999945	6.821	6.856	6.895	6.871
	2.0	6.870999994	6.821	6.856	6.895	6.871
	3.0	6.870999996	6.821	6.856	6.895	6.871
3S	1.0	7.079844893	7.175	7.244	7.522	-
	2.0	7.079923693	7.175	7.244	7.522	-
	3.0	7.079938283	7.175	7.244	7.522	-
1P	1.0	6.450099644	6.715	6.700	6.529	-
	2.0	6.580866397	6.715	6.700	6.529	-

	3.0	6.871276565	6.715	6.700	6.529	-
2P	1.0	6.925459986	7.156	7.108	7.102	-
	2.0	6.969242914	7.156	7.108	7.102	-
	3.0	7.079961566	7.156	7.108	7.102	-

Table 4: Mass spectra of $c\bar{s}$ meson in (GeV)
(m_c =1.209 GeV,$m_{\bar{s}}$ =0.419 GeV,μ= 0.3111 GeV,θ=0.01,a= -2.0227 GeV, b = 198.2519 GeV,δ= 1.6 GeV, $\hbar$=1,α=1.0)
(m_c =1.209 GeV,$m_{\bar{s}}$ =0.419 GeV,μ= 0.3111 GeV,θ=0.01,a= -2.1031 GeV, b = 202.2735 GeV,δ= 1.6 GeV, $\hbar$=1,α=2.0)
(m_c =1.209 GeV,$m_{\bar{s}}$ =0.419 GeV,μ= 0.3111 GeV,θ=0.01,a= -2.0227 GeV, b = 206.3001 GeV,δ= 1.6 GeV, $\hbar$=1,α=3.0)

State	α	Our Result	[41]	AIM[42]	Exp.[40]
1S	1.0	1.967999992	1.969	2.512	1.968
	2.0	1.968000003	1.969	2.512	1.968
	3.0	1.968000009	1.969	2.512	1.968
2S	1.0	2.316999996	2.318	2.709	2.317
	2.0	2.317000002	2.318	2.709	2.317
	3.0	2.317000004	2.318	2.709	2.317
3S	1.0	2.569135452	2.667	2.906	2.700
	2.0	2.655146351	2.667	2.906	2.700
	3.0	2.709948372	2.667	2.906	2.700
1P	1.0	2.070929595	2.126	2.649	2.112
	2.0	2.147345620	2.126	2.649	2.112
	3.0	2.157038303	2.126	2.649	2.112
1D	1.0	2.180107355	2.374	2.859	2.318
	2.0	2.28087479	2.374	2.859	2.318
	3.0	2.319154842	2.374	2.859	2.318

A similar trend is observed. The variation of MS of charm-strange $(c\bar{s})$ against n is plotted as shown in Fig.3. It is observed that the mass spectra, increases as TD is increased In Fig.4, the MS of bottom-charm $(b\bar{c})$, is plotted against the principal quantum number. The MS is seen to increase when the values of TD is increased, which shows the effect of TD on the mass spectra.

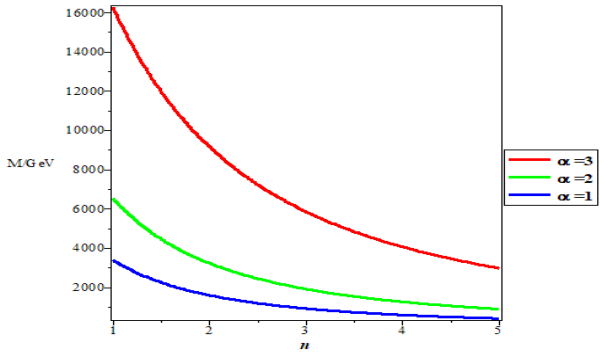

Fig.1. Variation of the mass spectra of charmonium with principal quantum number for different values of α

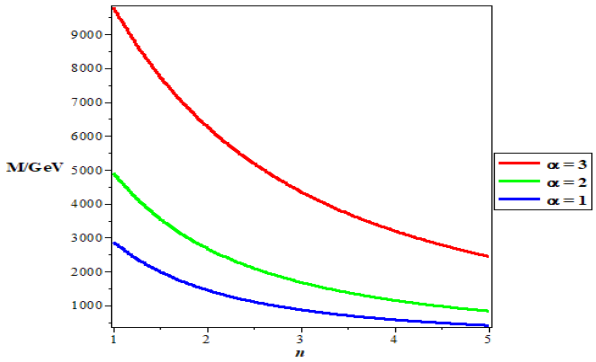

Fig.2. Variation of the mass spectra of bottomonium with principal quantum number for different values of α

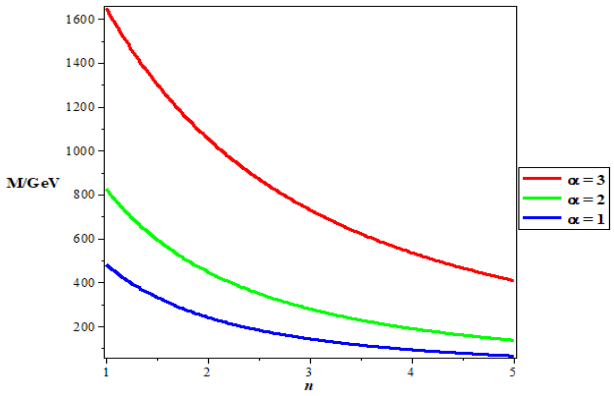

Fig.3. Variation of the mass spectra of $c\bar{s}$ meson with principal quantum number for different values of α

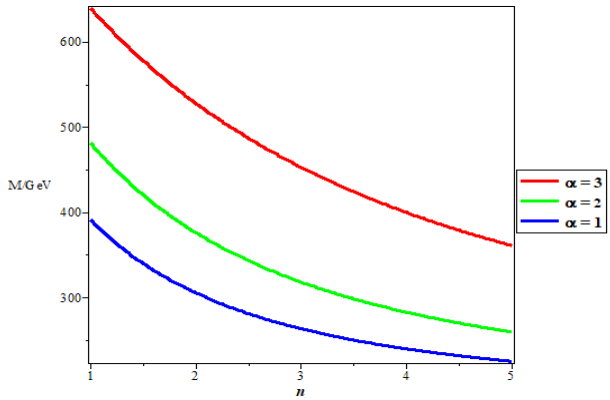

Fig.4. Variation of the mass spectra of $b\bar{c}$ meson with principal quantum number for different values of α

Conclusion

In the current study, the Hulthen-Yukawa Potential is used to examine the effect of Topological Defect on the mass spectra of heavy and heavy-light mesons such as charmonium, bottomonium, charm-strange, and bottom-charm respectively. Analytically, the SE was solved using the NU approach. The un-normalized wave function and the energy spectrum were found. The mass spectra of heavy and heavy-light mesons in the presence and absence of TD for various quantum states were predicted. We observed that the mass spectra rise and shift closer to the ED as the TD increases. However, when compared to the work of other researchers, the results obtained demonstrated an improvement. This research could be expanded to examine the thermal properties of heavy and heavy-light mesons.

REFERENCES

1 Augustin J.E., Boyarski A.M., Breidenbach M. Discovery of a narrow resonance in e+e- annihilation. *Physical Review Letter*, 1974, Vol. 33, pp. 1408.

2 Aubert J.J., Becker U., Biggs P.J. Experimental observation of a heavy particle. *Physical Review Letters,* 1974, Vol. 33, pp. 1406.

3 Allosh M., Mustafa Y., Ahmed N.K., Mustafa A.S. Ground and Excited state mass spectra and properties of heavy-light mesons, *Few-Body Systems*,2021, Vol. 62, pp 234**.**

4 Omugbe E., Osafile O.E., Okon I.B., Inyang E.P., William E.S., Jahanshir A. Any L-state energy of the spinless Salpeter equation under the Cornell potential by the WKB Approximation method: An Application to mass spectra of mesons. *Few-Body Systems* 2022,Vol. 63, pp 7.

5 Bhaghyesh A. Charmonium properties using the Discrete variable representation (DVR) method. *Advances in High Energy Physics,* 2021, pp.7. doi:10.1155/2021/9991152

6 Inyang E.P., William E.S., Obu J.O., Ita B. I., Inyang E.P., Akpan I.O. Energy spectra and expectation values of selected diatomic molecules through the solutions of Klein-Gordon equation with Eckart-Hellmann potential model. *Molecular Physics,* 2021, Vol.119, e1956615. doi: 10.1080/00268976.2021.1956615

7 Omugbe E., Osafile O.E., Okon I. B., et al. Non - relativistic bound state solutions with l -deformed Kratzer-type potential using the super-symmetric WKB method: application to theoretic-information measures. *European Physical Journal D,* 2022, Vol.76, pp.11.

8 Akpan I.O., Inyang E.P., Inyang E.P., William E.S. Approximate solutions of the Schrödinger equation with Hulthen-Hellmann Potentials for a Quarkonium system. *Revista Mexica De Fisica,* 2021. Vol.67, pp. 490.

9 Mutuk H. Mass Spectra and Decay constants of Heavy-light Mesons: A case study of QCD sum Rules and Quark model. *Advances in High Energy Physics,* 2018, Vol.20**,** pp.653.

10 Edet C.O., Mahmoud S., Inyang E.P., Ali N., Aljunid A., Endut R., IkotA.N., Asjad M.. Non-Relativistic Treatment of the 2D Electron System Interacting via Varshni-Shukla Potential Using the Asymptoptic Iteration Method. *Mathematics,* 2022, Vol.10, pp.2824. doi: 10.3390/math10152824

11 Nikiforov S.K., Uvarov V.B. Special functions of Mathematical Physics, Birkhauser, Basel, 1988. http://dx.doi.org/10.1007/978-1-4757-1595-8

12 William E. S., Inyang E. P., Thompson E. A. Arbitrary ℓ-solutions of the Schrödinger equation interacting with Hulthén-Hellmann potential model. *Revista Mexicana Fisica,* 2020, Vol**.** 66, pp. 730. doi: 10.31349/RevMexFis.66.730

13 Ikot A.N., Okorie U.S., Amadi P.O., Edet C.O., Rampho G.J., Sever R. The Nikiforov-Uvarov –Functional Analysis (NUFA) Method: A new approach for solving exponential – Type potentials. *Few-Body System,* 2021, Vol.62**,** pp. 9. doi: 10.1007/s00601-021-021-01593-5

14 Inyang E.P., Iwuji P.C., Ntibi J.E., Omugbe E., Ibanga E.A., William E.S. Quark-antiquark study with inversely quadratic Yukawa potential using Nikiforov-Uvarov-Functional analysis method. *East European Journal of Physics*, 2022, Vol. 2, pp.51. doi: 10.26565/2312-4334-2022-2-05

15 Inyang E.P., Iwuji P.C., Ntibi J.E., William E.S., Ibanga E.A. Solutions of the Schrodinger equation with Hulthen –screened Kratzer potential: Application to diatomic molecules. *East European Journal of Physics*, 2022, Vol.1, pp.11. doi: 10.26565/2312-4334-2022-2-02

16 Omugbe E., Osafile O.E., Inyang E.P., Jahanshir A. Bound state solutions of the hyper-radial Klein-Gordon equation under the Deng-Fan potential by WKB and SWKB methods. *Physica Scripta*, 2021, Vol. 96, pp. 125408.

17 Dong S.H., Cruz-Irisson M.Energy spectrum for a modified Rosen-Morse potential solved by proper quantization rule and its thermodynamic properties. *Journal of Mathematical Chemistry,* 2012, Vol.50, pp. 892.

18 Abu-shady M., Edet C.O., Ikot A.N. Non-relativistic Quark model under external magnetic and Aharanov-Bohm (AB) fields in the presence of Temperature-Dependent confined Cornell potential. *Canadian Journal of Physics,* 2021. doi: 10.11139/cjp-2020-0101

19 Prasanth J.P., Sebastian K., Bannur V.M. Revisiting Cornell potential model of the Quark-Gluon plasma. *Physica A*, 2020, Vol.558, pp.124921.

20 Vega A., Flores J. Heavy quarkonium properties from Cornell potential using variational method and supersymmetric quantum mechanics. *Pramana Journal of Physics*, 2016, Vol.87, pp.46.

21 Kumar R., Singh R.M., Bhahardivaj S.B., Rani R., Chand F. Analytical solutions to the Schrodinger equation for generalized Cornell potential and its application to diatomic molecules and heavy mesons. *Modern Physics Letter A.*, 2022, Vol. 37, pp.2250010.

22 Hassanabadi H., Ghafourian M., Rahmani S. Study of the Heavy-Light mesons properties via the Variational method for Cornell interaction. *Few-Body System,* 2016, Vol.15, pp. 6.

23 Inyang E.P., Inyang E.P., Ntibi J.E., William E.S. Analytical solutions of Schrodinger equation with Kratzer-screened Coulomb potential for a Quarkonium system. *Bulletin of Pure and Applied Sciences*, 2021, Vol.40, pp.24. doi:10.5958/2320-3218.2021.0002.6

24 Inyang E.P., Inyang E.P., William E., et al. Study on the applicability of Varshni potential to predict the mass-spectra of the Quark-Antiquark systems in a non-relativistic framework. *Jordan Journal of Physics,* 2021, Vol.14, pp.345.

25 Inyang E.P., Inyang E.P., Akpan I.O., Ntibi J.E., William E.S. Masses and thermodynamic properties of a Quarkonium system. *Canadian Journal Physics,* 2021, Vol. 99, pp.990. doi: 10.1139/cjp-2020-0578

26 Purohit K. R., Jakhad P. Rai A.K., Quarkonium spectroscopy of the linear plus modified Yukawa potential. *Physica Scripta,* 2022, Vol. 97, pp. 044002.

27 Hulthen L. Über die eigenlosunger der Schro¨dinger-Gleichung des deuterons, Ark. Mat. *Astronomy Physics A.,* 1942, Vol. 28, pp.5.

28 Yukawa H. On the interaction of elementary particles. *Proc. Phys. Math. Soc,. Jap*an. 1935, Vol. 17, pp. 48.

29 Li X., Chang C. Nonlinear optical properties of GaAs/Al_nGa_{1-n} as quantum dots system with Hulthen-Yukawa potential. *Optical materials,* 2022, Vol.131, pp.112605.

30 Edet C.O., Ikot A.N. Effect of Topological Defect on the Energy spectra and Thermo-magnetic properties of CO diatomic molecule. *Journal Low Temperature Physics*, 2021, Vol. 203, pp.111.

31 Furtado C., Morades F. Landau levels in the presence of a screw dislocation. *Europhysics Letter*, 1999, Vol.45, pp.282.

32 Furtado C., F.Morades. On the binding of electrons and holes to disclinations. *Physics Letter A.*, 1994, Vol.188, pp.396.

33 Hassanabadi H., Hosseinpour M. Thermodynamic properties of neutral particle in the presence of topological defects in magnetic cosmic string background. *European Physical Journal C.,* 2016, Vol.76, pp.553.

34 Nwabuzor P., Edet C., Ikot A.N., Okorie U., Ramantswana M., Horchani R., Abdel-Aty A., Rampho G. Analyzing the effects of Topological Defect (TD) on the Energy spectra and Thermal Properties of LiH, TiC and I_2 diatomic molecules. *Entropy,* 2021, Vol.23*(8),* pp.1060. doi: 10.3390/e23081060

35 Ahmed F. Approximate eigenvalue solutions with diatomic molecular potential under topological defects and Aharonov-Bohm flux field: application for some known potentials. *Molecular Physics,* 2022, 2124935.

36 Jacobs S., Olsson M.G., Suchyta C. Comparing the Schrodinger and Spinless Salpeter equations for heavy-quark bound states. *Physical Review D.*, 1986, Vol. 33, pp. 3338.

37 Ciftci H., Kisoglu H.F. Nonrelativistic-Arbitrary l-states of quarkonium through Asymptotic Iteration method. *Advances in High Energy Physics,* 2018, 4549705.

38 Olive R., Groom D. E., Trippe T.G. Particle Data Group, *Chinese Physics C.,* 2014, Vol.38, pp. 60.

39 Tanabashi M., Carone, C. D., Trippe T.G., Wohl C.G. Particle Data Group, *Physical Review D.,* 2018, Vol.98, pp.546.

40 Patrignani C. et al., Particle data group, *Chinese Physics C.*, 2016, Vol.40, 100001.

41 Abu-Shady M., Ezz-Alarab S.Y. Trigonometric Rosen–Morse Potential as a Quark–Antiquark Interaction Potential for Meson Properties in the Non-relativistic Quark Model Using EAIM. *Few-Body Systems*, 2019, Vol. 60, pp 66.

42 Rani R., Bhardwaj S. B., Chand F., Mass Spectra of Heavy and Light Mesons Using Asymptotic Iteration Method, *Communication in Theoretical Physics,* 2018, Vol.70, pp.179.

43 Kumar A., Vinodkumar P. C. Properties of B_c meson. *Pramana Journal of Physics,* 2006, Vol.66, pp.958.

44 Eichten E.J., Quigg C. Mesons with beauty and charm: Spectroscopy. *Physical Review D.* ,1994, Vol. 49, pp.5845.

Article accepted for publication 26.07.2022

DOI 10.31489/2022No4/88

Eurasian Physical Technical Journal, 2021, Vol.18, No.1 (35)

CORRECTION
to the article «**RELATIONSHIP BETWEEN MAGNETIC PROPERTIES AND MICROSTRUCTURE OF FERRITES DURING SINTERING IN RADIATION AND RADIATION-THERMAL CONDITIONS**»
by Malyshev A.V., Lysenko E.N., Sheveleva E.A., Surzhikova O.A., Aringazin A.K.

Eurasian Physical Technical Journal, 2021, Vol.18, No.1 (35), pp. 3 – 8.

with affiliations:
[1]Tomsk Polytechnic University, Tomsk, Russia, malyshev@tpu.ru
[2]Ceské vysoké ucení technické v Prague, Prague, Czech Republic
[3]L.N. Gumilev Eurasian National University, Nur-Sultan, Kazakhstan

1) Authors name shood be read as:
Malyshev A.V., Lysenko E.N., Sheveleva E.A., Surzhikova O.A.

2) Affiliations shood be read as:
[1]Tomsk Polytechnic University, Tomsk, Russia, malyshev@tpu.ru
[2]Ceské vysoké ucení technické v Prague, Prague, Czech Republic

SUMMARIES	ТҮСІНІКТЕМЕЛЕР	АННОТАЦИИ

Кучеренко М. Г., Неясов П. П.

Ферромагниттік нанобөлшек бетіндегі триплет-қозған молекулалардың спин-селективті өзара әрекеттесуі.

Ферромагниттік нанобөлшектің генерациялайтын магнит өрісінің триплеттік қозған органикалық молекулалардың немесе бөлшектердің беткі қабатындағы триплеттік экситондардың аннигиляциясына әсері зерттелген. Электрондық қозудың диффузиялық қозғалғыштығын және жүйенің геометриясын ескеретін егжей-тегжейлі математикалық модель ұсынылған. Кинетикалық оператор триплет-триплет жұбының 9х9 спиндік күйлерінің толық базасында берілген. Триплет-триплет жұбының синглеттік спин күйінің қоныстануының уақыттық тәуелділіктері және триплет-триплет аннигиляциясы кезіндегі магниттік дауыс профилінің (магниттік реакция әсері) магнит өрісінің индукциясына тәуелділігі алынған. Магнит өрісі градиентінің реакция шығысына әсері триплет-триплет жұптарындағы басқа белгілі спин-динамика механизмдерінде басым екені анықталды.

Кілт сөздер: триплет-триплеттік аннигиляция, ферромагниттік нанобөлшек, біртекті емес магнит өрісі, магниттік әсер.

Кучеренко М.Г., Неясов П.П.

Спин-селективное взаимодействие триплетно-возбужденных молекул на поверхности ферромагнитной наночастицы.

Изучено влияние магнитного поля, генерируемого ферромагнитной наночастицей, на аннигиляцию триплетно-возбужденных органических молекул или триплетных экситонов в приповерхностном слое частиц. Представлена подробная математическая модель, учитывающая диффузионную подвижность электронного возбуждения и геометрию системы. Кинетический оператор задан в полном базисе 9х9 спиновых состояний триплет-триплетной пары. Получены временные зависимости заселенности синглетного спинового состояния триплет-триплетной пары и зависимость профиля магнитного отклика при триплет-триплетной аннигиляции (эффект магнитной реакции) от индукции магнитного поля. Обнаружено, что влияние градиента магнитного поля на выход реакции доминирует над другими известными механизмами спин-динамики в триплет-триплетных парах

Ключевые слова: триплет-триплетная аннигиляция, ферромагнитная наночастица, неоднородное магнитное поле, магнитный эффект.

Волокитина И.Е., Найзабеков А.Б., Волокитин А.В.

Микроқосындыланған болат микроқұрылымының өзгеруіне жоғары қысым астындағы бұралудың әсері.

Бөлшектерді жасаудың ең көп таралған әдісі - металдарды қысым астында өңдеу болып табылады, оның нәтижесінде материалдың беріктігі мен иілімділігінің барлық резерві таусыла алмайды. Сондықтан пластикалық деформацияның поршеньдік сақиналардың циклдік беріктілігіне және төзімділік шектеріне әсері өзекті болып табылады. Берілген мақалада жаңа конструкция қалыбындағы микроқұрылым эволюциясына және механикалық қасиеттердің өзгеруіне жоғары қысым астындағы бұралудың әсерін эксперименттік зерттеулері жүргізілген. Нәтижесінде ультра ұсақ түйіршікті құрылымды қалыптастыру және болат сақиналардың беріктік қасиеттерін арттыру үшін ұсынылған әдісті қолданудың принципті мүмкіндігі және тиімділігі дәлелденген. Деформацияны қоршаған орта температурасында алты өту кезінде жүргізілді. Деформация нәтижесінде ультра ұсақ түйіршікті құрылым алынды, оның орташа түйіршік мөлшері 0,5 μm және үлкен бұрышты шекаралар сандары бар. Микроқосындылаған болаттың беріктік қасиеттері бастапқы күймен салыстырғанда шамамен 3 есе артты, микроқаттылық та 3 есе артты, яғни бастапқы күйдегі 760 МПа-дан деформациядан кейін 1935 МПа-ға дейін көтерілді. Мұнда беріктік қасиеттерінің ең үлкен артуы деформацияның алғашқы 3 циклінде бар болды.

Кілт сөздері: қарқынды пластикалық деформация, микроқұрылым, жоғары қысым астындағы бұралу, болат, механикалық қасиеттер.

Волокитина И.Е., Найзабеков А.Б., Волокитин А.В.

Влияние кручения под высоким давлением на изменение микроструктуры микролегированной стали.

Наиболее распространенным методом изготовления деталей является обработка металлов давлением, в результате которой не исчерпывается весь резерв прочности и пластичности материала. Поэтому вопросы влияния пластической деформации на циклическую долговечность и пределы выносливости поршневых колец являются актуальными. В данной статье проведены экспериментальные исследования влияния кручения под высоким давлением в штампе новой конструкции на эволюцию микроструктуры и изменение механических

свойств. В результате доказана принципиальная возможность и эффективность использования предложенного метода для формирования ультрамелкозернистой структуры и повышения прочностных свойств стальных колец. Деформацию проводили при температуре окружающей среды в шесть проходов. В результате деформирования получена ультрамелкозернистая структура со средним размером зерна 0,5 μm с наличием большого количества большеугловых границ. Прочностные свойства микролегированной стали возросли по сравнению с исходным состоянием почти в 3 раза, микротвердость также возросла в 3 раза, т.е. повысилась с 760 МПа в исходном состоянии до 1935 МПа после деформирования. При этом наибольший прирост прочностных свойств приходился на первые 3 цикла деформирования.
Ключевые слова: интенсивная пластическая деформация, микроструктура, кручение под высоким давлением, сталь, механические свойства.

Ашуров М.Х., Нуритдинов И., Джуманов С.Д., Саидахмедов К.Х.
Иондаушы сәулеленудің SNC стеатит керамикасының диффузды шағылу спектрлеріне әсері.
Берілген мақалада оптикалық спектроскопия әдісімен, яғни диффузды шағылу әдісімен 60Co көзінің гамма-сәулеленуінің жоғары дозаларымен және аралас реакторлық no-гамма-сәулеленумен сәулелендірілген SNC типті стеатиттік керамикадағы радиациялық ақаулар зерттелген. Диффузды шағылу спектрлерінің нәтижелерін талдау кейбір құрылымдық ақаулардың гамма-сәулелену кезінде пайда болатынын көрсетті. Бұл спектрдің ультракүлгін аймағында байланыспаған оттегі атомдарының және E1 орталықтары, (электронды ұстайтын үш үйлестірілген кремний атомы) бос орындар болып табылады. Спектрдің көрінетін аймағында кемтік орталықтарының түрлері әр түрлі байқалған. Көрінетін спектр аймағында спектрді гауссиандарға жіктегеннен кейін спектрдің бұл аймағында гамма-сәулеленумен салыстырғанда кемтік орталықтарының (O-ME, me-металл) әр түрлі типтері қосымша түзілетіні анықталды. No-гамма-сәулелену реакторында мұндай құрылымдық ақауларды алу тиімділігі гамма-сәулеленумен сәулелендірілген үлгілермен салыстырғанда жоғары болды.
Кілт сөздері: SNC типті стеатит керамикасы, диффузиялық шағылу, гамма-сәулелену, no-гамма-сәулелену, V типті кемтік орталықтары.

Ашуров М.Х., Нуритдинов И., Джуманов С.Д., Саидахмедов К.Х.
Влияние ионизирующего излучения на спектры диффузного отражения стеатитовой керамики SNC.
В данной статье методом оптической спектроскопии, т.е. методом диффузного отражения, исследованы радиационные дефекты, в стеатитовой керамике типа SNC, облученной высокими дозами гамма-излучения источника 60Co и смешанного реакторного no-гамма-облучения. Анализ результатов спектров диффузного отражения показал, что некоторые структурные дефекты образуются при гамма-облучении. Это кислородные вакансии, несвязанные атомы кислорода и E1-центры (трехкоординированный атом кремния, захвативший электрон) в ультрафиолетовой области спектра. В видимой области спектра различны типы дырочных центров. После разложения спектра видимой области на гауссианы было обнаружено, что в этой области спектра, по сравнению с гамма-облучением, дополнительно образуются различные типы дырочных центров - (O-Me, Me-металл). Эффективность создания этих структурных дефектов при реакторном no-гамма-облучении, была выше по сравнению с образцами, облученными гамма-излучением.
Ключевые слова: стеатитовая керамика типа SNC, диффузное отражение, гамма-излучение, no-гамма-облучения, дырочные центры V-типа.

Сериков Т.М., Балтабеков А.С., Айдарова Д.Д., Жанбирбаева П.А., Куанышбекова А.Б.
Титан диоксиді нанотүтікшелерінен түзілген қабықшалардың фотокаталитикалық белсенділігіне анодтау кернеуінің әсері.
Синтез кезінде анодтау кернеуінің бетінің меншікті аймағына және TiO_2 нанотүтікшесінің фотокаталитикалық белсенділігіне әсері зерттелген. Титан диоксиді нанотүтікшелерінен түзілген қабықшалар титан фольгасының бетінде электрхимиялық анодтау әдісімен алынды. Анодтау кернеуінің 20 В-тан 60 В-қа дейін жоғарылауы нанотүтікшелердің ішкі және сыртқы диаметрлерінің артуына, өсу жылдамдығының жоғарылауына және нанотүтікшелердің кеуектері арасындағы қашықтыққа әкелетіні анықталды. Үлгілердің фотокаталитикалық белсенділігі фотоиндукцияланған тоқтың шамасын өлшеу арқылы бағаланған. Төмен кернеуде алынған қабықша жоғары кернеуде алынған қабықшадан 3,5 есе көп тоқ шығарды, ал қабықшалардың қатысуымен бояғыштың ыдырауы сол уақыт аралығында сәйкесінше 75 және 38% құрады. Қабықшалардың фотокаталитикалық белсенділігінің артуы негізінен нанотүтікшелердің беткі қабатының ұлғаюымен байланысты. Осылайша, TiO_2 нанотүтікшелерінің нақты бетінің мәндері азотты төмен температурада адсорбциялау әдісімен анықталды. Анодтау кернеуінің жоғарылауымен қабықшалар бетінің нақты ауданы азаятыны анықталды.
Кілт сөздері: нанотүтікше, титан диоксиді, фотокатализ, меншікті бетінің ауданы, судың бөлінуі.

Сериков Т.М., Балтабеков А.С., Айдарова Д.Д., Жанбирбаева П.А., Куанышбекова А.Б.
Влияние напряжения анодирования на фотокаталитическую активность пленок, формированных нанотрубками диоксида титана.
Исследовано влияние напряжения анодирования при синтезе на удельную площадь поверхности и на фотокаталитическую активность нанотрубок диоксида титана TiO2. Методом электрохимического анодирования на поверхности титановой фольги были получены пленки, образованные нанотрубками TiO_2. Установлено, что увеличение напряжения анодирования от 20 В до 60 В приводит к росту внутреннего и внешнего диаметров нанотрубок, увеличению скорости роста и межпорового расстояния нанотрубок. Фотокаталитическая активность образцов оценивалась по измерению величины фотоиндуцированного тока. Пленка, полученная при низком напряжении, генерировала ток в 3,5 раза выше, чем пленка, полученная при высоком напряжении, а деградация красителя в присутствии пленок составила 75 и 38 % соответственно за одинаковый период времени. Повышение фотокаталитической активности пленок преимущественно связан с ростом величины удельной площади поверхности нанотрубок. Так, методом низкотемпературной адсорбции азота определены величины удельной площади поверхности нанотрубок TiO_2. Установлено, что с ростом напряжения анодирования удельная площадь поверхности пленок уменьшается.
Ключевые слова: нанотрубка, диоксид титана, фотокатализ, удельная площадь поверхности, расщепление воды.

Рогалев Н.Д., Рогалев А.Н., Киндра В.О., Злывко О.В., Брызгунов П.А.
Қолданыстағы және перспективтік жылу электр станцияларының көміртегі ізін салыстырмалы талдау.
Отын - энергетика секторы ғаламдық жылынуға үлесін қосатын жылыжай газдардың ең ірі эмитенті болып табылады. Олардың эмиссиясы отынды өндіру, тасымалдау және жағу кезінде жүзеге асырылады. Өндіруші объектілерді пайдалану кезінде шығарындыларды азайтудың перспективті тәсілі – көміртегі диоксидінің аз шығарындыларына ие органикалық отында жұмыс істейтін энергиялық қондырғыларға көшу болып табылады. Алайда, көмірқышқыл газын ұстауға жұмсалатын энергия шығындарының бар болуы мұндай энергия қондырғыларының тиімділігінің айтарлықтай төмендеуіне әкеледі. Ақырында, бұл отынды тұтынудың жоғарылауына және жылыжай газдарының шығарындыларының өсуіне әкеледі: ең алдымен, отын өндіру көлемдерінің және тасымалдаудың ұлғаюымен байланысты. Берілген жұмыста материалдық теңгерім әдісі негізінде тұтынылатын отынның тиімділігі мен мөлшерінің өзгеруінің жүйелік әсерін ескере отырып, табиғи газда да, ішкі циклдік газдандырумен көмірде де жұмыс істейтін бу-газ және оттегі-отын қондырғылары үшін жиырма жылдық өмірлік цикл ішінде көміртегі ізінің бағалауы жүргізілген. Оттегі - отын электр станцияларына ауысу көміртегі ізін табиғи газбен жұмыс істеу жағдайынмен салыстырғанда шамамен 90%-ға және көмір отыны жағдайымен салыстырғанда шамамен 75%-ға төмендетуге мүмкіндік беретіні көрсетілген. Зерттеу сонымен қатар көмірқышқыл газын ұстау және сақтау жүйесін енгізудің оң әсерін көрсетті: көміртегі ізін табиғи газ үшін шамамен 75% -ға және көмір үшін 70%-ға азайған.
Кілт сөздері: көміртегі ізі, жылу электр станциялары, БҒҚ, Аллам циклі, органикалық отын, көмірді газдандыру.

Рогалев Н.Д., Рогалев А.Н., Киндра В.О., Злывко О.В., Брызгунов П.А.
Сравнительный анализ углеродного следа существующих и перспективных тепловых электрических станций
Топливно-энергетический сектор является крупнейшим эмитентом парниковых газов, вносящих вклад в глобальное потепление. Их эмиссия осуществляется при добыче, транспортировке и сжигании топлив. Перспективным способом снижения выбросов при эксплуатации генерирующих объектов является переход к энергетическим установкам на органическом топливе с малыми выбросами диоксида углерода. Однако наличие затрат энергии на улавливание углекислого газа приводит к существенному снижению эффективности данных энергоустановок. В конечном счете это приводит к повышенному потреблению топлива и росту эмиссии парниковых газов: прежде всего, за счет увеличенных объемов добычи и транспортировки топлива. В настоящей работе на основе метода материального баланса, с учетом системного эффекта изменения эффективности и количества потребляемого топлива, произведена оценка углеродного следа в течение двадцатилетнего жизненного цикла для парогазовых и кислородно-топливных установок, работающих как на природном газе, так и на угле с внутрицикловой газификацией. Показано, что переход на кислородно-топливные энергоустановки позволяет снизить углеродный след примерно на 90 % в случае работы на природном газе и около 75 % для угольного топлива. Исследование также демонстрирует положительный эффект внедрения системы улавливания и хранения диоксида углерода: сокращение углеродного следа примерно на 75% для природного газа и на 70% для угля.
Ключевые слова: углеродный след, тепловые электрические станции, ПГУ, цикл Аллама, органическое топливо, газификация угля.

Турсунов М.Н., Сабиров К., Абилфазиев Ш.Н., Юлдошов Б.А.

Әртүрлі материалдардан жасалған фотоэлектрлік және фототермиялық батареяларды сынау.

Дүние жүзінде соңғы жылдары көмірсутек ресурстарын пайдалану қысқаруда және олардың орнын экологиялық таза баламалы және жаңартылатын энергия көздері алмастырылуда. Сондықтан фотоэлектрлік батареяларға негізделген құрылғыларды жетілдіруге көп көңіл бөлінеді. Бұл бағытта мақсатты ғылыми зерттеулер жүргізу қазіргі заманның өзекті мәселелерінің бірі болып табылады. Мақалада табиғи жағдайда пайдаланылған кезде фотоэлектрлік және фототермиялық батареялардың электрлік параметрлерін салыстыру нәтижелері келтірілген. Тәжірибелер әр түрлі материалдардан жасалған және әр түрлі конструкциялы үш дәстүрлі фотоэлектрлік батареялар мен фототермиялық батареяларда жүргізілген. Бүкіл батареялар мобильді конструкцияға орнатылған, ал аккумуляторлардың байланыстыратын құрылғының ұзын жағында күн сәулесін шағылдыратын екі жазықтық (рефлекторлар) орнастырылған. Дәл осындай жағдайларда күн сәулеленуінің қарқындылығы фотоэлектрлік және фототермальді батареяларына жарықты қайтаратын рефлекторлардың көмегімен арттырылады. Фотоэлектрлік батареялардың алдыңғы бетінде күн сәулесінің тік (90º) түсуі қарастырылған. Материалдың түріне және конструкциясына байланысты сыналатын батареялардың электрлік параметрлерінің әр түрлі мәндері алынған. Дәстүрлі фотоэлектрлік батареялармен салыстырғанда фототермиялық батареялар материалдың түріне байланысты 1,3-1,4 есе көп электр энергиясын өндірді. Эксперимент нәтижесінде ыстық климат жағдайында жұмыс істейтін фотоэлектрлік және фототермиялық батареялардың бос жүрістің кернеуі, қысқа тұйықталу тоғы және қуаты туралы мәліметтер алынған. Нәтижелерге сәйкес, электр параметрлері бойынша жоғары көрсеткіштерді монокристалдар негізіндегі фотоэлектрлік және фототермиялық батареялар көрсетті.

Кілт сөздері: монокристалл, поликристалл, фототермиялық, мобильді құрылғы, жылу коллекторы, ұялы поликарбонат, бос жүріс кернеуі, қысқа тұйықталу тоғы.

Турсунов М.Н., Сабиров К., Абилфазиев Ш.Н., Юлдошов Б.А.

Испытания фотоэлектрических и фототермальных батарей из различных материалов.

Во всем мире последние годы сокращается использование углеводородных ресурсов, а их место заменяют экологически чистые альтернативные и возобновляемые источники энергии. Поэтому большое внимание уделяется усовершенствованию устройств на основе фотоэлектрических батарей. Проведение целевых научных исследований в этом направлении является одним из актуальных вопросов настоящего времени. В статье представлены результаты сравнения электрических параметров фотоэлектрических и фототермических батарей при использовании в естественных условиях. Эксперименты проводились на трех традиционных фотоэлектрических батареях и фототермических батареях, изготовленными из разных материалами и с различными конструкциями. Все аккумуляторы установлены в мобильной конструкции, а вдоль длинной стороны устройства, соединяющего аккумуляторы, установлены две плоскости (рефлектора), отражающие солнечный свет. В таких же условиях интенсивность солнечного излучения увеличивается с помощью рефлекторов, возвращающих свет к фотоэлектрическим и фототепловым батареям. На лицевой поверхности фотоэлектрических батарей предусмотрено вертикальное (90º) падение солнечных лучей. Получены различные значения электрических параметров испытываемых батарей в зависимости от типа материала и конструкции. По сравнению с традиционными фотоэлектрическими батареями фототермические батареи производили в 1.3-1.4 раза больше электроэнергии в зависимости от типа материала. В результате эксперимента получены данные о напряжении холостого хода, токе короткого замыкания и мощности фотоэлектрических и фототермических батарей в условиях жаркого климата. Согласно результатам, высокие показатели по электрическим параметрам имеют монокристаллические фотоэлектрические и фототермические батареи, изготовленные на их основе.

Ключевые слова: монокристалл, поликристалл, фототермальный, мобильное устройство, коллектор тепла, сотовый поликарбонат, напряжение холостого хода, ток короткого замыкания.

Ермачихин А.В., Литвинов В.Г., Холомина Т.А., Маслов А.Д., Трусов Е.П.

Электрондық техниканың элементтері мен құрылымдарындағы төмен жиілікті шу спектрінің температураға тәуелділігін зерттеуге арналған өлшеуіш кешені.

Берілген жұмыста төмен жиілікті шу спектроскопиясына арналған өлшеуіш - аналитикалық кешен ұсынылған. Өлшеуіг кешен электронды элементтердегі, компоненттердегі және жартылай өткізгіш материалдар мен құрылымдардағы төмен жиілікті шу спектрлерін автоматтандырылған зерттеулерге бейімделген. Ұсынылған өлшеуіш жүйесінің ерекшелігі - үлгідегі төмен жиілікті шу спектрлерінің электр кернеуі мен температурасына тәуелділігін автоматты түрде кешенді және нақты зерттеу. Жиіліктер диапазоны 0,001-10000 Гц, ығысудың тұрақты кернеу диапазоны 0-50 В және температура диапазоны 7-500 К. Өлшеуіш кешені электронды материалдар мен құрылымдардың шу сиаттамаларының жергілікті өлшеулер үшін атомдық күштік микроскопымен жұмыс істеуге бейімделген. Өлшеу кешенінің көмегімен эксперименттік мәліметтердің үлкен көлемін алуға болады, бұл зерттелетін үлгіде шудың пайда болу механизмдері мен себептері туралы жан-жақты қорытынды жасауға мүмкіндік береді. Шоттқидің диодтық құрылымын зерттеу мысалында өлшеуіш кешеннің жұмысын тексеру нәтижелері келтірілген.

Кілт сөздері: төмен жиілікті шу спектроскопиясы; температуралық өлшеулер; өлшеуді автоматтандыру; тосқауыл құрылымдары; атомдық-күштік микроскопия.

Ермачихин А.В., Литвинов В.Г., Холомина Т.А., Маслов А.Д., Трусов Е.П.
Измерительный комплекс для исследований температурной зависимости спектра низкочастотного шума в элементах и структурах электронной техники.
В данной работе представлен измерительно-аналитический комплекс для спектроскопии низкочастотных шумов. Измерительный комплекс адаптирован для автоматизированного исследования спектров низкочастотных шумов в электронных элементах, компонентах и полупроводниковых материалах и структурах. Отличительной характеристикой предлагаемой измерительной системы является автоматизированное комплексное и прецизионное исследование зависимости спектров низкочастотного шума в образце от электрического напряжения и температуры. Диапазон частот 0,001-10000 Гц, диапазон постоянного напряжения смещения 0-50 В и диапазон температур 7-500 К. Измерительный комплекс адаптирован для работы с атомно-силовым микроскопом для локальных измерений шумовых характеристик электронных материалов и структур. С помощью измерительного комплекса можно получить больший объем экспериментальных данных, что позволяет сделать всеобъемлющие выводы о механизмах и причинах генерации шума в исследуемом образце. Приведены результаты проверки работы измерительного комплекса на примере исследования диодной структуры Шоттки.
Ключевые слова: спектроскопия низкочастотных шумов; температурные измерения; автоматизация измерений; барьерные структуры; атомно-силовая микроскопия.

Алипбаев К.А., Сарсенбаев Е.Е., Мусина А.А., Нұрғизат Е.С.
Наносеріктерді басқарудың борттық кешенінің архитектурасын әзірлеу.
Берілген мақалада борттық басқару кешенінің архитектурасын әзірлеу ұсынылған. Атап айтқанда, модульді әзірлеуде аппараттық және схемотехникалық шешімдер ұсынылған. Сонымен қатар, техникалық шешімдер, борттық басқару кешенінің механикалық құрылымының тұжырымдамасы, сервистер мен қосымшалардың деңгейі, борттық кешеннің ұсынылған модульдерінің блок-сұлбалары талқыланады. Өте шағын жасанды серіктерді жобалауға және дамытуға көмектесетін борттық бағдарламалық жасақтаманың негізгі функциялары егжей-тегжейлі сипатталған. Бұл мақала борттық басқару жүйесін тиімді реттеу және пайдалану тәсілі ретінде қызмет етеді.
Кілт сөздері: борттық компьютер, кубсат, бағдарламалық жасақтамамен анықталған радиожүйесі, бағдарламаланатын логикалық интегралды сұлба.

Алипбаев К.А., Сарсенбаев Е.Е., Мусина А.А., Нұрғизат Е.С.
Разработка архитектуры бортового комплекса управления наноспутниками.
В данной статье представлена разработка архитектуры бортового комплекса управления. В частности, представлены аппаратные и схемотехнические решения в разработке модуля. Также обсуждаются технические решения, концепция механической компоновки бортового комплекса управления, уровень сервисов и приложений, блок-схемы представленных модулей бортового комплекса. Подробно описаны основные функции бортового программного обеспечения, которое поможет в проектировании и разработке сверхмалых искусственных спутников. Эта статья служит подходом к эффективной настройке и эксплуатации бортовой системы управления.
Ключевые слова: бортовой компьютер, кубсат, программно-определяемая радиосистема, программируемая логическая интегральная схема.

Шаихова Г.С., Беломестный Д., Копбалина К.Б.
Қатты дене механикасының әдістерімен кен қазбаларының кернеулік күйін деформацияланатын арқылы зерттеу.
Кен қазбаларының кернеулік күйін ескеруімен тау-кен технологиялық сұлбасының сенімділігін бағалауы тау-кен геологиялық, техникалық және технологиялық факторлардың жиынтығына байланысты. Мақалада деформацияланатын қатты дене механикасының заманауи әдістері негізінде тау-кен массивінің моделі және кернеулік күйді есептеудің сұлбалары келтірілген. Зерттеу нысаны ретінде көмір қабатына параллель болатын ұзындығы үлкен таужыныстары арқылы өтетін, тау қысымы аймағындағы жалғыз қазба (далалық штрек) қарастырылған. Көмір тақтасы қабаттың төмендеуі бойынша ұзын бағандармен алынады. Далалық штрек тақтаның табан жыныстарында орналасқандықтан және тазарту жұмыстары әсер ететін аймақта болғандықтан негізгі жүктеме тақтаға әсер ететін тірек қысымы болып табылады. Қолданбалы есептерді шешу кезінде интегралды теңдеулердің кешенді потенциалдарының әдістерін және олардың комбинацияларын тиімді қолдану салаларын анықталған. Шахталық (табиғи) өлшеулер мен бақылаулар, зертханалық эксперименттер мен оларды жалпылауды міндетті түрде пайдалануды және шекаралық жағдайларды белгілеу кезінде де, шешу барысында алынған нәтижелерді тексеру кезінде де ескеріледі. Бұл үшін бойлық осьтің бойымен өзгеретін

жартылай жолақтарда түйіспелі кернеу туралы серпімділік теориясының аралас есебі шешілгені; бұл жартылай борттар қабаттық жартылай қабаттар арасындағы үйкеліс қысылған кезде, бүйірден, деформативті қасиеттер.
Кілт сөздері: массив, кернеу, модель, көмір қыртысы, интегралдау тораптары, шекаралық интегралды теңдеулер әдісі, қысым.

Шаихова Г.С., Беломестный Д., Копбалина К. Б
Исследование напряженного состояния горных выработок с использованием методов механики деформируемого твердого тела.
Оценка надежности горно-технологической схемы с учетом напряженного состояния горных выработок зависит от совокупности горно-геологических, технических и технологических факторов. В статье показано создание модели массива горных пород и схемы расчета напряженного состояния на основе современных методов механики деформируемого твердого тела. Объектом исследования является одиночная горная выработка большой протяженности, пройденная в породе параллельно простиранию угольного пласта (промысловому штреку) и находящимся в зоне влияния крепи. В связи с тем, что полевой штрек закладывается в грунте пласта, представляющего собой слоистую толщу в зоне влияния очистных работ, преобладающей нагрузкой является опорное давление на пласт. Определены области применения методов комплексных потенциалов интегральных уравнений и их комбинаций при решении прикладных задач. Данные шахтных (полевых) измерений и наблюдений, лабораторных экспериментов и их обобщения учитываются как при постановке задач и постановке граничных условий, так и при проверке полученных результатов. Решена смешанная задача теории упругости о контактном напряжении на полуполосах, изменяющемся вдоль продольной оси; отходя от концов, деформационные свойства при зажатии этих полуполос с трением между слоистыми полуплоскостями.
Ключевые слова: массив, напряжения, модель, угольный пласт, узлы интегрирования, метод граничных интегральных уравнений, давление.

Ибраев Н.Х., Селиверстова Е.В., Канапина А.Е.
Әр түрлі диаметрлі алтын нанобөлшектерінің ауыспалы жұтылуы.
Орташа диаметрі 13±5 және 48±16 нм болатын алтын нанобөлшектерінің наносекундты лазерлік импульстармен фотоқоздыру кезіндегі ауыспалы жұтылуы зерттелген. Стационарлық жұтылу максимумы шамамен 520–540 нм максимуммен кең құрылымсыз жолақпен ұсынылғаны көрсетілген. Максимумы шамамен 430 нм болатын Au нанобөлшектерінің ауыспалы жұтылу жолағы 6–8 нм максимум жиілігімен жұқа құрылымға ие және нанобөлшектердің өлшеміне тәуелді емес. Нанобөлшектердің жұтылу ұзақтығы нанобөлшектің орташа өлшемдерінің төмендеуімен азаяды. Ауыспалы жұтылудың өмір сүру ұзақтығы үлкен және кіші бөлшектер үшін сәйкесінше 23±2 – 19,5±2 нс құрайды. Au нанобөлшеігнің ауыспалы жұтылуының наносекундтық ұзақтығы қоршаған ортамен жылу алмасудың тежелуінің көрінісі ретінде «алтын нанобөлшек – еріткіш молекуласының интерфейсі» жүйесіндегі ұзаққа созылған релаксация процесінің нәтижесі болып табылады.
Кілт сөздері: алтын нанобөлшектері, плазмон, өлшем, ауыспалы жұтылу, оптикалық қасиеттер.

Ибраев Н.Х., Селиверстова Е.В., Канапина А.Е.
Переходное поглощение наночастиц золота различного диаметра.
Изучено переходное поглощение наночастиц золота со средним диаметром 13±5 и 48±16 нм при фотовозбуждении лазерными импульсами наносекундной длительности. Показано, что максимум стационарного поглощения представлен широкой бесструктурной полосой с максимумом около 520–540 нм. Полоса переходного поглощения наночастиц Au с максимумом около 430 нм имеет тонкую структуру с периодичностью максимумов 6-8 нм и не зависит от размера наночастиц. Длительность поглощения сокращается с уменьшением среднего размера наночастиц. Время жизни переходного поглощения составляет 23±2-19,5±2 нс для больших и малых частиц, соответственно. Наносекундная длительность переходного полощения наночастиц Au является результатом затянутого релаксационного процесса в системе «интерфейс наночастица золота – молекулы растворителя» как проявление затрудненного теплообмена с окружающей средой.
Ключевые слова: наночастицы золота, плазмон, размер, переходное поглощение, оптические свойства.

Inyang E.P., Obisung E.O., Amajama J., Bassey D E., William E.S., Okon I.B.
Топологиялық ақаудың ауыр және жеңіл кварконий масс-спектрлеріне әсері.
Берілген зерттеуде топологиялық ақаудың чармоний, боттомоний және шарм-стрэндж, боттомчарм сияқты ауыр және ауыр-жеңіл мезондардың масс-спектрлеріне әсері сәйкесінше Хултен плюс Юкава потенциалы арқылы зерттелген. Шредингер теңдеуі аналитикалық түрде Никифоров-Уваров әдісімен шешілді. Энергиялық спектрдің және нормалданбаған толқындық функцияның жуық шешімдері алынды. Нәтижелер әртүрлі

кванттық күйлер үшін топологиялық ақау болған және болмаған кезде ауыр және ауыр жеңіл мезондардың масс-спектрлерін болжау үшін қолданылады. Топологиялық ақау артқан кезде масс-спектрлер ығысып, олардың мәндері эксперименттік мәліметтерге жақындайтыны анықталды. Алайда, басқа зерттеушілердің жұмысымен салыстырғанда, нәтижелер масс-спектрлерді сипаттау үшін жетілдірілген шешімді көрсетті.
Кілт сөздері: Шредингер теңдеуі, Никифоров-Уваров әдісі, Хултен-Юкава потенциалы, масс-спектрлер, топологиялық ақау.

Inyang E.P., Obisung E.O., Amajama J., Bassey D E., William E.S., Okon I.B.
Влияние топологического дефекта на масс-спектры тяжелых и легких кварконий.
В настоящем исследовании влияние топологического дефекта на масс-спектры тяжелых и тяжелых-легких мезонов, таких как чармоний, боттомоний и шарм-стрэндж, боттом-чарм, соответственно, изучается с помощью потенциала Хюльтена плюс Юкавы. Уравнение Шрёдингера решается аналитически методом Никифорова-Уварова. Получены приближенные решения энергетического спектра и ненормированной волновой функции. Полученные результаты применены для предсказания масс-спектров тяжелых и тяжело-легких мезонов при наличии и отсутствии топологического дефекта для различных квантовых состояний. Установлено, что при увеличении топологического дефекта масс-спектры смещаются и ихзначения приближаются к экспериментальным данным. Однако, по сравнению с работой других исследователей, результаты показали улучшенное решение для описания масс-спектров.
Ключевые слова: уравнение Шрёдингера, метод Никифорова-Уварова, потенциал Хультена-Юкавы, масс-спектры, топологический дефект.

INFORMATION ABOUT AUTHORS | **АВТОРЛАР ТУРАЛЫ МӘЛІМЕТТЕР** | **СВЕДЕНИЯ ОБ АВТОРАХ**

Abilfayziyev, Sh.N. - PhD student, Termez State University, Termez, Uzbekistan, ORCID iD: 0000-0002-5273-1206**;** abilfayziyev@inbox.ru

Aidarova, D.D. – Master student, E.A. Buketov Karaganda University, Karaganda, Kazakhstan; dariga_1810@mail.ru

Alipbayev, K.A. – PhD, Head of the "Space Technics and Technology" Department, Almaty University of Power Engineering and Telecommunications named after G. Daukeev, Almaty, Kazakhstan; Scopus Author ID: 56514120200; ORCID iD: 0000-0003-1652-9470; k.alipbayev@aues.kz

Amajama, J. – PhD (Phys.), Lecturer, Department of Physics, University of Calabar, Calabar, Nigeria; ORCID iD: 0000-0002-8475-9457; joeamajama@unical.edu.ng

Ashurov, M.K. – Doctor of phys.-math. sciences, Professor, Chief Researcher, Laboratory of Radiation Physics of Optical Phenomen, Institute of Nuclear Physics Academy Sciences of Uzbekistan, Tashkent, Uzbekistan; Scopus Author ID: 670146329; ashurov49@mail.ru

Baltabekov, A.S. – PhD, Associate Professor, E.A. Buketov Karaganda University, Karaganda, Kazakhstan; Scopus Author ID: 35193461600; ORCID iD: 0000-0001-8829-2527; abskargu@mail.ru

Bassey, D.E. – PhD (Phys.), Professor, Department of Physics, University of Calabar, Calabar, Nigeria; basseyde@yahoo.com

Belomestny, **D.V. –** PhD, Professor, University of Duisburg-Essen, Duisburg, Germany; Scopus Author ID: 15069577900; ORCID iD: 0000-0002-9482-6430; denis.belomestny@uni-due.de

Bryzgunov, P.A. – PhD student**,** National Research University “Moscow Power Engineering Institute", Moscow, Russian Federation; Scopus author ID: 57844836600; ORCID iD: 0000-0003-3710-5116; BryzgunovPA@mpei.ru

Dzhumanov, S. – Doctor of phys.-math. sciences, Professor, Chief Researcher, Laboratory of Physics of Nanostructured and Superconducting Materials, Institute of Nuclear Physics of the Uzbekistan Academy of Sciences, Tashkent, Uzbekistan; Scopus Author ID: 6603519344; WoS Researcher ID: ABI-2933-2020; dzhumanov@inp.uz

Ermachikhin, A.V. – PhD, Associate Professor, Ryazan State Radio Engineering University named after V.F. Utkin, Ryazan, Russia; Scopus Author ID: 55948342500; ORCID iD: 0000-0002-3808-9691; al.erm@mail.ru

Ibrayev, N.Kh. - Doctor of phys.-math. sciences, Professor, Director of the Institute of Molecular Nanophotonics, E.A. Buketov Karaganda University, Kazakhstan; Scopus Author ID: 9333698600, ORCID iD: 0000-0002-5156-5015, niazibrayev@mail.ru

Inyang, E.P. – PhD (Theoretical Nuclear Phys.), Professor, Department of Physics, National Open University of Nigeria, Jabi-Abuja, Nigeria; Scopus Author ID: 16175170000; ORCID iD: 0000-0002-5031-3297; einyang@noun.edu.ng

Kanapina, A.E. – PhD student, E.A. Buketov Karaganda University, Kazakhstan; Scopus Author ID 57226236798, ORCID iD: 0000-0001-7819-4667; asselkanapina@mail.ru

Kholomina, T.A. – Doctor of phys.-math. sciences, Full Professor, Ryazan State Radio Engineering University named after V.F. Utkin, Ryazan, Russia; Scopus Author ID: 6507925868; ORCID iD: 0000-0003-3902-618X; marta.tap@yandex.ru

Kindra, V.O. - Candidate of techn. sciences, Associate Professor, National Research University "Moscow Power Engineering Institute", Moscow, Russian Federation; Scopus author ID: 57023993700; ORCID iD: 0000-0002-8406-7901; KindraVO@mpei.ru

Kopbalina K.B – Master (Phys.), Senior Lecturer, A. Saginov Karaganda Technical University, Karaganda, Kazakhstan; Scopus Author ID: 56167615600**;** ORCID iD: 0000-0001-6378-9756; kopbalina82@mail.ru

Kuanyshbekova, A.B. - Master, E.A. Buketov Karaganda University, Karaganda, Kazakhstan; kuanyshbekovaaya@mail.ru

Kucherenko, M.G. – Doctor of phys.-math. sciences, Professor, Director of the Center for Laser and Informational Biophysics, Orenburg State University, Orenburg, Russia; Scopus Author ID: 7003581468; WoS Researcher ID: E-9515-2015; ORCID iD: 0000-0001-8821 -2427; clibph@yandex.ru

Litvinov, V.G. - Doctor of phys.-math. sciences, Associate Professor, Head of Micro- and nanoelectronics Department; Ryazan State Radio Engineering University named after V.F. Utkin, Ryazan, Russia; Scopus Author ID: 7201710127; ORCID iD: 0000-0001-6122-8525; vglit@yandex.ru

Maslov, A.D. – PhD, Senior Researcher, Ryazan State Radio Engineering University named after V.F. Utkin, Ryazan, Russia; Scopus Author ID: 56825275500; ORCID iD: 0000-0002-4056-1510; maslov.a.d@mail.ru

Mussina, A.A. - Master (Eng.), Lead Design Engineer, Ghalam LLP, Astana, Kazakhstan; a.mussina@ghalam.kz

Naizabekov, A.B. - Doctor of techn. sciences, Professor, Rector of the Rudny Industrial Institute, Rudny, Kazakhstan; Scopus Author ID: 56991079700; ORCID: 0000-0002-8517-3482

Neyasov, P.P. – PhD student, Center for Laser and Informational Biophysics, Orenburg State University, Orenburg, Russia; Scopus Author ID: 57222337052; ORCID iD: 0000-0002-7133-8741; nejapetr@yandex.ru

Nurgizat, Ye.S. – PhD, Senior Lecturer, Almaty University of Energy and Communications named after G. Daukeev, Almaty, Kazakhstan; y.nurgizat@aues.kz

Nuritdinov, I. – Doctor of phys.-math. sciences, Professor, Chief Researcher, Laboratory of Radiation Physics of Optical Phenomen, Institute of Nuclear Physics Academy Sciences of Uzbekistan, Tashkent, Uzbekistan; Scopus Author ID: 6601992720; izzatilloh/@yahoo.com

Obisung, E.O. – PhD (Phys.), Senior Lecturer, Department of Physics, University of Calabar, Calabar, Nigeria; effiongokokonobisung@gmail.com

Okon I.B. – PhD (Phys.), Senior Lecturer, Department of Physics, University of UYO, Nigeria; Scopus Author ID: 56465005800; ORCID iD: 0000-0002-8172-7249; ituenokon@uniuyo.edu.ng

Rogalev, A.N. - Doctor of techn. sciences, Professor, National Research University "Moscow Power Engineering Institute", Moscow, Russian Federation; Scopus author ID: 34980078500; ORCID iD: 0000-0001-7256-0144

Rogalev, N.D. - Doctor of techn. sciences, Professor, National Research University "Moscow Power Engineering Institute", Moscow, Russian Federation; Scopus author ID: 6507029432; ORCID iD: 0000-0002-6458-2869

Sabirov, X. - Candidate of techn. sciences, Associate Professor, Physical-Technical Institute, Academy of Sciences of Uzbekistan, Tashkent, Uzbekistan; ORCID iD:0000-0001-9193-6397; sabirovhabibullo54@gmail.com

Saidakhmedov, K.Kh. – PhD, Senior Researcher, Head of the Laboratory Radiation Physics of Optical Phenomen, Institute of Nuclear Physics Academy Sciences of Uzbekistan, Tashkent, Uzbekistan; Scopus Author ID: 6508071013; skahramon@yandex.ru

Sarsenbayev, Y.Y. – Master (Eng.), Lead Design Engineer, Ghalam LLP, Astana, Kazakhstan; y.sarsenbayev@ghalam.kz

Seliverstova, E. – PhD, Senior Researcher, Institute of Molecular Nanophotonics, E.A. Buketov Karaganda University, Kazakhstan; Scopus Author ID: 35323255400, ORCID iD: 0000-0002-9507-8825, genia_sv@mail.ru

Serikov, T.M. – PhD, Associate Professor, E.A. Buketov Karaganda University, Karaganda, Kazakhstan; Scopus Author ID: 56669712000; ORCID iD: 0000-0003-4302-9674; serikov-timur@mail.ru

Shaikhova, G.S. – Candidate of techn. sciences, acting Associate Professor, A.Saginov Karaganda Technical University, Karaganda, Kazakhstan; Scopus AuthorID: 57218284243; ORCID iD: 0000-0002-2036-3023; shaikxova_2011@mail.ru

Trusov, E.P. – PhD student, Ryazan State Radio Engineering University named after V.F. Utkin, Ryazan, Russia; Scopus Author ID:57203150591; ORCID iD: 0000-0003-1239-2702; eptrusov@yandex.ru

Tursunov, M.N. - Doctor of techn. sciences, Professor, Physical-Technical Institute, Academy of Sciences of Uzbekistan, Tashkent, Uzbekistan; ORCID iD: 0000-0001-5984-9568; muhammadtursunov1947@gmail.com

Volokitin, A.V. – PhD, Associate Professor, Metal Processing by Pressure Department, Karaganda Industrial University, Temirtau, Kazakhstan; Scopus Author ID: 56524247500; Researcher ID: U-8580-2018; ORCID: 0000-0002-0886-3578

Volokitina, I.E. – PhD, Associate Professor, Department of Metallurgy and Mining, Rudny Industrial Institute, Rudny, Kazakhstan; Scopus Author ID: 55902810800; Researcher ID: G-4526-2018; ORCID: 0000-0002-2190-5672

William, E.S. – PhD (Phys.), Professor, Department of Physics, University of Calabar, Calabar, Nigeria; Scopus Author ID: 57221313665; ORCID iD: 0000-0002-5247-5281; williameddyphysics@gmail.com

Yuldoshov, B.A. - PhD student, Termez State University, Termez, Uzbekistan, ORCID iD: 0000-0001-6614-6596; b.yuldoshov10@mail.ru

Zhanbirbayeva, P.A. - Master student, E.A. Buketov Karaganda University, Karaganda, Kazakhstan; ORCID iD: 0000-0002-9351-956X; perizat.zhanbirbaeva@mail.ru

Zlyvko, O.V. - Candidate of econom. sciences, Associate Professor, National Research University "Moscow Power Engineering Institute", Moscow, Russian Federation; Scopus author ID: 57060525900; ZlyvkoOV@mpei.ru

GUIDELINES FOR AUTHORS

Eurasian Physical Technical Journal (Eurasian phys. tech. j.) is a peer-reviewed open access international scientific journal publishing original research results on actual problems of technical physics and other related fields. Since 2004 «Eurasian phys. tech. j.» is published in English.

Acceptance of the manuscript for publication in the Eurasian phys. tech. j. is carried out online through website - https://phtj.buketov.edu.kz/index.php/EPTJ. Authors should check that their submissions meet all of the following requirements, as submissions may be returned to authors that do not comply with these guidelines.

Scientific article topic and content

A scientific article should contain the results of original scientific research previously unpublished and not intended for publication in other publications.

Manuscript of the article should contain at least 75% of the original text.

All articles are published **in English in 4 scientific areas of physics: Energy, Engineering, Materials Science, Physics and Astronomy.**

Publication Ethics and Malpractice Statement

Submission of an article to the Eurasian phys. tech. j. implies that the paper described has not been published previously, that it is not under consideration for publication elsewhere, that its publication is approved by all authors and tacitly or explicitly by the responsible authorities where the paper was carried out, and that, if accepted, it will not be published elsewhere in the same form, in English or in any other language, including electronically without the written consent of the copyright holder. In particular, translations into English of papers already published in another language are not accepted.

For information on Ethics in publishing and Ethical guidelines for journal publication see http://www.elsevier.com/publishingethics and http://www.elsevier.com/journal-authors/ethics.

The Eurasian phys.tech.j. strictly adheres the Code of Conduct of the Committee on Publication Ethics (COPE), and follows the COPE Flowcharts for Resolving Cases of Suspected Misconduct (http://publicationethics.org/files/u2/New_Code.pdf).

To verify originality, your article may be checked by the originality detection service Cross Check http://www.elsevier.com/editors/plagdetect.

Pre-publication process

Authors are responsible for the content of their publications. No other forms of scientific misconduct are allowed, such as plagiarism, falsification, fraudu-lent data, incorrect interpretation of other works, incorrect citations, etc. Authors are obliged to participate in peer review process and be ready to provide corrections, clarifications, retractions and apologies when needed. All authors of a paper should have significantly contributed to the research.

Reviewers should provide objective judgments and should point out relevant published works which are not yet cited. Reviewed articles should be treated confidentially. The reviewers will be chosen in such a way that there is no conflict of interests with respect to the research, the authors and/or the research funders.

Editors have complete responsibility and authority to reject or accept a paper, and they will only accept a paper when reasonably certain. They will preserve anonymity of reviewers and promote publication of corrections, clarifications, retractions and apologies when needed.

The acceptance of a paper automatically implies the copyright transfer to the Eurasian phys. tech. j.

All submitted papers will the sent for reviewing to leading experts in the given area.

The Editorial Board of the Eurasian phys. tech. j. will monitor and safeguard publishing ethics.

The editors reserve the right to accept or reject manuscripts.

The article and all documentation must be identified by the name of the 1st author: Akhmetov AA_et al_paper; Akhmetov AA_et al_fig.1; Akhmetov AA_et al_Cover letter; …

The article text must be formatted according to the **Template**, font - Times New Roman, size -11 pt; line spacing-single; alignment-in width, see https://phtj.buketov.edu.kz/index.php/EPTJ/about/submissions#authorGuidelines

An article should consist:

Title: includes a separate line on the left the **UDC** index, Title of the article, information about the authors-surname and initials, name of institution, city, country, e-mail of a corresponding author. The author* who submitted an article for publication will be considered as a corresponding author.

Abstract should consist of at least 5-6 sentences, not exceeding 200-250 words without formula, references, abbreviations. An abstract is a short and powerful summary that describes the focus and subject of a research paper. It could contain the information about why the research study was done, background, what the methodology was and something about the findings of the author(s).

Keywords: at least 3-10 basic terms or short phrases used in the article.

The text should be divided on structural parts: Introduction, Main part (Theoretical part, Methods and materials or Experimental technique), Results and Discussion, Conclusions.

Conclusions: formulating main results; a comparison of the results with the existing data on this topic; assessment of scientific novelty and practical value of the results.

Acknowledgments or Funding may be shown at the end of the article text, before References.

References: a bibliographic list is compiled according to the requirements:

- Books, abstracts, patents: Surname and initials of the authors (it is enough to indicate the first three or one surnames, et al), ***Title of the book*** in italics, publish house or city, year and total number of pages.
- Journals, collections of papers, conference proceedings - Surname and initials of the authors (the first three are enough), the title of the article, the ***Title of the journal*** in italics (you can use the abbreviated title), city and / or country, year, volume, issue number, pages of the "begining and end" (pp. … - … .).
- Internet links also must to indicated the authors, the title and URL

The authors should represent References according to the requirements of international journals on physics, but should to consult preliminarily for standard abbrevi¬ations of journal's names. More information on references guidelines for journal publication you can see in Harvard reference system - http://www.emeraldgrouppublishing.com /authors/guides/write/harvard.htm?part=2/

All references must be numbered in the text (for example, [1], [2-4]) and listed in numerical order.

All abbreviations and acronyms, with the exception of obviously well-known, should be deciphered at first use in the text.

Equations in your paper have to be written using the Microsoft Equation Editor or the MathType.

Tables, numbered and titled, should be inserted into the text (Times New Roman, size - 10 pt) or have been presented as an appendix at the end of the article.

Figures should be prepared in a digital form suitable for direct reproduction. Figures shall be submitted on the separate sheets or can be included into the text.

The manuscript volume, including text, formulas, figures, bibliography, should not exceed 12 pages including tables, figures (no more than 8-10) and references (no more than 30-35) of text typed on a computer using Microsoft Word editor. The review article should not exceed 20 pages with no more than 15 figures.

List of required documents

The following files must be uploaded to the journal's website:

1. Text of the article, with pictures (*.doc);
2. Figure, Picture, Photo (fig1.jpg, fig2.pcx, …);
3. Figure captions (*.doc);
4. A Cover letter - from a university, research institute or an organization licensed to conduct research activities, must be issued on an official letterhead and / or certified by the organization seal. The management officially confirms by this letter that the article (the title of the article and the names of the authors are indicated in English) doesn't contain any information constituting state or commercial secrets, and the article can be published in the Open Press. Authors must upload a copy of the signed Cover Letter in PdF format to the Journal website.

It's necessary to upload by separately 2 files in English (and in Russian for authors from Russia, and in Kazakh for authors from Kazakhstan):

5. Article's data: Surname and initials of the authors, the article title, abstract, keywords.
6. Information about each co-author: full name, academic degree, academic title, place of work or study, title of organization, city, country, SCOPUS Author ID or ORCID iD; and contact details (e-mail, phone).
7. Receipt of payment. Authors should pay for the publication only after receiving notification about a positive decision of the reviewers.